

REPORT DOCUMENTATION PAGE				Form Approved OMB NO. 0704-0188	
<p>The public reporting burden for this collection of information is estimated to average 1 hour per response, including the time for reviewing instructions, searching existing data sources, gathering and maintaining the data needed, and completing and reviewing the collection of information. Send comments regarding this burden estimate or any other aspect of this collection of information, including suggestions for reducing this burden, to Washington Headquarters Services, Directorate for Information Operations and Reports, 1215 Jefferson Davis Highway, Suite 1204, Arlington VA, 22202-4302. Respondents should be aware that notwithstanding any other provision of law, no person shall be subject to any penalty for failing to comply with a collection of information if it does not display a currently valid OMB control number.</p> <p>PLEASE DO NOT RETURN YOUR FORM TO THE ABOVE ADDRESS.</p>					
1. REPORT DATE (DD-MM-YYYY) 07-06-2013		2. REPORT TYPE Final Report		3. DATES COVERED (From - To) 14-Aug-2008 - 13-Feb-2014	
4. TITLE AND SUBTITLE Biologically Assembled Quantum Electronic Arrays				5a. CONTRACT NUMBER W911NF-08-1-0364	
				5b. GRANT NUMBER	
				5c. PROGRAM ELEMENT NUMBER 611103	
6. AUTHORS Christopher B. Murray, Todd O. Yeates, Colin Nuckolls, Nadrian C. Seeman, Yu Huang, Kang L. Wang, Allan H. MacDonald, Richard A. Kiehl, Andrew D. Kent				5d. PROJECT NUMBER	
				5e. TASK NUMBER	
				5f. WORK UNIT NUMBER	
7. PERFORMING ORGANIZATION NAMES AND ADDRESSES University of California - Davis Sponsored Programs 118 Everson Hall Davis, CA 95616 -8671				8. PERFORMING ORGANIZATION REPORT NUMBER	
9. SPONSORING/MONITORING AGENCY NAME(S) AND ADDRESS(ES) U.S. Army Research Office P.O. Box 12211 Research Triangle Park, NC 27709-2211				10. SPONSOR/MONITOR'S ACRONYM(S) ARO	
				11. SPONSOR/MONITOR'S REPORT NUMBER(S) 54505-PH-MUR.30	
12. DISTRIBUTION AVAILABILITY STATEMENT Approved for Public Release; Distribution Unlimited					
13. SUPPLEMENTARY NOTES The views, opinions and/or findings contained in this report are those of the author(s) and should not be construed as an official Department of the Army position, policy or decision, unless so designated by other documentation.					
14. ABSTRACT DNA, protein, and peptide strategies, together with chemical synthetic techniques, are exploited to create nanoparticle (NP) arrays for systematic study of quantum many-body physics in structures fabricated by biological techniques. Periodic arrays where quantum many-body physics occur within each NP and interparticle coupling of charge, electric dipole, or magnetic dipole occurs among particles are considered. The primary focus is placed on studies of magnetic interactions. Magnetic NP with organic shells suitable for functionalized attachment at specific					
15. SUBJECT TERMS biology, DNA, self-assembly, proteins, quantum mechanics, many-body effects, nanotechnology					
16. SECURITY CLASSIFICATION OF:			17. LIMITATION OF ABSTRACT UU	15. NUMBER OF PAGES	19a. NAME OF RESPONSIBLE PERSON Richard Kiehl
a. REPORT UU	b. ABSTRACT UU	c. THIS PAGE UU			19b. TELEPHONE NUMBER 530-752-0636

## Report Title

Biologically Assembled Quantum Electronic Arrays

### ABSTRACT

DNA, protein, and peptide strategies, together with chemical synthetic techniques, are exploited to create nanoparticle (NP) arrays for systematic study of quantum many-body physics in structures fabricated by biological techniques. Periodic arrays where quantum many-body physics occur within each NP and interparticle coupling of charge, electric dipole, or magnetic dipole occurs among particles are considered. The primary focus is placed on studies of magnetic interactions. Magnetic NP with organic shells suitable for functionalized attachment at specific sites on the scaffolding were assembled into arrays by DNA-directed self-assembly and drop-casting. The DNA scaffolding was suitable for controlling the coupling between the NP by DNA base sequence design and by NP shell composition and thickness, to allow future systematic studies of interactions within the arrays. The convergent goal of this interdisciplinary project was defined to be the use of DNA scaffolding for the assembly of ferromagnetic NP arrays closely coupled to an electron gas near the surface of a semiconductor for the study of many-body physics in electrically gated magnetic NP arrays. It is anticipated that this MURI will contribute to a fundamental understanding of electronic and magnetic behavior in nanoparticle arrays, which could impact computing, signal processing, and sensing.

---

**Enter List of papers submitted or published that acknowledge ARO support from the start of the project to the date of this printing. List the papers, including journal references, in the following categories:**

**(a) Papers published in peer-reviewed journals (N/A for none)**

Received

Paper

**TOTAL:**

**Number of Papers published in peer-reviewed journals:**

---

**(b) Papers published in non-peer-reviewed journals (N/A for none)**

Received

Paper

**TOTAL:**

**Number of Papers published in non peer-reviewed journals:**

---

**(c) Presentations**

P. Subedi "Hall magnetometry measurements of the susceptibility of variants on Mn12," 2011 APS March Meeting, Dallas,, Texas.

A.D. Kent "Random Field Ferromagnetism in Single Crystals on Molecular Magnets" at Quantum Coherent behavior of Spins II, UCF, Orlando, Florida, December 2012.

A.D. Kent "Random Field Dipolar Using Ferromagnetism in Single Crystals of Molecular Magnet Mn12-acetate," University of Nancy, Nancy, France.

B. Wen, P. Subedi, Y. Yeshurun, M. Sarachik, A.D. Kent, A.J. Millis, E. Pardo, S. Mukherjee and G. Christou "Demagnetizing effect in local magnetic measurements," 2012 APS March Meeting, Boston, MA.

P. Subdei, S. Velez, S. Li, M. Sarachik, J. Tejada, A.D. Kent, S. Mukherjee and G. Christou "Quantum deflagration in Mn12-acetate in the presence of a transverse field," 2012 APS March Meeting, Boston, MA.

N. Seeman, DNA-16, Hong Kong, 2010.

N. Seeman, Nanofabrication Gordon Conference, Tilton, 2010.

N. Seeman, Stereochemistry Gordon Conference, Salve Regina, 2010.

N. Seeman, James W. Canary 50th Birthday Symposium, New York, 2010.

N. Seeman, CNIC 2010, Havana, 2010.

N. Seeman, Kavli Prize Lecture, Oslo, 2010.

N. Seeman, Second Nanotechnology Symposium at NTNU, Trondheim, 2010.

N. Seeman, British Science Festival, Birmingham, 2010.

N. Seeman, 7th ERA-Chem. Flash Conf. on Bioinspired Chem., Santiago de Compostela, 2010.

N. Seeman, ElecMol'10, Grenoble, 2010.

N. Seeman, Workshop on Research Frontiers in Bioinspired Energy, Washington, DC, 2011.

N. Seeman, Kavli Futures Symposium, Plenty of Room at the Middle, Pasedena, CA, 2011.

N. Seeman, American Association for the Advancement of Science, Washington, DC, 2011.

N. Seeman, Nanoscale Biophysics Subgroup, Biophysical Society, Baltimore, 2011.

N. Seeman, ONR Workshop on 3D-Based DNA Nanofabrication, Phoenix, 2011.

N. Seeman, ISNSCE Prize Lecture, Snowbird, Utah, 2011.

N. Seeman, Synthetic Biology Workshop, Paris, 2011.

N. Seeman, Soft Matter Physics Approaches to Biology, KITP, Santa Barbara, 2011.

N. Seeman, American Crystallographic Association, Plenary Lecture, New Orleans, 2011.

N. Seeman, 94th Canadian Chemistry Conference, Montreal, 2011 [remote].

N. Seeman, Seventeenth Conversation on Biomolecular Stereodynamics, Albany, 2011.

**Peer-Reviewed Conference Proceeding publications (other than abstracts):**

Received

Paper

**TOTAL:**

**Number of Peer-Reviewed Conference Proceeding publications (other than abstracts):**

---

**(d) Manuscripts**

<u>Received</u>	<u>Paper</u>
02/01/2012	22.00 Paul M. Reichers, Richard A. Kiehl. CNN Implemented by Nonlinear Phase Dynamics in Nanoscale Processes, Proceedings of the 12th IEEE International Workshop Cellular Nanoscale Networks and Applications (02 2010)
02/02/2012	24.00 Paul Reichers, Jun Chen, Christopher Murray, Richard Kiehl. Fe <sub>3</sub> O <sub>4</sub> /GaAs Hybrid Ferromagnet/Semiconductor Nanostructures, 53rd Electronic Materials Conference, Santa Barbara, CA (06 2011)
02/02/2012	23.00 Paul M. Reichers, Richard A. Kiehl. A Scheme for Computation in Nanoscale Dynamical Systems: Gated Discrete Phase-Shift Interactions, IEEE/ACM International Symposium Nanoscale Architectures (06 2011)
02/03/2012	25.00 Hongzhou Gu, Jie Chao, Shou-Jun Xiao, Nadrian C. Seeman. Dynamic Patterning Programmed by DNA Tiles Captured on a DNA Origami substrate, Nature Nanotechnology (08 2008)
02/03/2012	28.00 Chin-Yi Chiu, Yujing Li, Yu Huang, Lingyan Ruan. Synthesis of Platinum Single-Twinned Right Bipyramid and {111}-Bipyramid through Targeted Control over Both Nucleation and Growth Using Specific Peptides, Nano Letters (06 2011)
02/03/2012	29.00 D.A. Pesin, D.A. Abanin. Ordering of Magnetic Impurities and Tunable Electronic Properties of Topological Insulators, Physical Review Letters (10 2010)
03/25/2010	1.00 K. Wong, M. Bao, J. Alzate, A. Khitun, K. Wang, A. Dong, J. Chen, C. Murray. Propagating Magnetostatic Waves Through Nanoparticle Assemblies, (03 2010)
05/15/2013	27.00 Yujing Li, Lingyan Ruan, Xingchen Ye, Christopher B. Murray, Chin-Yi Chiu, Yu Huang. Platinum nanocrystals selectively shaped using facet-specific peptide sequences, Nature Chemistry (11 2010)
12/21/2011	2.00 Dmitri V. Talapin, Elena V. Shevchenko, Maryna I. Bodnarchuk, Xingchen Ye, Jun Chen, Christopher B. Murray. Quasicrystalline order in self-assembled binary nanoparticle superlattices, Nature (10 2009)
12/22/2011	12.00 Angang Dong, Xingchen Ye, Jun Chen, Christopher B. Murray. Two-Dimensional Binary and Ternary Nanocrystal Superlattices: The Case of Monolayers and Bilayers, Nano Letters (01 2011)
12/22/2011	11.00 Angang Dong, Jun Chen, Soong Ju Oh, Weon-kyu Koh, Faxian Xiu, Xingchen Ye, Dong-Kyun Ko, Kang L. Wang, Cherie R. Kagan, Christopher B. Murray. Multiscale Periodic Assembly of Striped Nanocrystal Superlattice Films on a Liquid Surface, Nano Letters (01 2011)
12/22/2011	3.00 Christopher B. Murray, Angang Dong, Jun Chen, Patrick M. Vora, James M. Kikkawa. Binary nanocrystal superlattice membranes self-assembled at the liquid–air interface, Nature (7 2010)
12/22/2011	4.00 Angang Dong, Jing Cai, Xingchen Ye, Yijin Kang, James M. Kikkawa, Christopher B. Murray, Jun Chen. Collective Dipolar Interactions in Self-Assembled Magnetic Binary Nanocrystal Superlattice Membranes, Nano Letters (12 2010)
12/22/2011	5.00 Jun Chen, Xingchen Ye, Christopher B. Murray. Systematic Electron Crystallographic Studies of Self-Assembled Binary Nanocrystal Superlattices, ACS Nano (04 2010)

12/22/2011	6.00	D. Pesin, A. MacDonald, Shengyuan Yang, Qian Niu. Theory of I-V characteristics of magnetic Josephson junctions, Physical Review B (11 2010)
12/22/2011	7.00	Wenyan Liu, Xing Wang, Tong Wang, Ruojie Sha, Nadrian C. Seeman. PX DNA Triangle Oligomerized Using a Novel Three-Domain Motif, Nano Letters (01 2008)
12/22/2011	8.00	D. A. Pesin, A.H. MacDonald. Transport in Coherent Quantum Hall Bilayers, Physical Review B (03 2011)
12/22/2011	9.00	Xingchen Ye, Jun Chen, Yijin Kang, Thomas Gordon, James M. Kikkawa, Christopher B. Murray, Angang Dong. A Generalized Ligand-Exchange Strategy Enabling Sequential Surface Functionalization of Colloidal Nanocrystals, J. Am. Chem. Soc. (01 2011)
12/22/2011	10.00	Angang Dong, Jun Chen, Zingchen Ye, James M. Kakkawa, Christopher B. Murray. Enhanced Thermal Stability and Magnetic Properties in NaCl-Type FePt–MnO Binary Nanocrystal Superlattices, J. Am. Chem. Soc. (08 2011)
12/22/2011	13.00	Xingchen Ye, Jun Chen, Christopher B. Murray. Polymorphism in Self-Assembled AB <sub>6</sub> Binary Nanocrystal Superlattices, J. Am. Chem. Soc. (01 2011)
12/22/2011	14.00	Xingchen Ye, Joshua E. Collins, Yijin Kang, Jun Chen, Daniel T. N. Chen, Arjun G. Yodh, Christopher B. Murray. Morphologically controlled synthesis of colloidal upconversion nanophosphors and their shape-directed self-assembly, Proc. Natl. Acad. Sci. U.S.A. (12 2010)
12/22/2011	15.00	Noah L. Wieder, Kevin Bakhtmutsky, Raymond J. Gorte, Christopher B. Murray, Dianyan Wang, Yijin Kang, Vicky Doan-Nguyen, Jun Chen, Rainer Kuengas. Synthesis and Oxygen Storage Capacity of Two-Dimensional Ceria Nanocrystals, Angew Chemical International Ed (01 2011)
12/22/2011	16.00	J. Millis, A. D. Kent, M. P. Sarachik, Y. Yeshurun. Pure and Random-Field Quantum Criticality in the Dipolar Ising Model: Theory of Mn <sub>12</sub> acetates,, Physical Review B (01 2010)
12/22/2011	19.00	J. Zheng, P.S. Lukeman, W.B. Sherman, C. Micheel, A. P. Alivisatos, P.E. Constantinou, N.C. Seeman. Metallic Nanoparticles Used to Estimate the Structural Integrity of DNA Motifs, Biophysical Journal (10 2008)
12/22/2011	20.00	J. Zheng, J.J. Birktoft, Y. Chen, T. Wang, R. Sha, P.E. Constantinou, S.L. Ginell, C. Mao, N.C. Seeman. From Molecular to Macroscopic via the Rational Design of a Self-Assembled 3D DNA Crystal, Nature (09 2009)
12/22/2011	21.00	T. Wang, R. Sha, J.J. Birktoft, J. Zheng, C. Mao, N.C. Seeman. A DNA Crystal Designed to Contain Two Molecules per Asymmetric Unit, J. Am. Chem. Soc. (10 2010)
<b>TOTAL:</b>		<b>26</b>

**Number of Manuscripts:**

---

## Books

Received

Paper

**TOTAL:**

---

### **Patents Submitted**

---

### **Patents Awarded**

J.W. Canary, N.C. Seeman, L. Zhu, P.S. Lukeman Ladder Copolymers, #7,943,751, Issues, May 17, 2011.

---

### **Awards**

A.D. Kent, Invited Professor, Institut Jean Lamour, CNRS - Nancy Universite, BP 239, F-54506 Vandoeuvre, France.

---

A.D. Kent, Invited Professor, Institut d'Electronique Fondamentale (IEF), Universite Paris Sud-Bat 220, 91405 Orsay Cedex, France.

---

C. Nuckolls, 2012 Wheland Medal, University of Chicago.

C. Nuckolls, 2011-2013 "Honorable Professor" at Shanghai Normal University.

N. Seeman, 2010 Kavli Prize in Nanoscience.

N. Seeman, 2010-2011 John Simon Guggenheim Fellow.

N. Seeman, 2011, Honored by Symposium at FNANO Conference.

N. Seeman, 2011, ISNSCE Nanoscience Award, from ISNSCE.

N. Seeman, 2012, Chinese Academy of Sciences Albert Einstein Professorship Award.

---

### **Graduate Students**



<u>NAME</u>	<u>PERCENT SUPPORTED</u>	Discipline
Dagim Tilahun	0.31	
Dan Ethan McNamara	0.03	
Erik Q Fostvedt	0.22	
Garry Jason Forse	0.14	
Hayden J Peacock	0.24	
Jeffrey Meisner	0.17	
Jizhou Huang	0.28	
Kathryn Allen	1.00	
Michael Thompson	0.01	
Mohammad Sohrabi	0.48	
Mojtaba Sharifzadeh	0.35	
Paul Reichers	0.62	
Pradeep Subedi	1.00	
Rohit Hedge	0.20	
Sahar Hihath	1.00	
Tatiana S Dorofeeva	0.63	
Xinshuai Zhao	1.00	
Xubing Zhou	0.20	
<b>FTE Equivalent:</b>	<b>7.88</b>	
<b>Total Number:</b>	<b>18</b>	

#### Names of Post Doctorates

<u>NAME</u>	<u>PERCENT SUPPORTED</u>
Dima Pesin	0.80
Ruojie Sha	0.50
<b>FTE Equivalent:</b>	<b>1.30</b>
<b>Total Number:</b>	<b>2</b>

#### Names of Faculty Supported

<u>NAME</u>	<u>PERCENT SUPPORTED</u>	National Academy Member
Allan MacDonald	0.04	
Andrew Kent	0.11	
Kang L Wang	0.02	
Richard Kiehl	0.18	
Todd Yeates	0.08	
<b>FTE Equivalent:</b>	<b>0.43</b>	
<b>Total Number:</b>	<b>5</b>	

#### Names of Under Graduate students supported

<u>NAME</u>	<u>PERCENT SUPPORTED</u>	Discipline
Jianshi Tang	0.50	Electrical Engineering
Juan Alzate	0.50	Electrical Engineering
<b>FTE Equivalent:</b>	<b>1.00</b>	
<b>Total Number:</b>	<b>2</b>	

### Student Metrics

This section only applies to graduating undergraduates supported by this agreement in this reporting period

The number of undergraduates funded by this agreement who graduated during this period: .....

The number of undergraduates funded by this agreement who graduated during this period with a degree in science, mathematics, engineering, or technology fields:.....

The number of undergraduates funded by your agreement who graduated during this period and will continue to pursue a graduate or Ph.D. degree in science, mathematics, engineering, or technology fields:.....

Number of graduating undergraduates who achieved a 3.5 GPA to 4.0 (4.0 max scale): .....

Number of graduating undergraduates funded by a DoD funded Center of Excellence grant for Education, Research and Engineering: .....

The number of undergraduates funded by your agreement who graduated during this period and intend to work for the Department of Defense .....

The number of undergraduates funded by your agreement who graduated during this period and will receive scholarships or fellowships for further studies in science, mathematics, engineering or technology fields: .....

### Names of Personnel receiving masters degrees

NAME

**Total Number:**

### Names of personnel receiving PHDs

NAME

Anuttara Udomprasert  
Chunhua Liu  
Dadong Li  
Dagim Tilahun  
Hari Krishnaswamy Subramanian  
Tanashya Ciengshin  
Wenyan Liu  
Xubing Zhou  
Yoel Ohayon

**Total Number:** 9

### Names of other research staff

NAME

PERCENT SUPPORTED

Fang Sheng	0.25
Inna Pashkov	0.21
Kin Wong	1.00
Natalie Wagner	0.01
Rita Jo Dos Santos Macedo	1.00

**FTE Equivalent:** 2.47

**Total Number:** 5

### Sub Contractors (DD882)

## **Inventions (DD882)**

### **Scientific Progress**

See Attachment

### **Technology Transfer**

# **Biologically Assembled Quantum Electronic Arrays**

**W911NF-08-1-0364**

## **Final Report**

### **Principal Investigator**

Professor Richard A. Kiehl  
Department of Electrical & Computer Engineering  
University of California, Davis, California

### **Co-Principal Investigators**

Professor Yu Huang  
Department of Materials Science and Engineering  
University of California, Los Angeles, California

Professor Andrew D. Kent  
Department of Physics  
New York University, New York, New York

Professor Allan H. MacDonald  
Department of Physics  
University of Texas, Austin, Texas

Professor Christopher B. Murray  
Departments of Chemistry and Materials Science and Engineering  
University of Pennsylvania, Philadelphia, Pennsylvania

Professor Colin Nuckolls  
Department of Chemistry  
Columbia University, New York, New York

Professor Nadrian C. Seeman  
Department of Chemistry  
New York University, New York, New York

Professor Kang L. Wang  
Department of Electrical Engineering  
University of California, Los Angeles, California

Professor Todd O. Yeates  
Department of Chemistry and Biochemistry  
University of California, Los Angeles, California

## TABLE OF CONTENTS

**Statement of problem studied. ... p. 3**

**Summary of the most important results ... p. 4**

**Theory of quantum many-body effects in NP arrays (TS1). Allan H. MacDonald ... p. 6**

**NP-array nanostructures and electronic transport studies (ES-1). Richard A. Kiehl ... p. 12**

**Spectroscopic studies of magnetic/coulombic NP arrays (ES-2). Andrew D. Kent ... p. 23**

**Dynamic studies of spin transport in magnetic NP arrays (ES-2). Kang L. Wang ... p. 28**

**Core/shell NP synthesis (NP-1). Christopher B. Murray ... p. 33**

**Functionalization and attachment of NP (NP-2). Colin Nuckolls ... p. 41**

**DNA scaffolding of NP arrays (DP-1). Nadrian C. Seeman ... p. 52**

**Protein-organized dimer and trimer NP subcomponents (DP-2). Todd O. Yeates ... p. 60**

**Specific peptide affinities to core/shell NP (DP-3). Yu Huang ... p. 64**

## STATEMENT OF THE PROBLEM STUDIED

This MURI has exploited DNA, protein, and peptide strategies, together with chemical synthetic techniques, to create nanoparticle (NP) arrays for systematic study of quantum many-body physics in normal metal and magnetic NP systems. This study has provided a foundation for the development of a reliable biological route to precision assembly of quantum electronic systems that can operate at room temperature.

The scope of this study includes the many-body physics of electronic, magnetic and photonic systems. Each type of system offers its own possibilities for exploring new physics. We focused on periodic arrays where quantum many-body physics occur within each NP and interparticle coupling of charge, electric dipole, or magnetic dipole plays a central role. Our primary focus evolved toward magnetic dipole and exchange interactions.

The quantum systems were constructed by biological assembly of NP primarily in 2D geometries. The NP were composed of monodisperse normal metal and magnetic NP with organic shells that could be functionalized for attachment at specific sites on the scaffolding. Drop-casting of NP with organic shells was used to provide simple preliminary test structures for studies in the limit of close-packed arrays. The DNA scaffolding studied during the project was suitable for controlling the coupling between NP by DNA base sequence design and by NP shell composition and thickness, to allow systematic studies of interactions within the arrays.

The initial convergent goal for the various tasks of this project was defined as the assembly of protein-organized metallic NP dimers or trimers into arrays on DNA scaffolding. The ability to control size, spacing, composition, and coupling in such a structure would represent a *tour de force* in biological assembly. As the project evolved, the goal was redefined to be the use of DNA scaffolding for assembly of ferromagnetic NP arrays in closely coupled to an electron gas near the surface of a semiconductor substrate for study of electrically gated magnetic coupling in nanoparticle arrays.

It is anticipated that this MURI will contribute to a fundamental understanding of electronic and magnetic behavior due to many-body physics in nanoparticle arrays, which could impact future DoD capabilities for computing, signal processing, and sensing. In addition, the results of this project will improve our understanding of critical issues for exploiting biological approaches for assembling quantum systems based on organic-inorganic structures.

## SUMMARY OF THE MOST IMPORTANT RESULTS

### NP Synthesis and Test Structure Fabrication

- **Synthesis of uniform single-particle and binary superlattice (BNSL) ferromagnetic NP arrays by drop casting.** Drop-casting of inorganic NP with organic shells provided a simple means for preliminary studies of arrays in the close-packed limit to complement studies tailorable, DNA-assembled arrays.
- **Development of process for bonding  $\text{Fe}_3\text{O}_4$  -NP to GaAs and InAs substrates.** Demonstrated the critical organic removal and physical bonding steps needed for electronic coupling NP arrays to the substrates.
- **Demonstration of e-beam patterning of mesoporous silica at sub-100 nm dimensions.** Patterning of mesoporous silica potentially provides means for passivating and contacting hybrid organic/inorganic DNA-assembled NP arrays.
- **Mask set design and fabrication of FET, Hall and test devices for studies of gated exchange interactions.** Used to fabricate and characterize graphene field-effect transistors.

### Biological Self-assembly

- **Self-assembly of  $\text{Fe}_3\text{O}_4$  -NP to DNA scaffolding.** Established protocol for  $\text{Fe}_3\text{O}_4$  -NP assembly to 2D DNA scaffolding.
- **Self-assembly of molecular bridges between NP and GaAs substrate.** NP were self-assembled into 2D arrays with molecular bridges to a GaAs substrate, as a step toward exchange through a substrate.
- **Synthesis of molecular bridges with tunable solubility and conductivity.** Designs for high conductivity were explored and demonstrated.
- **Identification of peptide sequences with specific binding to  $\text{Fe}_3\text{O}_4$  and FePt.** Such specific binding is desired for the synthesis of NP trimer modules for this study.
- **Demonstration of protein trimers with non-specific (cysteine) and specific (peptide) binding tails for NP attachment.** Pt NP trimers observed by electron microscopy but low yield suggests peptide affinity may not be sufficiently robust.
- **Self-assembly of protein trimers on DNA scaffolding.** Protein trimers assembly to DNA origami scaffolding confirmed by AFM imaging.
- **Demonstration of peptide shaping of FePt NP.** Biological control of shape anisotropy demonstrated, as desired for certain NP array studies.

### Characterization

- **FMR characterization of ferromagnetic NP arrays.** Resolved characteristics down to single monolayer  $\text{Fe}_3\text{O}_4$  arrays for studies of interparticle dipole interactions.
- **TEM characterization of  $\text{Fe}_3\text{O}_4$  -NP / GaAs interface in bonded arrays.** Confirmed crystallinity of  $\text{Fe}_3\text{O}_4$ -NP post processing; identified need for control of amorphous interlayer for achieving strong coupling.



- **Conductance-AFM evidence for  $\text{Fe}_3\text{O}_4$  -NP to n-InAs coupling.** C-AFM images indicate that electronic coupling was achieved by optimized processing, as needed for substrate-mediated exchange interactions.
- **Capacitance-voltage characterization of back-gated 2DEG in GaAs heterostructure.** Demonstrated suitability of CV technique for determining optimal heterostructure design for NP coupling through substrate.
- **Magnetic characterization of nanoparticle arrays.** Field- and temperature dependent magnetometry revealed affect of annealing cycle on moment and blocking temperature in  $\text{Fe}_3\text{O}_4$  arrays, as needed for design of optimized structures.
- **Magneto-optical Kerr effect (MOKE) characterization of multiferroic composite laminate of Ni on top of piezoelectric substrate.** Results reveal a change in the magnetic hysteresis as a function of electric field but exchange interaction requires closer packing.

### Physics

- **FMR characterization of dipole interactions in ferromagnetic NP monolayers.** Results show anisotropy for  $\text{Fe}_3\text{O}_4$  NP arrays as thin as one monolayer and lower magnetization than for “effective medium” model, consistent with MacDonalds model.
- **Theory of ferromagnetic resonance (FMR) in regular, dense nanoparticle arrays.** The model includes finite NP size and magnetic dipolar interactions and shows that the interparticle dipolar interaction leads to an easy-plane anisotropy in magnetic energy that explains our experimental results.
- **Theory of current-induced magnetization reversal in a nanomagnet with structural inversion asymmetry.** Derived an expression for the effective switching magnetic field, which is in good agreement with literature experiments.
- **Observation of collective blocking temperature in binary nanocrystal superlattice (BNSL).** Observe a single blocking temperature due to collective behavior rather than separate blocking temperatures of the constituents.
- **Concept and structures for electrical control of exchange interactions in arrays of ferromagnetic nanoparticles.** This topic was identified at the 2<sup>nd</sup> annual project review as the primary focus of the project.
- **$\Delta$ -M magnetometry of interactions in  $\text{Fe}_3\text{O}_4$  - NP on GaAs.** Demonstrated usefulness of first order reversal curves for characterizing the NP arrays.
- **Theory of gate-tunable exchange coupling in the case of cobalt NP on graphene.** Used Spin-density-functional theory and simple model for shifts in majority and minority energies. The results confirm that both the sign and magnitude of the magnetic coupling can be tuned by electric fields due to changes in the graphene carrier density.



# **Theory of quantum many-body effects in NP arrays (TS-1). Allan H. MacDonald**

## **Theory of nanoparticle array characterization using ferromagnetic resonance**

We have developed a theory of ferromagnetic resonance (FMR) in regular dense nanoparticle arrays. The theory quantitatively describes the experiments performed in Andrew Kent's group. Our findings are summarized in Fig. 1. The corresponding manuscript is being prepared for publication.

In general, ferromagnetic resonance has proven to be a valuable tool in studying magnetic properties (e.g. the type of magnetic anisotropy) of magnetic materials [1]. It is natural to apply this technique to nanoparticle arrays, as has been done in the group of Andrew Kent as part of this MURI effort.

Magnetic nanoparticles normally form poorly characterized random anisotropy axis arrays. Due to the recent progress in fabrication, it has been possible to create well-formed hexagonal nanoparticle arrays of magnetically soft  $\text{Fe}_3\text{O}_4$  nanoparticles. The experiments of Kent's group were performed on this type of array. It was observed that the properties of dense arrays were different from what could have been expected for thin film ferromagnets.

From the theory side, FMR of disordered arrays of nanoparticles was considered in Ref. [2]. Importantly, the magnetic dipole-dipole interaction was neglected in that study. In dense arrays, however, the dipolar interaction between nanoparticles is important due to considerable size of the nanomagnets, and their superparamagnetic behavior. In the present work our task was to build a theory of FMR in nanoparticle arrays, which

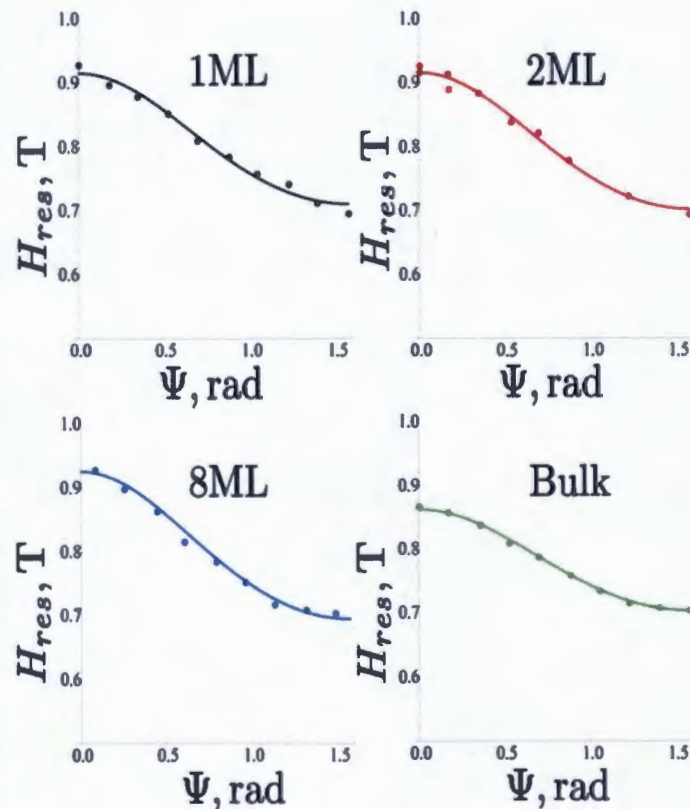


Fig. 1: Theoretical dependences of the resonant magnetic field,  $H_{res}$ , on its orientation (angle  $\Psi$ ) with respect to the sample plain (solid lines), and experimental data (dots) for various numbers of magnetic layers of nanoparticles (ML), and a bulk (drop casted) film.

takes into account finite size of the nanoparticles (i.e. goes beyond the point-dipole approximation), and their magnetic dipolar interaction.

The results of our theoretical fit to the experimental data are shown in Fig. 1. The essentially parameter-free fit is quite good. In what follows we briefly outline the theory that we developed for ferromagnetic resonance in nanoparticle arrays.

To describe the dynamics of the uniform mode of the array magnetization, we use the standard approach based on the Landau-Lifshitz equation:

$$\frac{\partial \mathbf{m}}{\partial t} = -\gamma \mathbf{m} \times \mathbf{H}_{\text{eff}} + \alpha \mathbf{m} \times \frac{\partial \mathbf{m}}{\partial t}. \quad (1)$$

In the above equation  $\mathbf{m}$  represents the direction of each nanoparticle magnetization (assumed the same for all nanoparticles in the array),  $\mathbf{H}_{\text{eff}}$  is the effective magnetic field felt by a nanoparticle,  $\alpha$  is the Gilbert damping constant, and  $\gamma$  is the gyromagnetic ratio. Here and in what follows we consider the dynamics of the uniform mode of the magnetization. Thus we assume that magnetic moment of each nanoparticle points in the same direction. This, in turn, means that we can consider FMR for a single nanoparticle, whose energy density is modified by dipolar interaction with the rest of the nanoparticles.

Magnetic field  $\mathbf{H}_{\text{eff}}$  includes an external magnetic field, and the field resulting from dipolar interaction between nanoparticles. It is defined as  $\mathbf{H}_{\text{eff}} = -\delta E / \delta (M_S \mathbf{m})$ , where  $E$  is the the aforementioned effective energy density per nanoparticle, and  $M_S$  is the saturation magnetization. We have shown that in all cases studied the dipolar interaction between nanoparticles leads to an easy-plane anisotropy in magnetic energy of a nanoparticle:

$$E = -M_S \mathbf{m} \mathbf{H} + 2\pi K M_S^2 m_{\perp}^2 \quad (2)$$

Here  $\mathbf{H}$  is the static external magnetic field, and  $m_{\perp}$  is the component of the magnetization direction perpendicular to the array plane. The dimensionless constant  $K$  depends on the geometry of an array, and was calculated for each type of array.

Once the energy density per particle is calculated, one can find the frequency at which the resonant absorption of microwave radiation occurs by solving Eq. (1), to arrive at the standard expression:

$$\frac{\omega^2}{\gamma^2} = \frac{1}{M_S^2 \sin^2 \theta} \left[ \frac{\partial^2 E}{\partial \theta^2} \frac{\partial^2 E}{\partial \phi^2} - \left( \frac{\partial^2 E}{\partial \phi \partial \theta} \right)^2 \right] \bigg|_{\theta=\theta_0, \phi=\phi_0}. \quad (3)$$

The angles  $\theta$ ,  $\phi$  and  $\theta_0$ ,  $\phi_0$  describe the orientation and the equilibrium orientation of the magnetization in the external field  $\mathbf{H}$ , respectively. The solution of Eq. (3) provides

an implicit dependence  $H_{res}(\varphi)$  at given frequency  $\omega$ . These dependences are the main result of this work, and are summarized in Fig. 1.

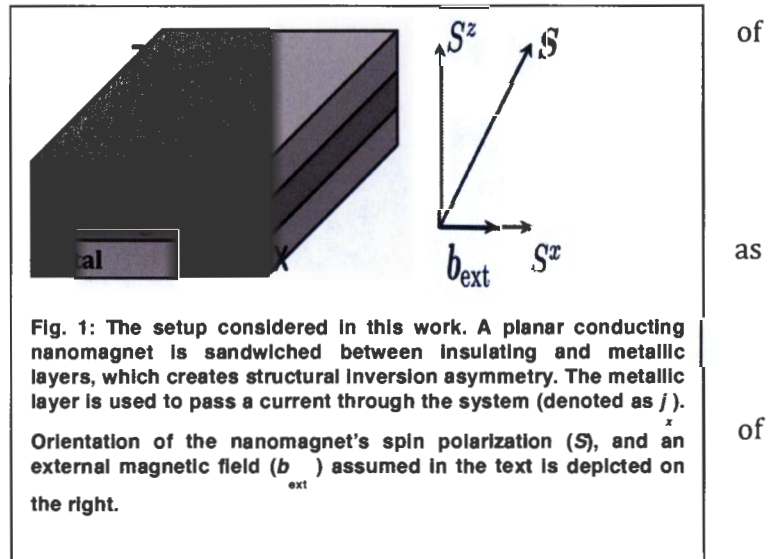
The work described above is being prepared for publication.

#### Bibliography:

- [1] Ch. Kittel, "Introduction to Solid State Physics: 8<sup>th</sup> edition", (Johh Wiley & Sons, Inc, 2005)
- [2] A. Sukhov, K.D. Usadel, U. Nowak, "Ferromagnetic resonance in an ensemble of nanoparticles with randomly distributed anisotropy axes", J. Magn. Magn. Mater., Vol. 320, pp. 31-35, Jan 2008

### Current-induced magnetization switching in nanomagnets with structural inversion asymmetry

Over the past several months we have developed a theory current-induced magnetization reversal in a nanomagnet with structural inversion asymmetry. This is potentially relevant for the magnetic recording industry, has been demonstrated in a recent experimental work [1]. We would like to further explore the possibility to electrically control *ensembles* nanomagnets, deposited on a conducting substrate, in close collaboration with experimental groups.



It is well known that structural inversion asymmetry leads to a particular kind of spin-orbit interaction in 2D electron systems, known as the Rashba spin-orbit interaction. There is a large body of work on spin-orbit-interaction-driven phenomena in semiconductors. In particular, a great deal of attention has been paid to the field of spintronics: the electrical control of the electronic spin. Recently, a successful attempt to electrically control magnetization direction of a nanomagnet has been reported [1]. In Ref. [1], reliable switching of magnetization direction of a two-dimensional ferromagnetic island with perpendicular magnetic anisotropy was shown, and further used to build a magnetic switch device. This remarkable achievement has obvious *practical* implications for the magnetic storage industry. We expect the experimental groups participating in this grant to be able to build nanoparticle arrays on conducting



substrates to explore the possibilities to control the collective behavior of an array with electric currents.

The geometry we have considered, and which was used in Ref. [1], is depicted in Fig. 1. The nanomagnet is assumed to have a strong easy-axis anisotropy perpendicular to its plane, which is necessary for thermal stability and scalability of the device. In this geometry, a strong enough current pulse flowing through the setup in the direction of the applied external magnetic field is able to deterministically switch the direction of the ferromagnetic layer's magnetization (between two perpendicular to the layer plane directions). For each magnetization direction and fixed direction of the external magnetic field, only one of the two possible current flow directions leads to switching. Further, the switching is absent for current flowing in the direction perpendicular to the one of the external magnetic field, and the critical value of the current necessary for switching decreases with increasing external magnetic field. Our final result is an expression for an effective switching magnetic field, which points almost perpendicular to the nanomagnet's plane:

$$B_d^{\text{eff}} = -eE\alpha N_0\gamma_0 \int dr \frac{S_x S_z}{S_x^2 + 2S_z^2}, \quad \gamma_0 = \frac{p_F}{v_F} \frac{\partial v_F}{\partial p_F} - 1$$

In this expression  $E$  is the electric field,  $\alpha$  characterizes the strength of the spin-orbit interaction,  $N_0$  and  $\gamma_0$  are the density of states and band non-parabolicity of the ferromagnet, and  $S_i$  denote the Cartesian components of the ferromagnet's spin polarization. We can estimate this field using the material parameters for Cobalt, which gives

$$B_z \sim \frac{\hbar e E \alpha N_{\downarrow}}{M_S} \frac{M_x}{M_S} \approx 50 \text{ mT}$$

Here  $N_{\downarrow}$  is the minority spin density of states at the Fermi surface for Cobalt,  $M_S$  is its saturation magnetization, while  $M_x$  is the x-component of the magnetization, determined by the competition between the external magnetic field and easy-axis anisotropy. The electric field value is chosen such that it corresponds to the experimental current of  $10^{12} \text{ A/m}^2$ . We note that the number obtained here is very close to the experimentally reported 70-90 mT.

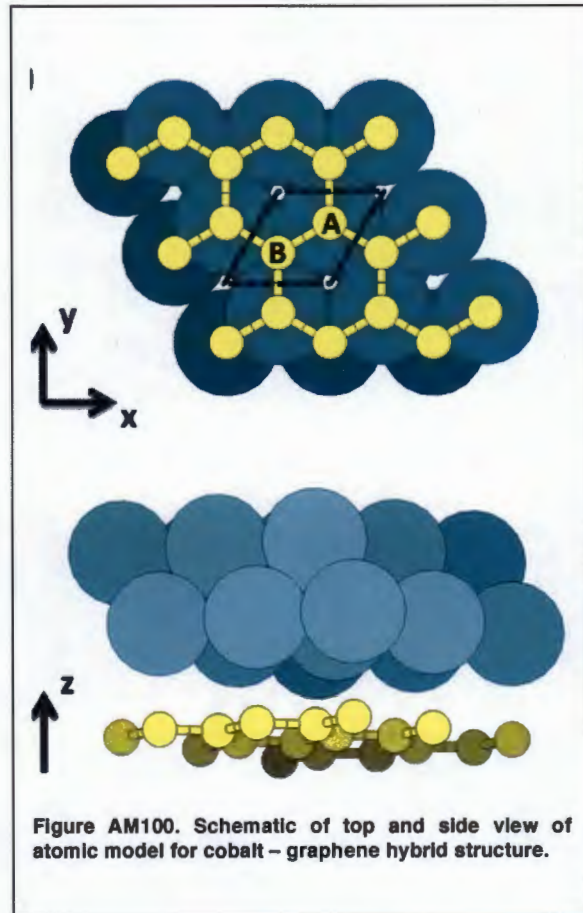
In order to obtain the above result, we derived and solved the kinetic equation for a conducting ferromagnet with structural inversion asymmetry. In 3d transition metals, of which Cobalt is an example, building a kinetic scheme is complicated by a large number of electronic bands at the Fermi surface. Both 3d- and 4s-derived electronic bands are responsible for ferromagnetism and transport. Ferromagnetic properties are mostly due to the d-bands, but there are usually states of both types at the Fermi level. Since both types of the electronic bands participate in transport, and both types of bands are spin-orbit coupled, it is impossible to decide *a priori* which ones are more important for the magnetization switching discussed above. The d-bands are favored by a large density of states at the Fermi surface, as is typical for ferromagnetism, and strong atomic spin-orbit interaction, yet the s-bands should have a larger value of a spin-orbit interaction coming from the structural inversion asymmetry due to larger wave function overlaps. To chose

a specific model, admittedly simplified, but allowing to build a quantitative theory of the above phenomena, we viewed a ferromagnetic transition metal as consisting of two abstract subsystems of localized ('d') and mobile ('s') electrons. The former are considered responsible for the ferromagnetism, and the latter are itinerant electrons participating in transport. The s-electrons were further assumed to occupy a single Kramers-degenerate band. The coupling between the two types of bands was introduced via a simple local exchange Hamiltonian. We note that this division into d- and s-electrons does not literally correspond to the original 3d and 4s bands of the realistic substance: In principle, we could think of the 3d-electrons alone in this kind of way, self-consistently demanding that the average magnetization of the "localized" electrons coincides with that of the itinerant ones (which is the essence of the Stoner model of ferromagnetism). As we saw above, such a simplified treatment led to a good quantitative agreement with experiment.

Currently, we are working on extending this treatment to a more realistic model of a ferromagnet, as well as generalizing the results to assemblies of nanomagnets on a conducting substrate.

#### Bibliography:

[1] I. M. Miron, K. Garello, G. Gaudin, P. Zermatten, M. V. Costache, S. Auffret, S. Bandiera, B. Rodmacq, A. Schuhl, and P. Gambardella, *Nature* Vol. **476**, pp. 189-193, Jul 2011.



#### Gate-Tunable Exchange Coupling Between Cobalt Clusters on Graphene

During the last period of the project we theoretically investigated the possibility for electrical gate control of exchange interactions between ferromagnetic NP coupled through a two-dimensional electron gas, in concert with the various experimental studies by the Kiehl group. We examined the particular case of gate control of the magnetic coupling between infinite Co electrodes on top of graphene.

Spin-density-functional theory ab initio calculations were used to theoretically explore the possibility of achieving useful gate control over exchange coupling between cobalt clusters placed on a graphene sheet. An illustration of the model is given in Fig. AM100. In the calculations we used a 20x1 supercell with 18 atoms in each supercell and 3 layers of



Co. Graphene was taken to be continuous in the x-y plane and the electric field was taken to be applied in the z direction normal to the plane.

The two-dimensional band structure of the Co-graphene hybrid system is shown on the left in Fig. AM110. The blue lines illustrate the majority spin bands and the red lines the minority spin bands. The blue and red dots indicate the strength of carbon  $p_z$  orbital character in the majority and minority spin states. Our electronic structure calculations could be qualitatively described using a simple model for graphene coupled to a cobalt overlayer in which hybridization and charge transfer effects shift the energies of both majority and minority spins on both graphene sublattices. The model includes the usual Dirac Hamiltonian for hopping

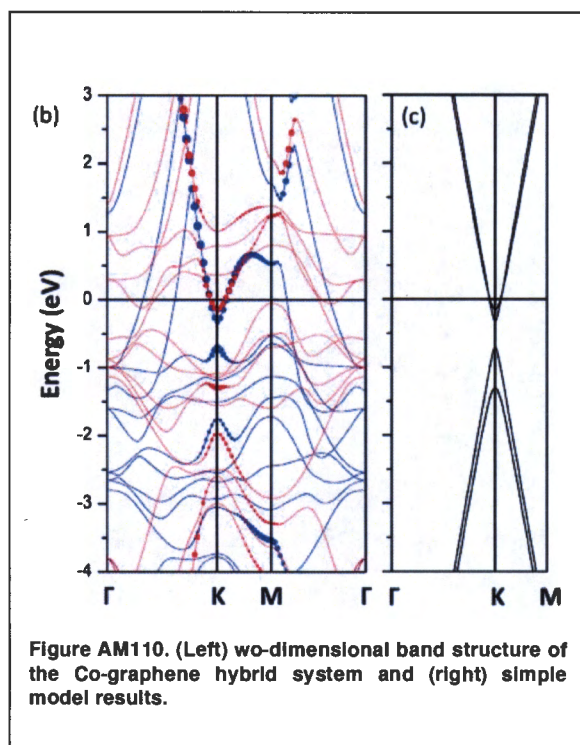


Figure AM110. (Left) two-dimensional band structure of the Co-graphene hybrid system and (right) simple model results.

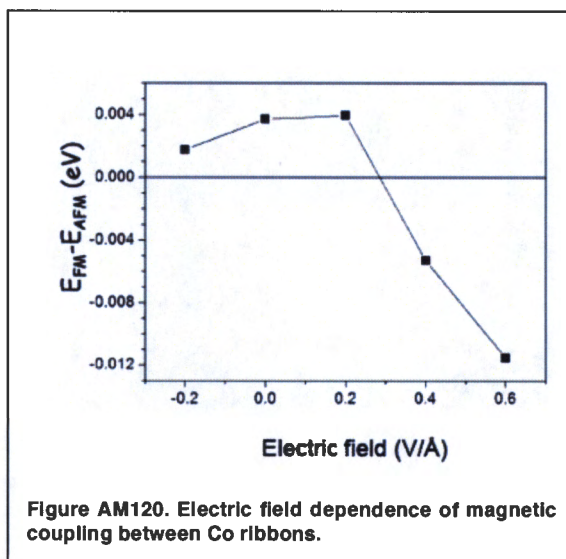


Figure AM120. Electric field dependence of magnetic coupling between Co ribbons.

on a honeycomb lattice. The parameters of this model were identified by fitting to the energies of the bands that have the largest band character at the Brillouin-zone corner points.

The calculated electric-field dependence of the magnetic coupling between two different cobalt ribbons is shown in Fig. AM120. The results confirm that both the sign and magnitude of the magnetic coupling can be tuned by electric fields due to changes in the graphene carrier density. Further study is underway to more quantitatively examine this control mechanism. In particular, we will study sensitive to the relative sublattice registration, as well as to the size and spacing of the cobalt clusters, to provide guidance to the experimental investigations.

## NP-array nanostructures and electronic transport studies

### (ES-1). Richard A. Kiehl

The initial scope of this program included a wide range of topics in many-body physics in nanoparticle arrays. Earlier work by Kiehl et al in DNA assembled NP arrays showed quantum behavior in the form of pronounced single-electron tunneling steps in the current-voltage characteristics of linear arrays of gold nanoparticles assembled by 2D DNA scaffolding. In the early period of this program the Kiehl group focused essential fabrication issues for such arrays.

DNA offers the ultimate in precision programmability for self-assembly the nanoscale. The programmable of DNA structures, the nucleotide, is only 0.34 nm. However, DNA is fragile, it does not offer a robust framework compared with conventional semiconductor fabrication technologies. Even as a scheme for organizing inorganic NP study of fundamental physics, one needs a way to exploit precision while adding robustness. Thus our earliest studies in the MURI were focused on a scheme for passivating DNA and organic structures while making electrical contact for single electron tunneling and similar studies.

We investigated a strategy suggested by Atul Parikh (UC Davis) based on mesoporous silica. The basic idea is to use DNA scaffolding organization of NP and then to passivate the NP in an intimate silica matrix. This can be thought of as an embalming process for the materials where the structure is not only maintained but made robust. An additional and essential feature, is to a high resolution patterning technique to define porous regions the silica structure that allow electrical contact to be made.

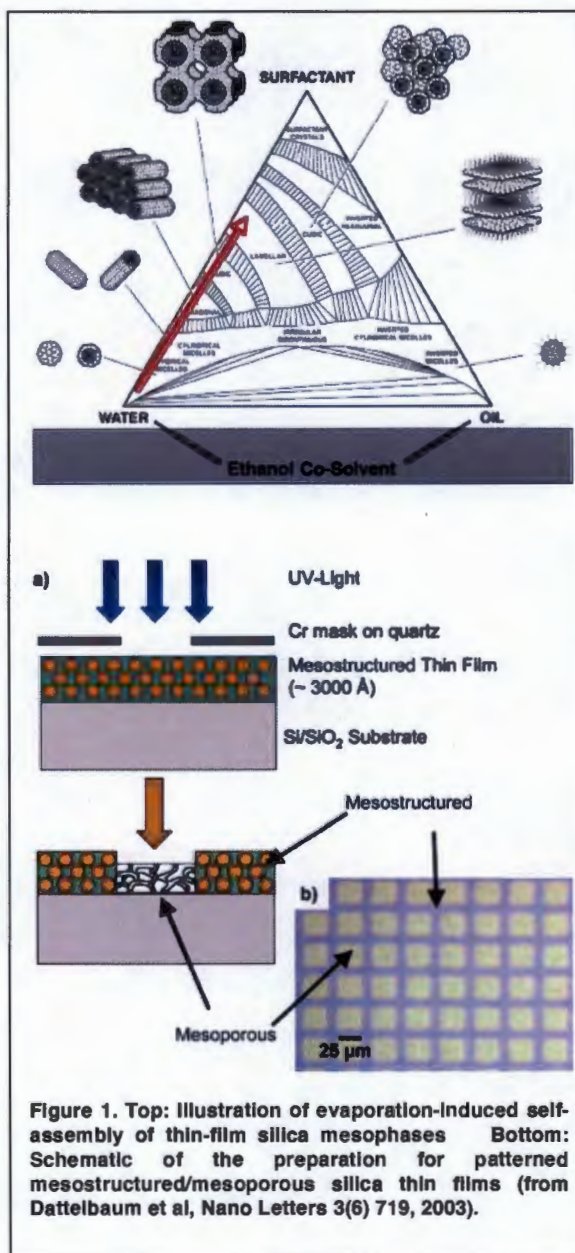


Figure 1. Top: Illustration of evaporation-induced self-assembly of thin-film silica mesophases. Bottom: Schematic of the preparation for patterned mesostructured/mesoporous silica thin films (from Dattelbaum et al, Nano Letters 3(6) 719, 2003).



The top of Fig. 1 illustrates the concept of evaporation-induced self-assembly of thin-film silica mesophases, which was discussed by Brinker et al (Nature 1992). The hexagonal phase of surfactant templated silica contains horizontal but not vertical channels. Vertical channels exist, however, in cubic phase silica, which opens the possibility for making contact to underlying structures. The bottom of Fig. 1 shows a schematic for the preparation of mesostructured/mesoporous silica thin films patterned by UV irradiation. (Dattelbaum et al, Nano Letters 3(6) 719, 2003)

For the purposes of this MURI, we need nanoscale patterning of contact regions. We have therefore investigated the use of electron beam lithography for patterning meso-porous silica into nanoscale porous and non-porous regions.

Figure 2 shows a process for making electrical contacts to a DNA-assembled nanoparticle array via e-beam patterning of meso-porous silica. As is illustrated, an e-beam exposes photoresist to allow its removal and transforms silica from non-porous hexagonal phase to porous cubic phase. Electroless deposition is then used for precipitation of silver in pores to form conductive channels to buried nanoparticles. Then, evaporated metal is used to make contact to channels. In the final step (not shown in the figure) the non-contacting metal regions are removed by a conventional liftoff process.

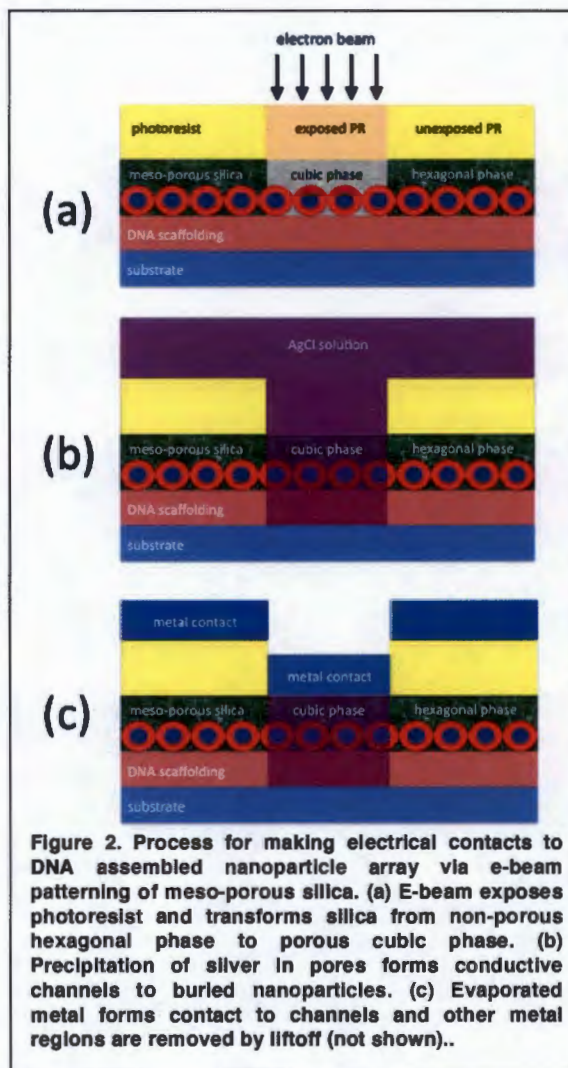


Figure 2. Process for making electrical contacts to DNA assembled nanoparticle array via e-beam patterning of meso-porous silica. (a) E-beam exposes photoresist and transforms silica from non-porous hexagonal phase to porous cubic phase. (b) Precipitation of silver in pores forms conductive channels to buried nanoparticles. (c) Evaporated metal forms contact to channels and other metal regions are removed by liftoff (not shown)..



Figure 3 shows results from our initial studies this approach. The figure shows a scanning electron micrograph of a nanoscale pinwheel directly written into the mesoporous silica with a focused electron beam. The thickness of the silica layer is reduced by exposure, as was the case for UV patterned layers. The fine details of the patterns suggest that material changes can be directly written into mesoporous silica thin films with nanoscale precision. In particular, the width of the lines the image is approximately 100 nm. Moreover, the individual pixels of the electron beam writing process are visible in the Fig. 3 image, illustrating the potential for nanoscale patterning. Further studies are underway to determine the material properties in the patterned and unpatterned regions and to confirm that the desired change in porosity has been obtained. If successful, this technique would provide an enabling technology to a wide range of bio-medical applications beyond this MURI.

Our evaluation of the most interesting physics

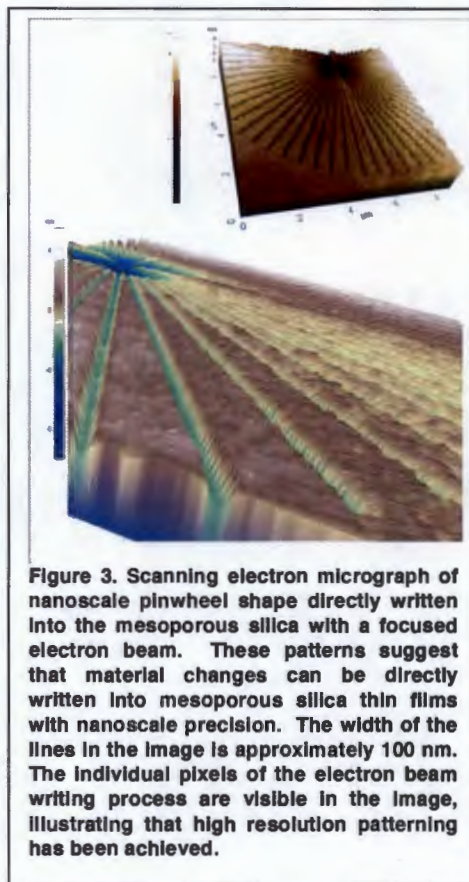
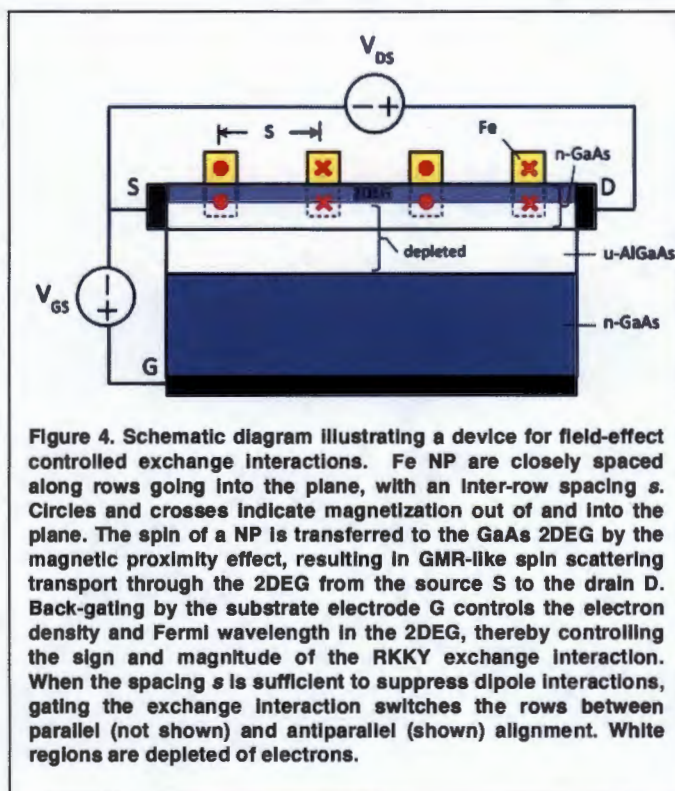


Figure 3. Scanning electron micrograph of nanoscale pinwheel shape directly written into the mesoporous silica with a focused electron beam. These patterns suggest that material changes can be directly written into mesoporous silica thin films with nanoscale precision. The width of the lines in the image is approximately 100 nm. The individual pixels of the electron beam writing process are visible in the image, illustrating that high resolution patterning has been achieved.



evolved in the first years. The many-body physics of arrays of ferromagnetic nanoparticles has taken priority, and the Kiehl Group work has shifted from making electrical contact to normal metal NP to making contact between ferromagnetic NP and a thin normal metal, the 2DEG at the surface of a semiconductor. The shift was stimulated by the expected richness of exchange interactions in FM NP arrays, as well as the difficulty in obtaining sufficient coupling for exchange interactions between even closely packed nanoparticles, as found by the U. Penn group. In trying to come up with an approach for increased exchange interaction, Kiehl and MacDonald considered coupling through a substrate and suggested a



GaAs-based structure, which offered not only coupling but gating.

Figure 4 is schematic diagram illustrating a GaAs-based test structure for studying gated exchange interactions, and other many body physics, in arrays of biologically assembled ferromagnetic (FM) nanoparticles (NPs). Electronic current flows through a surface two-dimensional electron gas (2DEG), which is coupled to the NP. The spin in the 2DEG is controlled by the magnetization of the nearby NP, as indicated. The density of the 2DEG is electrically controlled by the bias of n -GaAs back-gate electrode. InGaAs is key as the surface layer because the Fermi level in compounds near pure InAs is near or in the conduction band, thereby promoting coupling.

Details of the exchange gating concept are illustrated in Fig. 5. As shown, as the gate voltage is increased i)  $n$  the 2DEG electron density increases, ii) the Fermi wavelength decreases, iii)  $J$  the exchange coupling oscillates and iv)  $G$  the conductance oscillates. Applying a magnetic field  $H_s$  sufficient to force parallel alignment of the ferromagnetic nanoparticles will suppresses the  $G$  oscillation.



Figure 6. Close-packed arrays of  $\text{Fe}_3\text{O}_4$  nanoparticles on GaAs. A novel adsorption technique was developed at UC Davis for GaAs substrates, for which other techniques were much less effective. Top: 200 nm scale bar (see lower right). Bottom: 2 micron scale bar. The innermost (green) square defines the region in the magnified image.

Thus we shifted our focus to test vehicles for bio-assembly of FM NP on InAs epitaxial layer on GaAs. As a

preliminary step looked at close-packed arrays of  $\text{Fe}_3\text{O}_4$  nanoparticles on GaAs. The protocols for assembling arrays on  $\text{SiO}_2/\text{Si}$ , as used in most studies are not effective for GaAs. An important accomplishment in the UC Davis work was the development of an adsorption technique for

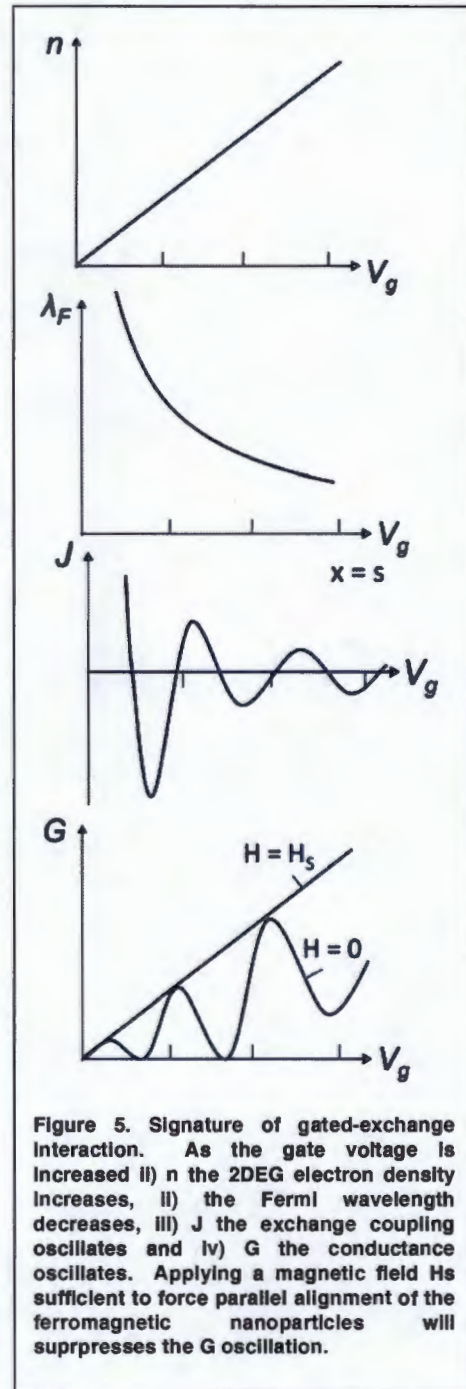
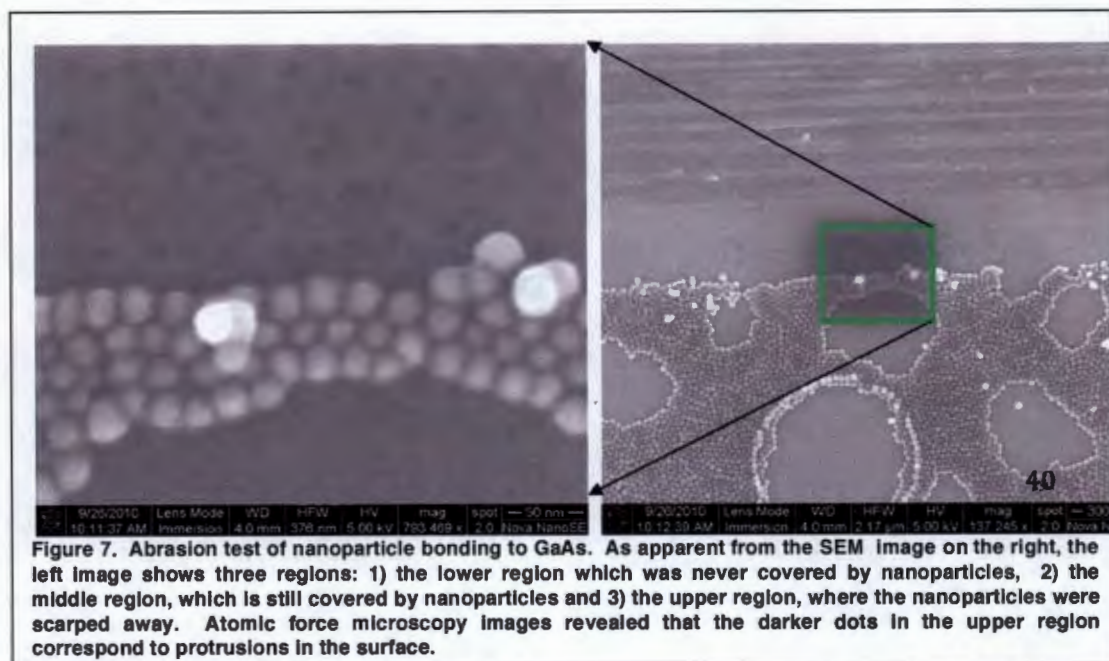


Figure 5. Signature of gated-exchange interaction. As the gate voltage is increased i)  $n$  the 2DEG electron density increases, ii) the Fermi wavelength decreases, iii)  $J$  the exchange coupling oscillates and iv)  $G$  the conductance oscillates. Applying a magnetic field  $H_s$  sufficient to force parallel alignment of the ferromagnetic nanoparticles will suppresses the  $G$  oscillation.

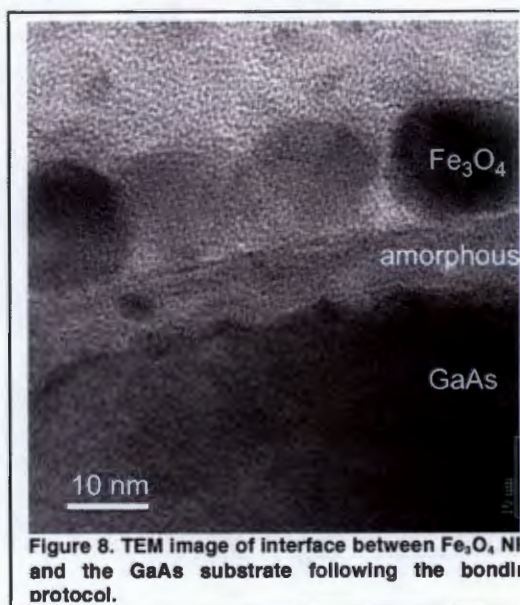


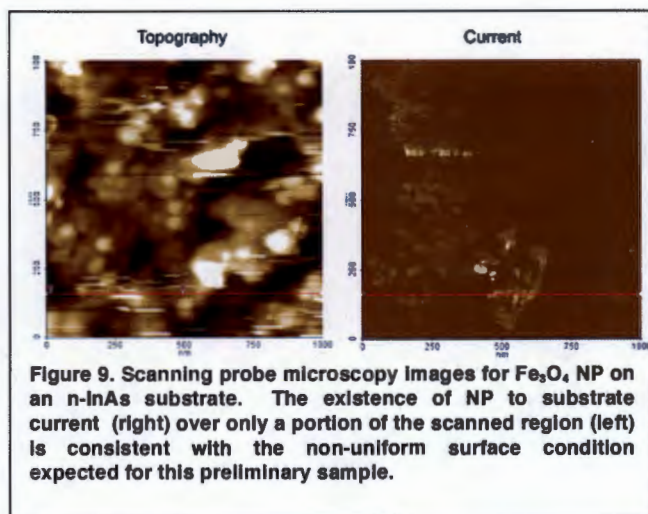
fabricating uniform arrays over large areas on GaAs. This is illustrated in Fig. 6. which shows two different magnifications of Fe<sub>3</sub>O<sub>4</sub> nanoparticles on GaAs.

The next step, creating covalent bonding between the NP and the substrate, involves a number of complications. The three main issues are 1) removal of surface oxides on the GaAs epi, 2) removal of organic shells from the nanoparticles, promotion of bonding between the NP and GaAs substrate. A good process for one step may lead to problems in another, so some process development is needed to optimize the overall protocol.



first strategy, we applied basic protocols for native oxide removal and for organic removal. Figure 7 shows results from an abrasion test designed to evaluate physical bonding of the nanoparticles to GaAs. As apparent from the SEM image on the right, the left image shows three regions: 1) the lower region which was never covered by nanoparticles, 2) the middle region, which is still covered by nanoparticles and 3) the upper region, where the nanoparticle were scraped away. Atomic force microscopy images revealed that the darker dots in the upper region correspond to protrusions in the surface. The results show that the NP are mechanically bonded to the surface.



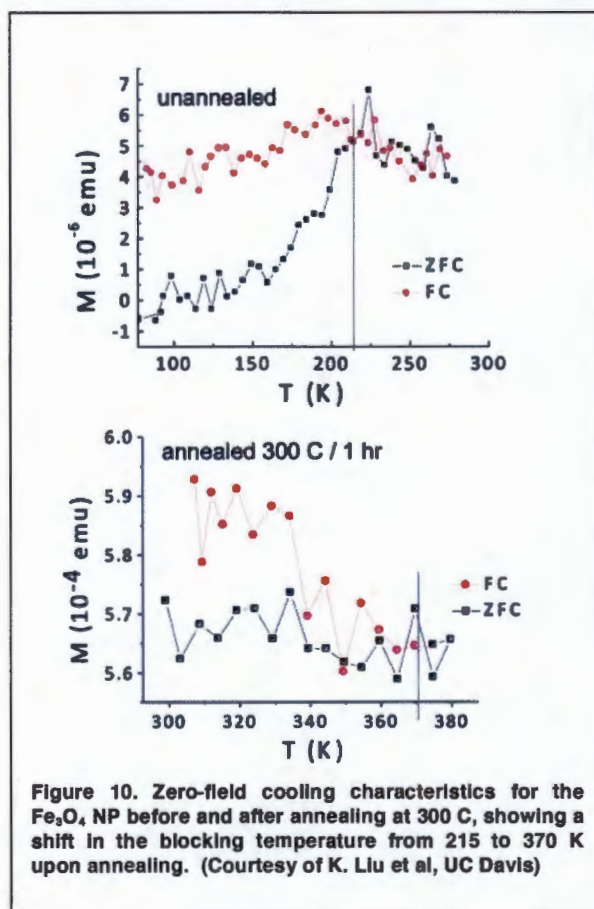


To examine the nature of the NP/substrate interface, **cross-sectional transmission electron microscopy** was carried out on the sample shown in Fig. 8. The TEM image in Fig. 8 shows that the bonding has been achieved in the annealing process while maintaining the crystallinity of the  $\text{Fe}_3\text{O}_4$  NP, as desired. However, the image reveals the presence of an amorphous layer of about 7 nm in thickness between the NP and the substrate. This layer is most likely composed of  $\text{Ga}_2\text{O}_3$  and  $\text{As}_2\text{O}_3$ , the well-known native oxides

for GaAs, possibly enhanced in thickness during the annealing process. Coupling between the NP and the substrate is necessary for substrate mediated exchange interactions. The oxide, which is about twice as thick as the native oxide on GaAs, introduces a tunneling barrier that would reduce electronic coupling. The TEM results therefore indicate that, despite the precautions taken to minimize oxide formation in these

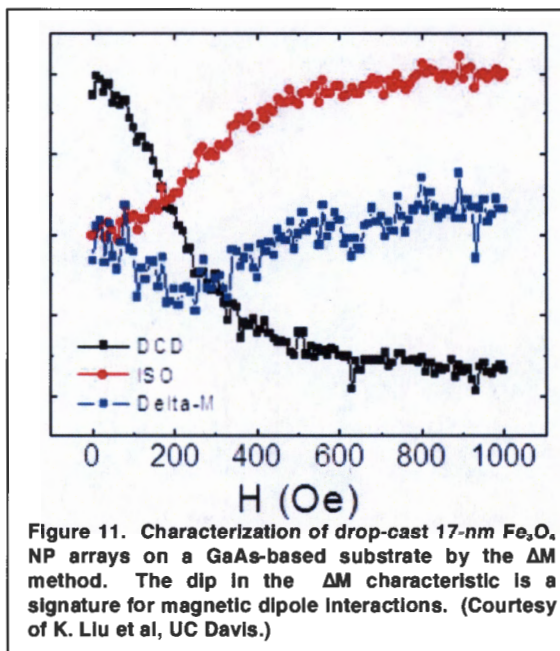
optimization of needed to the oxide in this

experiments, further the bonding protocol is reduce the thickness of structure.





NP/substrate coupling can also be enhanced by increasing the conductivity of the interfacial oxide. InAs, in particular, has two key advantages over GaAs for achieving electronic coupling between NP and the substrate: 1) the Fermi level is pinned in the conduction band allowing electrons to form at the surface with no depletion layer and 2) indium based oxides tend to be conducting (e.g., indium-tin oxide) and could provide a sufficiently conductive path. A number of experiments were carried out to investigate coupling of  $\text{Fe}_3\text{O}_4$  NP to InAs. Earlier on, we found anomalous sintering of NP at low temperature in the case of InAs substrates and therefore were forced to limit our annealing cycle to 150 C / 1 min, which was not sufficient for good bonding and limited our early progress. Fortunately, later we were able to anneal InAs samples at the 300 C / 1 hr, which is a cycle similar to that used for bonding to GaAs. We believe that the earlier anomalous results were due to degradation of the NP over time.



A number of promising results were obtained for InAs substrates during the final period of the project. First, we obtained **conductive atomic-force microscopy (I-AFM)** evidence of electrical contact between the  $\text{Fe}_3\text{O}_4$  NP and an n-InAs substrate. In this technique, current flow from the scanning probe tip through the NP and into the substrate was examined. Figure 9 shows results for topography and current in a sample of  $\text{Fe}_3\text{O}_4$  NP on n-InAs. The current image provides preliminary evidence of electronic coupling between the NP and the n-InAs substrate. The non-uniformity of the current within the field is consistent with the non-uniformity in the bonding that would be expected in this early stage of sample preparation. It is interesting to note that while the sample preparation protocol was similar to that for the GaAs substrates, and therefore the formation of surface oxides would also be expected in the InAs case, In-based oxides can be much more conductive than Ga-based oxides, thereby allowing coupling. Further study is underway to confirm this promising evidence for the achievement of NP/substrate electronic coupling.

A goal of this project is to demonstrate control of the magnetic interactions in NP arrays by electrically gated exchange interactions. Magnetometry techniques can be used to supplement the planned experiments on gated device structures by providing early, corroborating evidence on simpler structures. **For example zero-field cooling measurements** were used to examine the affect of annealing on the magnetic properties of the drop-case  $\text{Fe}_3\text{O}_4$  NP arrays. Figure 10 shows that a large shift in blocking temperature  $T_B$  from 215 K to 370 K occurs for a 300 C / 1 hour anneal, which is representative of the annealing cycle for our bonding process. The cooling

measurements and associated M-H characteristics of the sample show that at room temperature the arrays are superparamagnetic before annealing and ferromagnetic after annealing. We note that this shift in magnetic properties can be used to advantage in designing experiments. On the other hand, the large shift emphasizes an essential requirement for the control samples our experiments: the control samples must be subjected to *identical* annealing conditions since the thermal bonding process will produce substantial changes in the magnetic properties the NP themselves, which must be distinguished from the intended changes due substrate coupling.

A particularly useful method for supplementary characterization in our study is the  $\Delta M$  method (See M. T. Raman et al, Applied Physics Letters 94, 042507, 2009). This method is a type of first-order reversal technique based on VSM magnetometry which allows magnetic dipole and exchange interactions to be distinguished from one another. Characterization of the drop-cast  $\text{Fe}_3\text{O}_4$  NP arrays by the  $\Delta M$  method was carried out in preliminary experiments by the Kai Liu Group (UC Davis, Physics) to determine the sensitivity of the set-up for our test structures. Results are shown in Figure 11. The dip in the characteristic is expected in the case of magnetic dipole interactions. The results indicate that the set-up sensitivity should be sufficient for this measurement provided that the signal-to-noise ratio can be improved somewhat.

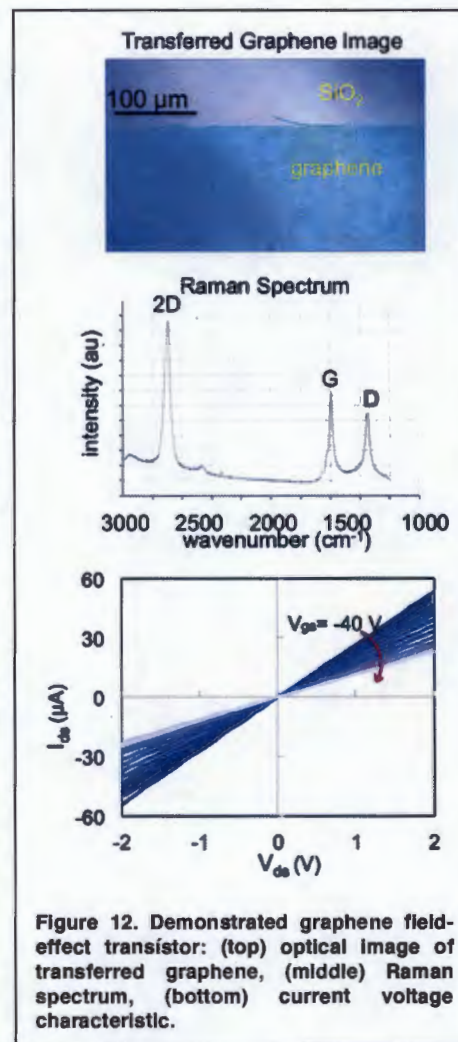


Figure 12. Demonstrated graphene field-effect transistor: (top) optical image of transferred graphene, (middle) Raman spectrum, (bottom) current voltage characteristic.

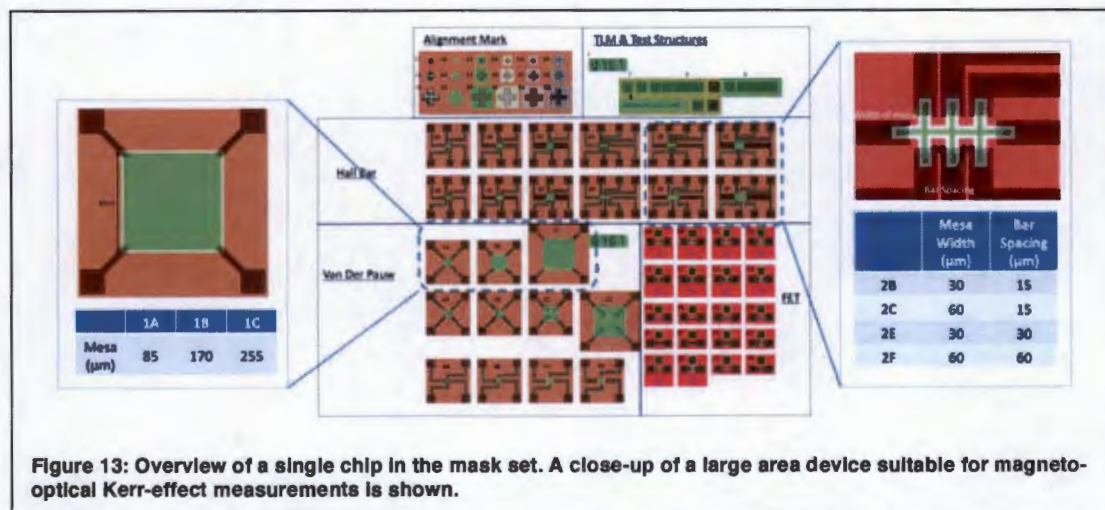
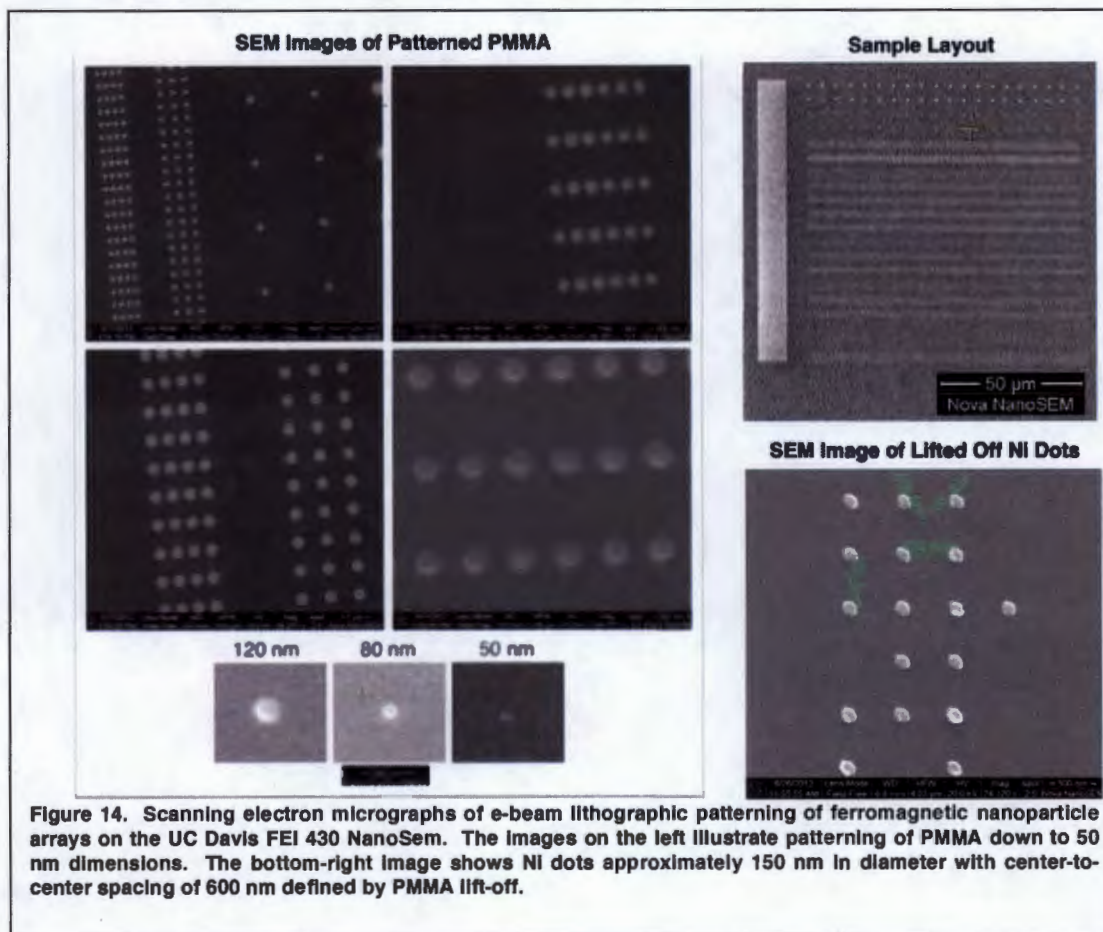


Figure 13: Overview of a single chip in the mask set. A close-up of a large area device suitable for magneto-optical Kerr-effect measurements is shown.



Although most of this report has focused on NP coupled through a 2DEG formed near the surface of a semiconductor, we devoted comparable effort toward coupling NP through the 2DEG formed in a layer of graphene. Thus far in the project, we have put into place the processing and characterization capabilities needed for fabricating graphene field-effect transistors. Figure 12 shows our results for the graphene transfer process, Raman spectrum and current-voltage characteristics of our devices. These results establish our capability for electrically contacting and gating graphene, as desired in this project. Figure 13 shows details of the mask set that we have developed for studying gated exchange interactions in the graphene and GaAs-based devices.



In  
a

parallel effort to our work on fabrication of NP arrays by “bottom-up” self-assembly, we recently initiated work on NP arrays fabricated by “top-down” electron-beam lithography (EBL) techniques with the intent of providing another path toward proof of concept of the gated exchange interaction concept. The fabrication of arrays by EBL patterning of deposited thin films allows some of the problems associated with the bottom-up approach (e.g., organic shell removal, oxide formation) to be circumvented. The trade-off for reduced process complexity is the larger size and spacing of EBL defined NP. Whereas, the assembly of 5 nm NP has been demonstrated routinely by our group and we have demonstrated assembly of NP as small as 1.5 nm, EBL defined NP are limited to several 10’s of nm or larger, with 100 nm being a practical limit for lifted off NP’s for high yield. Preliminary results on our work to push our EBL capability to its



limits for defining magnetic NP arrays are shown in Figure 14. We have been able to pattern 50 nm features, however, patterning of Ni dots by conventional PMMA lift-off of evaporated films has been limited so far to about 150-nm diameters. Therefore, we have begun the development of bi-layer lift-off schemes to push the achievable NP size and spacing to smaller dimensions. With bi-layer resist schemes, we expect to realize 50-nm metallic dots in close-packed arrays with our EBL system.

Although EBL patterning offers process advantages over self-assembly, the size limitation of EBL is a drawback. Indeed, the capability for achieving precision at nanometer-scale dimensions remains a key motivation for DNA-directed self-assembly. The NP size range of 5-20 nm seems optimal for our experiments since this range allows the magnetic properties  $\text{Fe}_3\text{O}_4$  NP to be size-tuned from superparamagnetic to ferromagnetic in the temperature range of interest. Furthermore, for optimal control of the exchange interaction, the NP spacing should correspond to the second node of the exchange integral  $J(x)$ , which occurs at half the Fermi-wavelength  $\lambda_F$  according to simple RKKY theory. Taking into account the dependence of  $\lambda_F$  on the 2DEG density and the accessible density range in our gated structures, 5-20 nm would also seem to be an ideal range for NP spacing. (Note that the optimal spacing in MacDonald's DFT calculations on exchange gating of cobalt NP on graphene is even below this range, however, graphene is a special case due to its bandstructure and the dependence of spacing on 2DEG density was not considered in those calculations.)

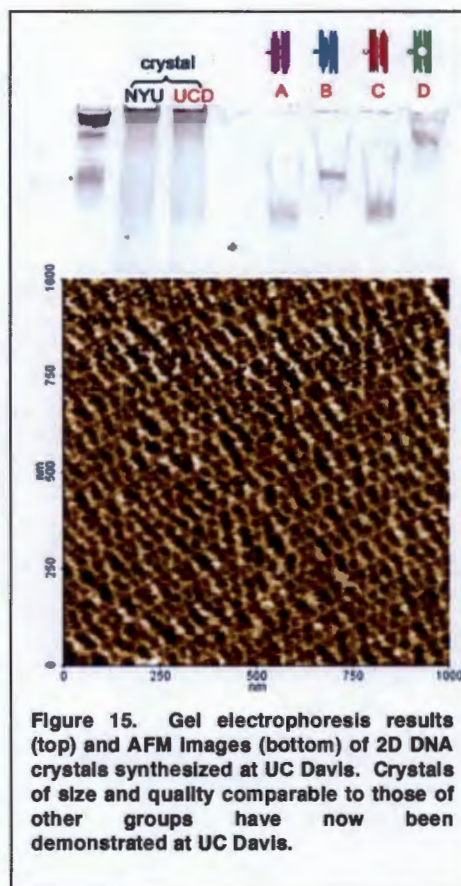


Figure 15. Gel electrophoresis results (top) and AFM images (bottom) of 2D DNA crystals synthesized at UC Davis. Crystals of size and quality comparable to those of other groups have now been demonstrated at UC Davis.

Although the 5-20 nm range of NP size and spacing is below the 50-100 nm limit for EBL patterned NP arrays, our investigation of EBL-defined arrays with larger dimensions is warranted for several reasons. First, the "optimal" 5-20 nm range is a rough estimate based on the density dependence of the wavevector in a free-electron model; the relevant wavevector for the RKKY model is strongly bandstructure dependent and could be substantially larger. In fact, this was the case in conventional GMR, where the optimal thickness of the normal-metal spacer layer in conventional multi-layer devices was found to be 5 to 10 times that originally predicted by simple RKKY theory. This is attributed to the fact that interzone scattering (Umklapp process) dominates over the intra-zone scattering for spacer materials having their minima near the Brillouin zone edge. Thus materials such as  $\text{Al}(0.3)\text{Ga}(0.7)\text{As}$ , Ge, and even Si may be advantageous for an initial proof of concept in large EBL defined structures.



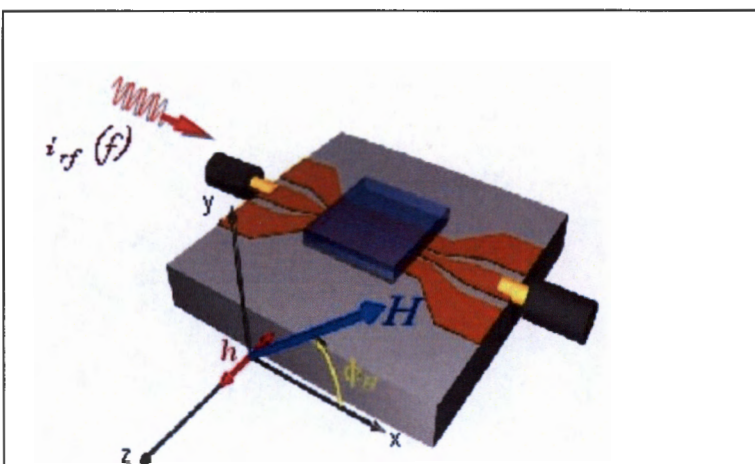
Although the work at UC Davis was primarily focused on drop-cast NP arrays, the fabrication of **2D DNA crystals** was successfully demonstrated during the last work period of the work UC Davis. While gel electrophoresis had confirmed good DNA tile formation by the UC Davis group earlier in the project, an error in the base sequence of one of the strands limited hampered large 2D crystal formation. Once the error was corrected, crystals of dimensions comparable to those of other groups were demonstrated at UC Davis, as shown in Fig. 15. Thus, the capability for using DNA-directed self-assembly to form optimized 2D NP arrays for this study is now in place at UC Davis.

## ***Spectroscopic studies of magnetic/coulombic NP arrays (ES-2).***

**Andrew D. Kent**

Kent's research in this project focused on the magnetic characterization of nanoparticle (NP) arrays. The main method Kent used was ferromagnetic resonance (FMR) spectroscopy, which is a powerful means to characterize NP particles and their interactions. In research period I, Kent's group demonstrated that the sensitivity of his FMR technique (see Fig. 1) was sufficient to characterize drop-cast close-packed arrays of Fe<sub>3</sub>O<sub>4</sub> NPs as well as layers only 4 NP thick. The FMR spectra of the 4-layer samples were similar to those of bulk (drop cast) material. It was determined that

improvements in sensitivity were needed to measure monolayer samples (i.e., strictly 2D arrays), and thus essential for the characterization of biological assembled layers, as these would be in the form of 2D arrays. Improvements in the FMR sensitivity required optimizing the coplanar waveguides used (reducing the their loss) for these experiments as well as using resonators, that is, waveguide structures with well-defined transmission resonances. Both methods were employed in Period II of the project.

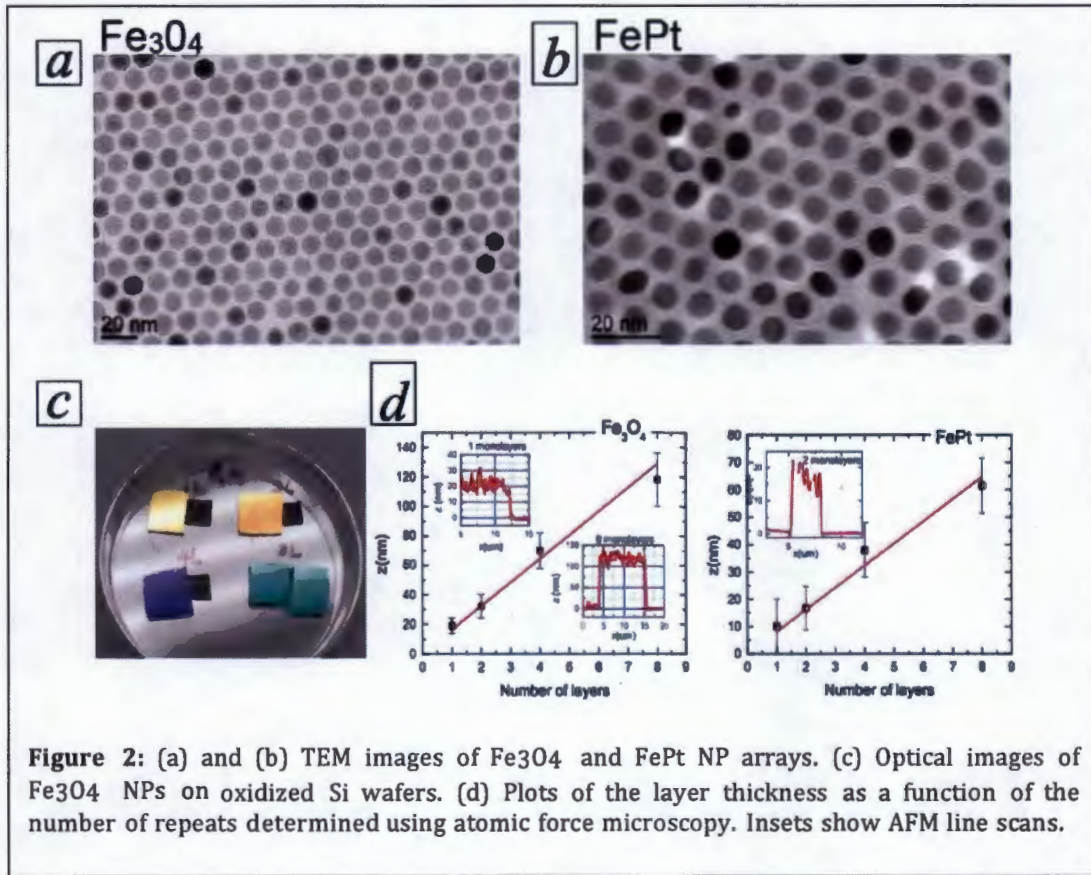


**Figure 1** shows the coplanar waveguide technique used in experiments on NP arrays. A substrate with NP arrays is mounted “flip chip” on a waveguide the transmission through the waveguide as a function of the applied field is used to determine the resonance condition— when the microwave frequency is resonant with magnetic excitation in the layer. The frequency range is 1 to 50 GHz.

In research period II we focused on characterizing 2D NP arrays (down to one monolayer of NPs), produced using a new method developed by **Murray's** group. Fe<sub>3</sub>O<sub>4</sub> and FePt NP samples were grown in a layer-by-layer fashion by Murray's group, as he reported in Nature in 2010. A drop of hexane solution with either Fe<sub>3</sub>O<sub>4</sub> or FePt nanocrystals spreads over the surface of diethylene glycol (DEG) in a Teflon well. The hexane is evaporated for 5-10 min and the solution formed a NP film supported on the DEG subphase surface. The transfer of the NP arrays to a substrate proceeded as follows: a substrate was placed under the floating film and then gently lifted up. In this way the silicon substrate became coated by a self-assembled NP of Fe<sub>3</sub>O<sub>4</sub> or FePt nanocrystals. We repeated the process several times with the same substrate to

obtain different number of NP repeats. We studied samples with 1,2,4 and 8 layers as well as bulk (many-layer drop cast) samples. Transmission electron microscopy (TEM) (Fig. 2a and b) of a 1-repeat samples showed that the layer is continuous, uniform in thickness and forms a hexagonal lattice for both  $\text{Fe}_3\text{O}_4$  and FePt. We have measured the particle size,  $r$ , and the distance between particles,  $d$ , and obtained for the  $\text{Fe}_3\text{O}_4$ ,  $r_{\text{FeO}} = 4.65 \text{ nm}$  and  $d_{\text{FeO}} = 11.30 \text{ nm}$  and for the FePt  $r_{\text{FePt}} = 3.50 \text{ nm}$  and  $d_{\text{FePt}} = 9.50 \text{ nm}$ . Figure 2c shows an optical image a set of  $\text{Fe}_3\text{O}_4$  NP samples with 1,2,4 and 8 repeats (and colors are uniform and the changes in color are due to thin film interference). AFM results (Fig. 2d) show that layers packed as close as the particles within a layer;  $\approx 15 \text{ nm}$  per layer for the  $\text{Fe}_3\text{O}_4$  and  $9 \text{ nm}$  for the FePt (see Fig. 1).

FMR spectroscopy was conducted with frequencies ranging from 4 to 40 GHz as a function of the applied field magnitude and angle (see Fig. 3 right for the experiment



geometry). To record the weak signals of the ultrathin magnetic layers we used a coplanar waveguide (CPW) with a smooth signal transmission within this frequency range. The absorption signal was recorded with the sample mounted flip-chip on the CPW. We show in Fig. 2 (left-hand-side panel) the spectra at fixed frequency for different samples with different numbers of monolayers. The signal-to-noise improves with the number of monolayers (i.e., with the volume of nanoparticles). We fitted the FMR data to determine the magnetic characteristics of the arrays.



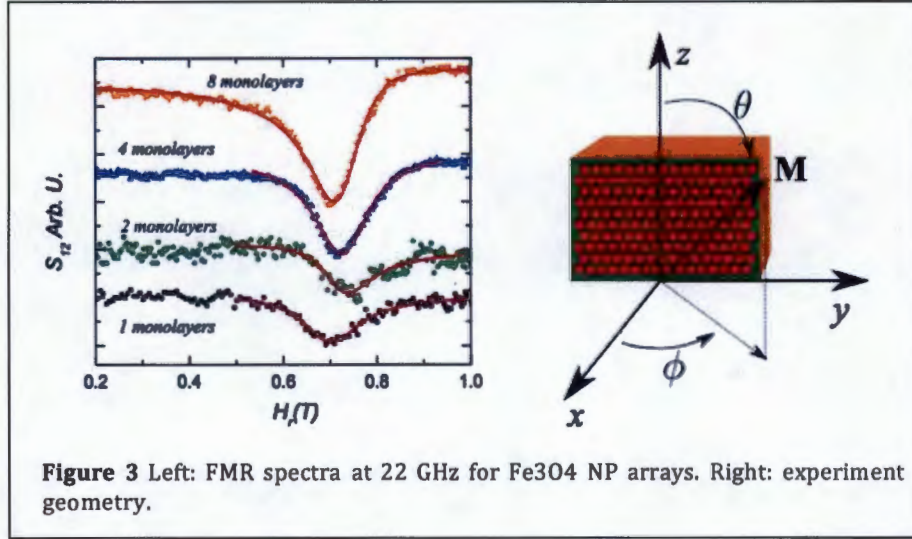
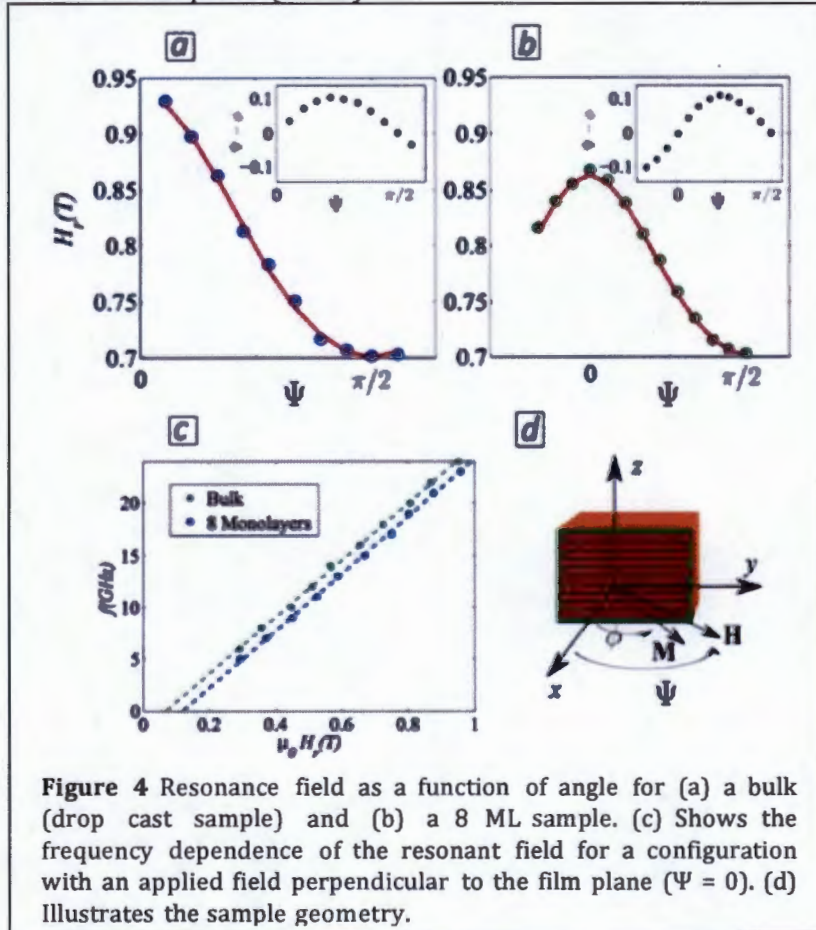
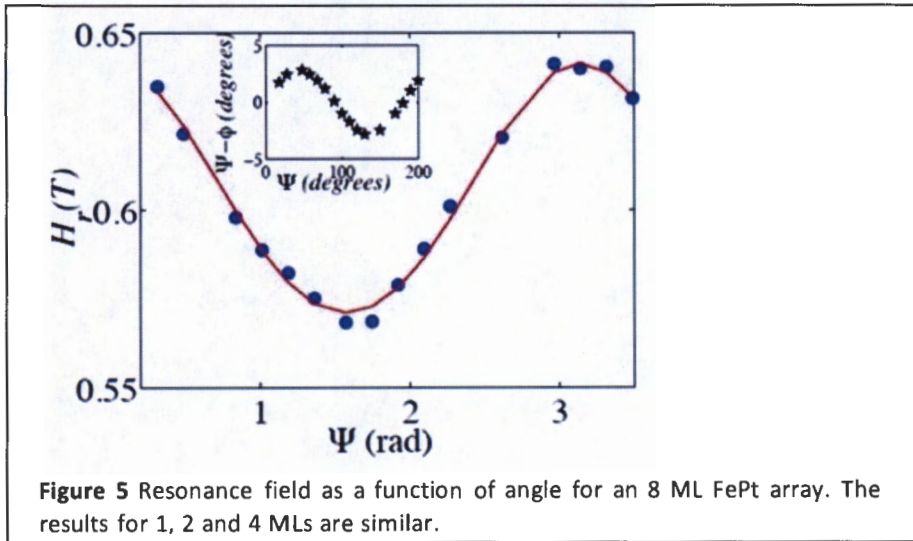


Figure 4a and 4b shows the angular dependence ( $\Psi$ ) of the resonant field ( $H_r$ ) and the corresponding fits to the data for Fe<sub>3</sub>O<sub>4</sub> samples. The inset shows the magnetization angles ( $\phi$ ) as a function of the applied field angle ( $\Psi$ ). We have also conducted measurements at different frequencies: Figure 4c shows the frequency dependence ( $f$ ) of the resonant field ( $H_r$ ) for a configuration with an applied field perpendicular to the film plane ( $\Psi = 0$ ). (d) illustrates the sample geometry.





An analysis of the FMR gives the array parameters shown in the tables to the right for both Fe<sub>3</sub>O<sub>4</sub> and FePt.

In both cases the effective magnetization increases in ML samples relative to bulk drop cast samples, but is about 30% less than expected for the magnetization density of the array. This is one of the

important results of our studies. The expected magnetization density of the array is based on considering the NP array as an effective medium with a material density determined by the particle packing density.

Fe <sub>3</sub> O <sub>4</sub>	$\frac{M_{\text{eff}}^2}{M_s} [\text{T}]$	$\frac{\gamma}{2\pi} [\frac{\text{GHz}}{\text{T}}]$	FePt	$\frac{M_{\text{eff}}^2}{M_s} [\text{T}]$	$\frac{\gamma}{2\pi} [\frac{\text{GHz}}{\text{T}}]$
1 Monolayer	0.139	28.3	1 Monolayer	-	-
2 Monolayers	0.147	29.1	2 Monolayers	0.0499	28.00
4 Monolayers	0.154	28.6	4 Monolayers	0.056	27.97
8 Monolayers	0.160	28.3	8 Monolayers	0.047	28.6
BULK	0.108	29.1	BULK	-	-

The improved model—developed in this project by McDonald—takes into account spatial variations of the magnetization in the array due to the discreteness of the particles. As a result there is a larger magnetostatic energy when the nanoparticles are magnetized in the plane. In an effective medium model the magnetostatic energy is zero when the magnetization is in the sample plane. As a result the effective medium model overestimates the anisotropy in the FMR response as a function of field angle, also giving a larger effective magnetization. McDonald finds that a lower effective magnetization is expected in NP arrays. This is associated with a non-negligible magnetostatic energy of arrays when their magnetization is in-plane. As described in section TS-1 the theory fits the FMR data well. The only input to the theory is the magnetic moment of the NPs, which we take from bulk data. It would be preferable to measure the magnetic

moment per particle—which we had planned to do but were not able to complete within this project. Nonetheless, this research demonstrated the effect of interparticle dipole interactions on the FMR response of NP arrays and provided the first FMR data on a single monolayer of magnetic NPs.



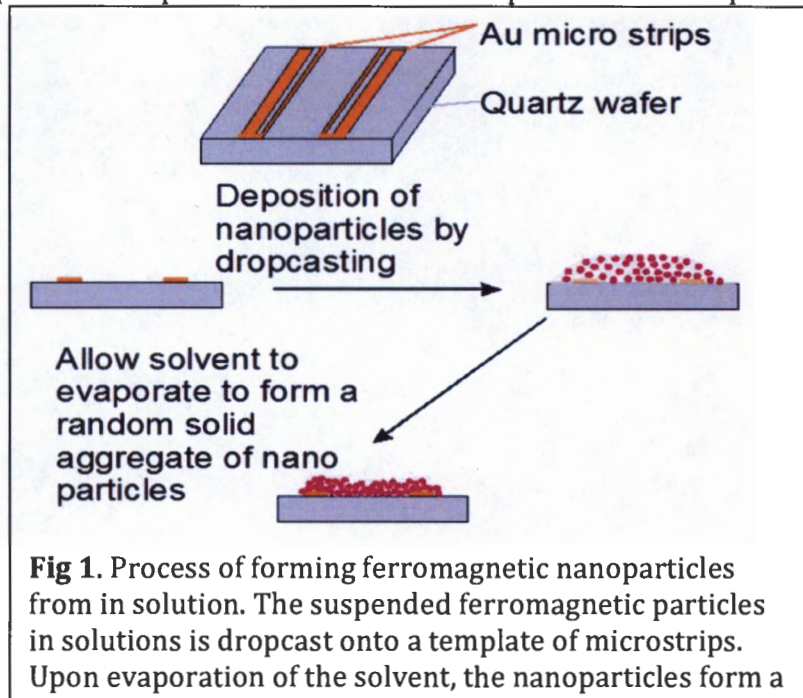
## Dynamic studies of spin transport in magnetic NP arrays (ES-3).

**Kang L. Wang**

During phase I of this project, emphasis was put on investigating the possibility of spinwave propagation through an ensemble of ferromagnetic nanoparticles. Uniform ferromagnetic nanoparticles in the size range of less than  $\sim 10\text{nm}$  were obtained from Murray's group. At these size ranges the particles are superparamagnetic at roomtemperature. A process for depositing these particles onto microstrip antennas for spinwave studies were developed as illustrated in Fig. 1. Ferromagnetic nanoparticles suspended in a solvent is dropcast onto a template

of microstrips. Upon evaporation of the solvent, the nanoparticles form a semic-random closed packed aggregate. Since the nanoparticles are coated with a organic ligand of roughly  $\sim 1\text{nm}$  thickness, the smallest edge to edge distance between the ferromagnetic nanoparticles achieved is  $\sim 2\text{nm}$ . This distance is too far to achieve strong exchange coupled particles, however

there are indications of weaker dipole-dipole interactions as evidenced by superconducting quantum interference device (SQUID) measurements of the dropcast aggregates.



**Fig 1.** Process of forming ferromagnetic nanoparticles from in solution. The suspended ferromagnetic particles in solutions is dropcast onto a template of microstrips. Upon evaporation of the solvent, the nanoparticles form a

Superparamagnetic particles are characterized by the Langevin function

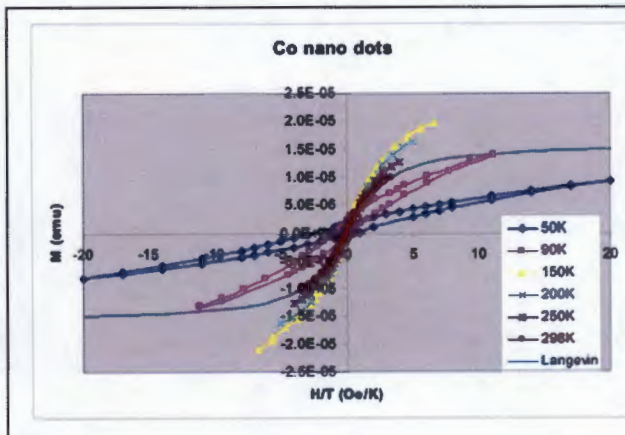
$$M = M_s L(x),$$

$$L(x) = \coth(x) - \frac{1}{x},$$

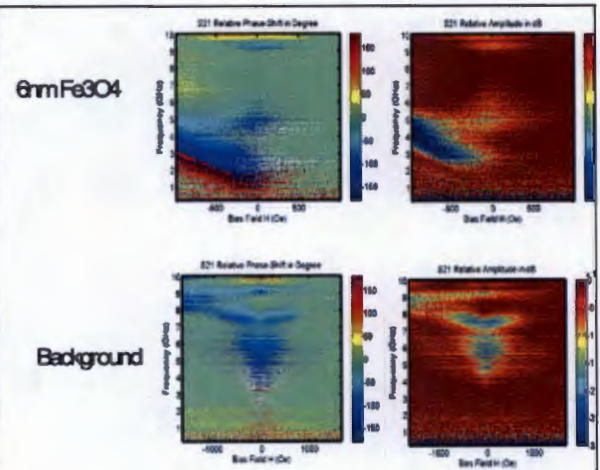
$$x = \mu H / k_B T$$

where,  $M_s$  is the saturation magnetization,  $H$  the external applied magnetic field and  $k_B$  is the Boltzmann constant. As Fig. 2. shows, the SQUID hysteresis loops of the Co nano particle aggregates do not fit the langevin equation. Moreover, the hysteresis

curve shows a weak coercive field, indicative of interacting particles rather than pure non-interacting superparamagnetic particles.



**Fig 2.** Magnetic hysteresis loops of nanoparticle aggregates



**Fig. 3.** Spinwave propagation measurements across microstrip antennas separated by 4 micrometer and covered by superferromagnetic nanoparticlres

Due to the very weak interaction between the spinwave propagation to be poor, i.e. highly damped measurements confirm very weak signal to noise separated by only 4 microns apart (see Fig. 3). background signal before dropcasting the nanoparticle aggregate is barely detectable. The dispersion for surface mode spinwaves (Damo) The fitting to the data is shown in Fig. 4.

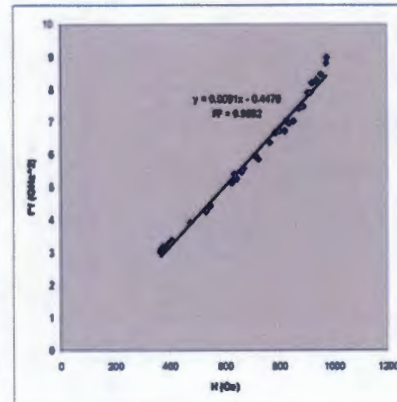
The spinwave measurments are performed on aggs sets of nanoparticles each with a different size. saturation magnetization can be extracted from extracted saturation magnetization values are shown Fig. 5. summarizes the three different saturation from the spinwave measurements plotted against the shown the size dependence of the saturation m empirical equation:

$$\frac{M_s(D)}{M_s(Bulk)} = 1 - t/D$$

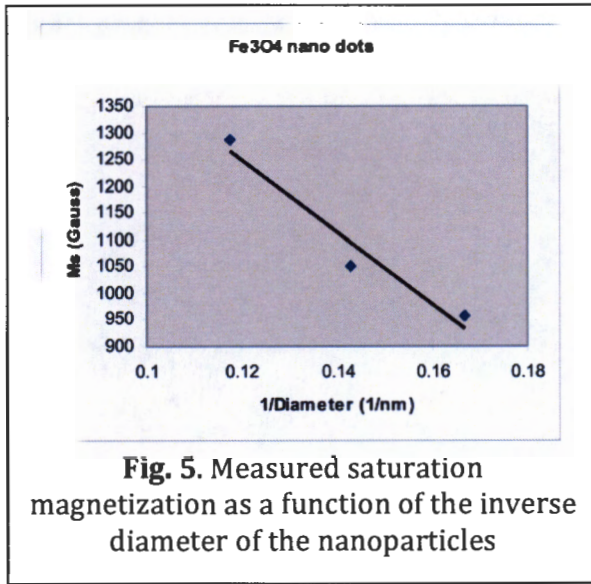
where  $t$  is a fitting parameter and  $D$  is the diameter of the nanoparticles.

From the spinwave propagation measurements performed during phase I of this project, it was concluded the damping of the spinwaves is too large in nano-aggregates compared to thin films of the same material. In order to lower the damping and increase the spinwave propagation signal, the nanoparticles needs to

**Fig. 4** The resonance features seen in fig. 3 fitted to surface mode spinwave dispersion formula



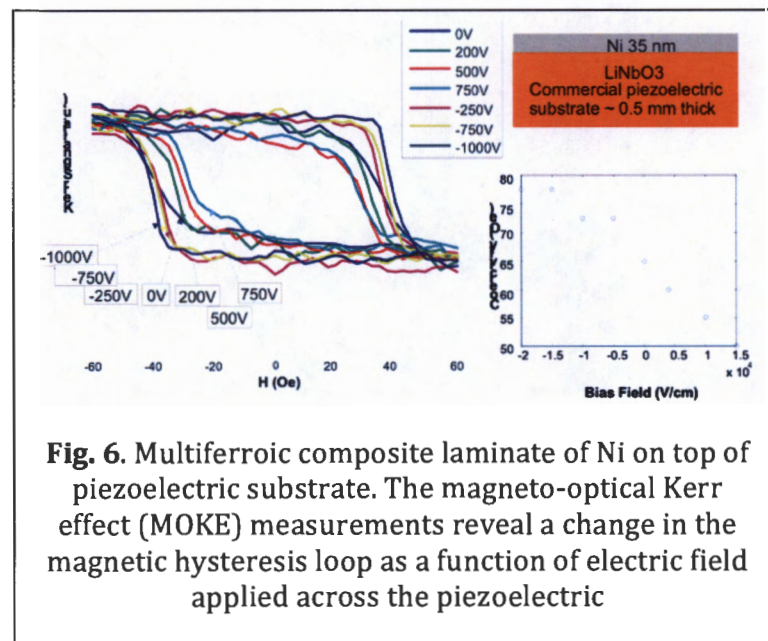


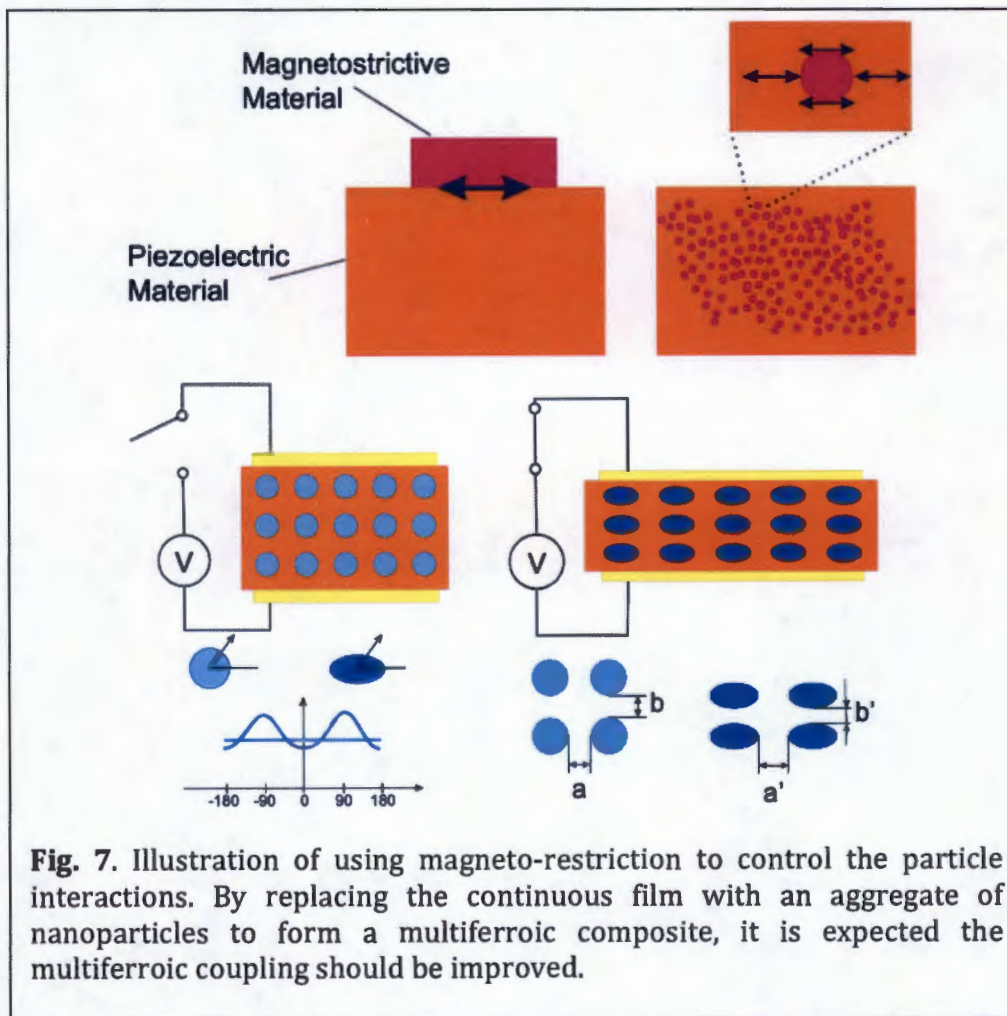


The idea is to replace the continuous Ni film with a nanoparticle aggregate. A modification of the strain level on the substrate will affect both the magnetic nanoparticles intrinsically via its magnetostriction, but also by changing the distance between the nanoparticles in the aggregate, hence affecting their inter-particle interaction. This idea is illustrated in fig. 7. By integrating nanoparticles into a piezoelectric material, the mechanical coupling of the strain response from the piezoelectric to the nanoparticles should also be enhanced compared to laminate film structures.

be substantially closer to each other, i.e. edge-to-edge separation of  $\sim 0.2$  nm rather than the current  $\sim 2$  nm.

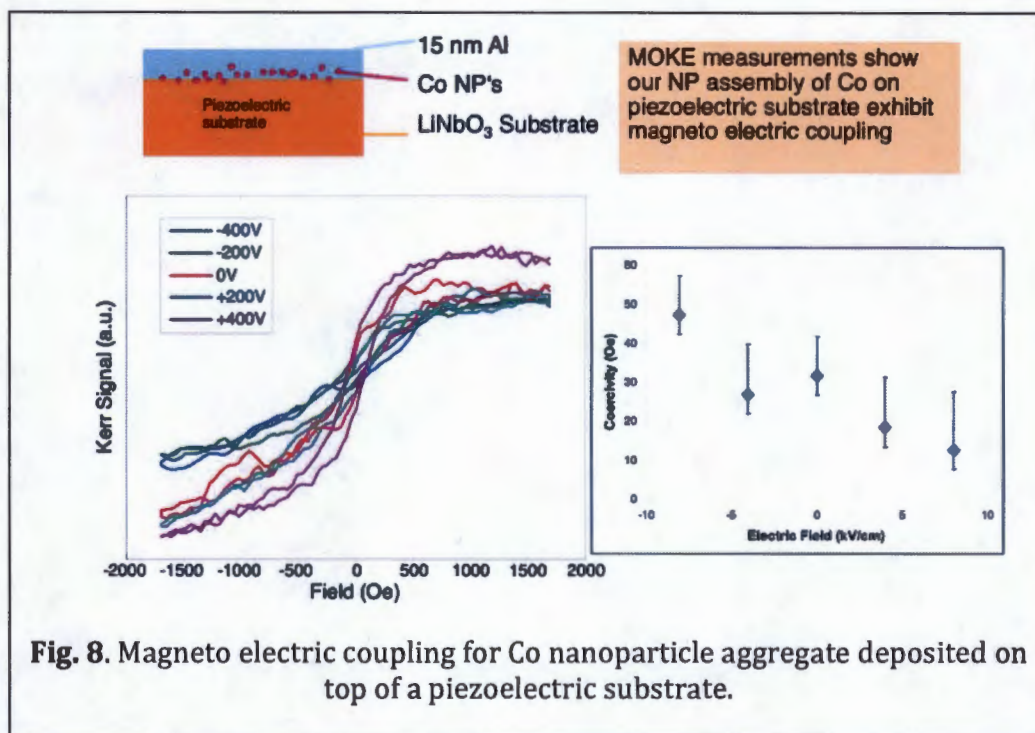
For phase II, an alternative approach to study the multiparticle interaction is proposed utilizing multiferroic materials. The principle is illustrated in fig.6. A magnetostrictive layer of Ni is deposited on top of a piezoelectric substrate. As an electric field is applied across the piezoelectric, a strain response is coupled to the Ni film which will change its magnetic properties subject to its magnetostriction and the strain response.





We have implemented this idea in various nanoparticle systems by developing novel laminate structure consisting of piezoelectric substrate coated with nanoparticle aggregate and subsequently covered by another non magnetic metal layer for enhancing the mechanical strain coupling. Using the described approach with Co nanoparticles, it is shown an electric field applied across the piezoelectric does indeed modify the magnetic hysteresis curve as shown in fig. 8.





Although these results are very promising in realizing a nanoparticle system with tunable interactions, the magnetic modulation in the present system is probably not due to any change of the inter-particle interaction. Control measurements probing the blocking temperature of the this sample at different electric fields did not reveal any shifts, supporting the interpretation the interparticle interaction, if any, is not modulated by electric fields.

The above results conclude phase II of the spinwave studies of nanoparticle aggregates. The conclusion is the nanoparticles needs to be packed closer to each other in order to form a strong exchange interaction required for strong spinwave signal. If such system can be found, integration of such particles into a piezoelectric material may lead to a tunable interacting system, where an electric field can be used to change the nature of the coupling mechanisms between the nanoparticles by simply changing their edge-to-edge separation.

## Core/shell NP synthesis (NP-1). Christopher B. Murray

### ACCOMPLISHMENTS PERIOD 1

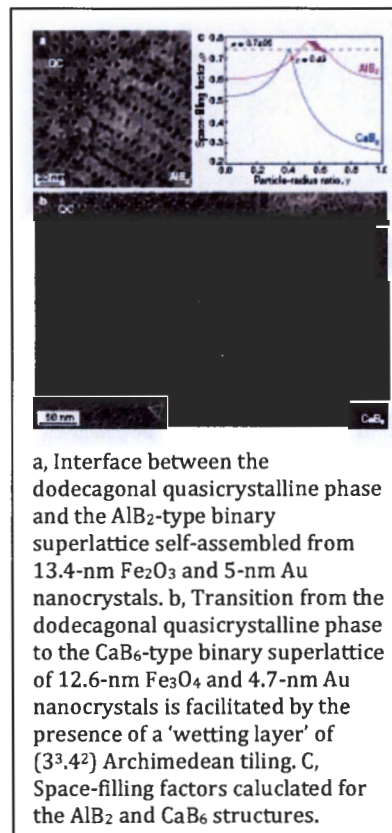
#### Quasicrystalline order in self-assembled binary nanoparticle superlattices

Dmitri V. Talapin, Elena V. Shevchenko, Maryna I. Bodnarchuk, Xingchen Ye, Jun Chen & Christopher B. Murray

*Nature* **2009**, 461, 964-967

The discovery of quasicrystals in 1984 changed our view of ordered solids as periodic structures and introduced new long-range ordered phases lacking any translational symmetry. Quasicrystals permit symmetry operations forbidden in classical crystallography, for example five-, eight-, ten- and 12-fold rotations, yet have sharp diffraction peaks. Intermetallic compounds have been observed to form both metastable and energetically stabilized quasicrystals; quasicrystalline order has also been reported for the tantalum telluride phase with an approximate  $Ta_{1.6}Te$  composition. Later, quasicrystals were discovered in soft matter, namely supramolecular structures of organic dendrimers and tri-block copolymers<sup>8</sup>, and micrometre-sized colloidal spheres have been arranged into quasicrystalline arrays by using intense laser beams that create quasi-periodic optical standing-wave patterns. Here we show that colloidal inorganic nanoparticles can self-assemble into binary aperiodic superlattices. We observe formation of assemblies with dodecagonal quasicrystalline order in different binary nanoparticle systems: 13.4-nm  $Fe_2O_3$  and 5-nm

Au nanocrystals, 12.6-nm  $Fe_3O_4$  and 4.7-nm Au nanocrystals, and 9-nm PbS and 3-nm Pd nanocrystals. Such compositional flexibility indicates that the formation of quasicrystalline nanoparticle assemblies does not require a unique combination of interparticle interactions, but is a general sphere-packing phenomenon governed by the entropy and simple interparticle potentials. We also find that dodecagonal quasicrystalline superlattices can form low-defect interfaces with ordinary crystalline binary superlattices, using fragments of  $(3^3.4^2)$  Archimedean tiling as the 'wetting layer' between the periodic and aperiodic phases.



a, Interface between the dodecagonal quasicrystalline phase and the  $AlB_2$ -type binary superlattice self-assembled from 13.4-nm  $Fe_2O_3$  and 5-nm Au nanocrystals. b, Transition from the dodecagonal quasicrystalline phase to the  $CaB_6$ -type binary superlattice of 12.6-nm  $Fe_3O_4$  and 4.7-nm Au nanocrystals is facilitated by the presence of a 'wetting layer' of  $(3^3.4^2)$  Archimedean tiling. c, Space-filling factors calculated for the  $AlB_2$  and  $CaB_6$  structures.

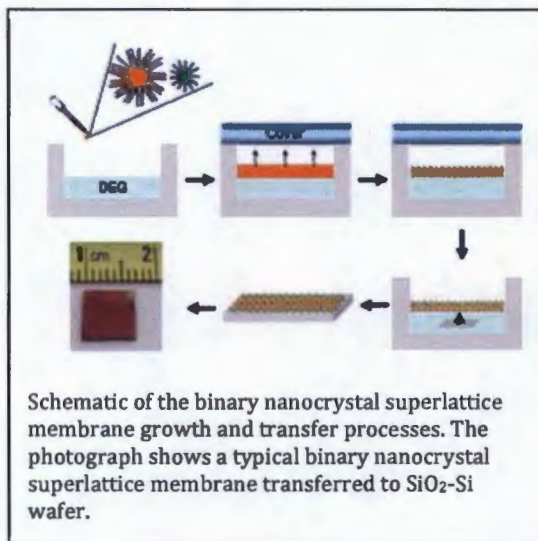
#### Binary Nanocrystal Superlattice Membranes Self-assembled at the Liquid–Air Interface

Angang Dong, Jun Chen, Patrick M. Vora, James M. Kikkawa & Christopher B. Murray

*Nature* **2010**, 466, 474-477



**ABSTRACT:** The spontaneous organization of multicomponent micrometer sized colloidal or nanocrystals into superlattices is of scientific importance for understanding the assembly process on the nanometer scale and is of great interest for bottom-up fabrication of functional devices. In particular, co-assembly of two types of nanocrystal into binary nanocrystal superlattices (BNSLs) has recently attracted significant attention, as this provides a low cost, programmable way to design metamaterials with precisely controlled properties that arise from the organization and interactions of the constituent nanocrystal components. Although challenging, the ability to grow and manipulate large-scale BNSLs is critical for extensive exploration of this new class of material. Here we report a general method of growing centimetre-scale, uniform membranes of BNSLs that can readily be transferred to arbitrary substrates. Our method is based on the liquid-air interfacial assembly of multicomponent nanocrystals and circumvents the limitations associated with the current assembly strategies, allowing integration of BNSLs on any substrate for the fabrication of nanocrystal-based devices. We demonstrate the construction of magnetoresistive devices by incorporating large-area (1.5 mm \* 2.5 mm) BNSL membranes; their magnetotransport measurements clearly show that device magnetoresistance is dependent on the structure (stoichiometry) of the BNSLs. The ability to transfer BNSLs also allows the construction of free-standing membranes and other complex architectures that have not been accessible previously.

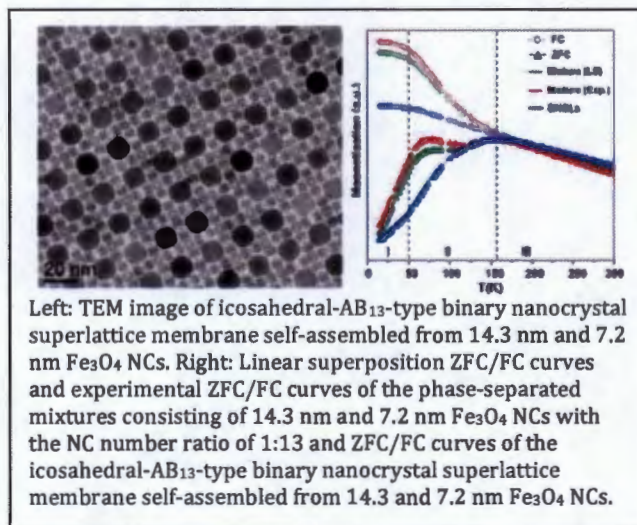


### Collective Dipolar Interactions in Self-Assembled Magnetic Binary Nanocrystal Superlattice Membranes

Jun Chen, Angang Dong, Jing Cai, Xingchen Ye, Yijin Kang, James M. Kikkawa, and Christopher B. Murray

*Nano Lett.* **2010**, 10, 5103-5108

**ABSTRACT:** Co-assembly of two types of nanocrystals (NCs) into binary NC superlattices (BNSLs) provides a solution-based, inexpensive way to create novel metamaterials with rationally designed properties. The fundamental challenge is to probe and understand the nature



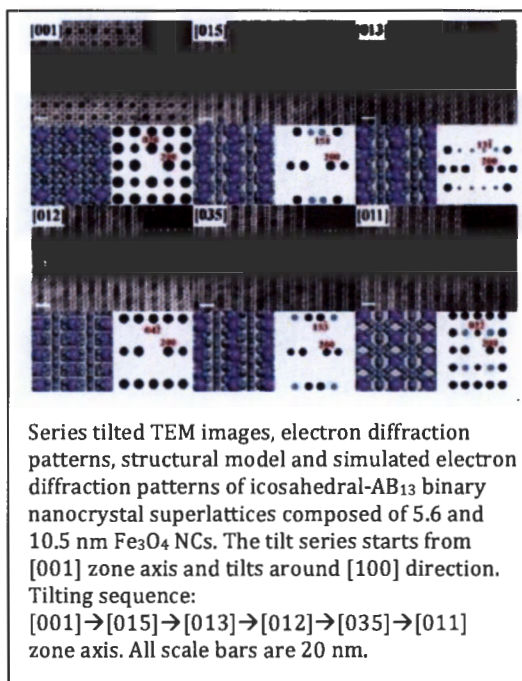
and extent of complex interparticle interactions present in BNSLs, which can lead to collective properties that differ from their dispersed constituents or phase-separated counterparts. Here, we report the growth and magnetic characterization of large-area ( $\sim 1 \text{ cm}^2$ ) BNSL membranes self-assembled from distinct magnetic NCs at the liquid-air interface. The resulting BNSL membranes exhibit a single-phase-like magnetization alignment process, which is not observed in the phase-separated NC mixtures having the same stoichiometry. This single-phase-like magnetic behavior is attributed to the collective interparticle dipolar interactions between two NC components in BNSLs, corroborated by calculation of the random dipolar fields as well as Monte Carlo simulation. The collective magnetic properties are demonstrated in magnetic BNSL membranes having different structures (stoichiometry) and different NC combinations.

### Systematic Electron Crystallographic Studies of Self-Assembled Binary Nanocrystal Superlattices

Jun Chen, Xingchen Ye, & Christopher B. Murray

*Acs Nano* **2010**, 4, 2374-2381

**ABSTRACT:** Multicomponent nanocrystal assemblies have received great attention due to their fundamental role in the study of self-assembly and novel physical properties arising from particle interactions. Here, we report the formation of the first binary nanocrystal superlattices (BNSLs) consisting of different-sized  $\text{Fe}_3\text{O}_4$  nanocrystals. We establish a framework to systematically study the structure of BNSLs using a dual-axis tomography TEM holder. The tilt series obtained not only allows us to map the three-dimensional (3D) structure of icosahedral  $\text{AB}_{13}$  (ico- $\text{AB}_{13}$ ) and  $\text{AlB}_2$ -type BNSLs but also uncovers the structural differences among the projections of ico- $\text{AB}_{13}$ , cuboctahedral  $\text{AB}_{13}$  (cub- $\text{AB}_{13}$ ), and  $\text{AlB}_2$ . This structural characterization method is general and is important for further exploration of structural diversity in BNSLs and in the development of rigorous structure property relationships in BNSLs. The formation of ico- $\text{AB}_{13}$  and  $\text{AlB}_2$  BNSLs from electrostatically neutral  $\text{Fe}_3\text{O}_4$  nanoparticles is consistent with the space-filling principles and further supports entropy as the dominant factor during the growth of these BNSLs.



## ACCOMPLISHMENTS PERIOD 2

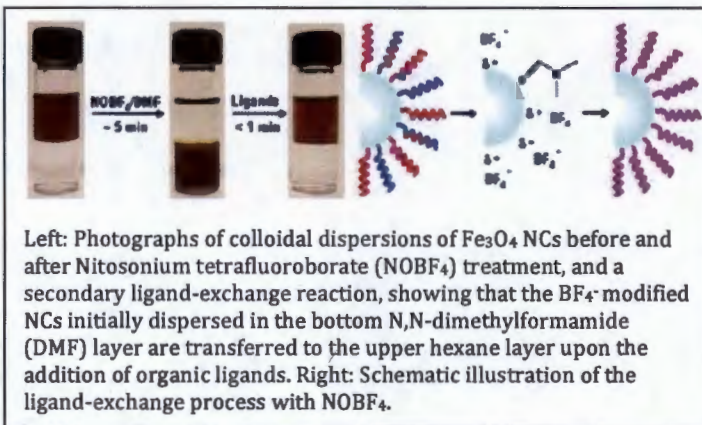
### A Generalized Ligand-Exchange Strategy Enabling Sequential Surface Functionalization of Colloidal Nanocrystals



Angang Dong, Xingchen Ye, Jun Chen, Yijin Kang, Thomas Gordon, James M. Kikkawa, and Christopher B. Murray

*J. Am. Chem. Soc.* **2011**, 133, 998-1006

**ABSTRACT:** The ability to engineer surface properties of nanocrystals (NCs) is important for various applications, as many of the physical and chemical properties of nanoscale materials are strongly affected by the surface chemistry. Here, we report a facile ligand-exchange approach, which enables sequential surface



Left: Photographs of colloidal dispersions of  $\text{Fe}_3\text{O}_4$  NCs before and after Nitrosonium tetrafluoroborate ( $\text{NOBF}_4$ ) treatment, and a secondary ligand-exchange reaction, showing that the  $\text{BF}_4^-$  modified NCs initially dispersed in the bottom N,N-dimethylformamide (DMF) layer are transferred to the upper hexane layer upon the addition of organic ligands. Right: Schematic illustration of the ligand-exchange process with  $\text{NOBF}_4$ .

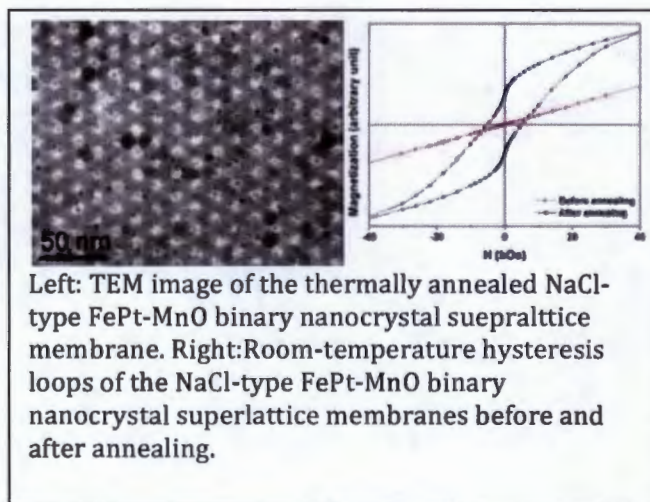
functionalization and phase transfer of colloidal NCs while preserving the NC size and shape. Nitrosonium tetrafluoroborate ( $\text{NOBF}_4$ ) is used to replace the original organic ligands attached to the NC surface, stabilizing the NCs in various polar, hydrophilic media such as N,N-dimethylformamide for years, with no observed aggregation or precipitation. This approach is applicable to various NCs (metal oxides, metals, semiconductors, and dielectrics) of different sizes and shapes. The hydrophilic NCs obtained can subsequently be further functionalized using a variety of capping molecules, imparting different surface functionalization to NCs depending on the molecules employed. Our work provides a versatile ligand-exchange strategy for NC surface functionalization and represents an important step toward controllably engineering the surface properties of NCs.

### Enhanced Thermal Stability and Magnetic Properties in NaCl-Type FePt-MnO Binary Nanocrystal Superlattices

Angang Dong, Jun Chen, Xingchen Ye, James M. Kikkawa, and Christopher B. Murray

*J. Am. Chem. Soc.* **2011**, 133, 13296-13299

**ABSTRACT:** We report the growth of NaCl-type binary nanocrystal (NC) superlattice membranes by coassembly of FePt and MnO NCs at the liquid-air interface. The constituent FePt NCs were converted into the hard magnetic  $\text{L}_{10}$  phase by thermal annealing



Left: TEM image of the thermally annealed NaCl-type FePt-MnO binary nanocrystal superlattice membrane. Right: Room-temperature hysteresis loops of the NaCl-type FePt-MnO binary nanocrystal superlattice membranes before and after annealing.



at 650 °C without degradation of the long-range NC ordering. In contrast, both FePt-only NC superlattices and FePt-MnO disordered NC mixtures showed substantial FePt sintering under the same annealing conditions. Our results demonstrate that the incorporation of FePt NCs into binary superlattices can solve the problems of FePt sintering during conversion to the  $L_{10}$  phase, opening a new route to the fabrication of ordered ferromagnetic NC arrays on a desired substrate for high-density data storage applications.

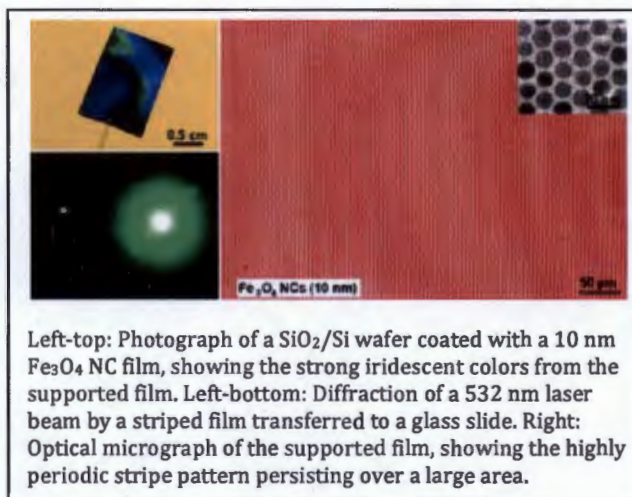
### Multiscale Periodic Assembly of Striped Nanocrystal Superlattice Films on a Liquid Surface

Angang Dong, Jun Chen, Soong Ju Oh, Weon-kyu Koh, Faxian Xiu, Xingchen Ye, Dong-Kyun Ko, Kang L. Wang, Cherie R. Kagan, and Christopher B. Murray

*Nano Lett.* **2011**, 11, 841-846

**ABSTRACT:** Self-assembly of nanocrystals (NCs) into periodically ordered structures on multiple length scales and over large areas is crucial to the manufacture of NC-based devices. Here, we report an unusual yet universal approach to rapidly assembling hierarchically organized NC films that display highly periodic,

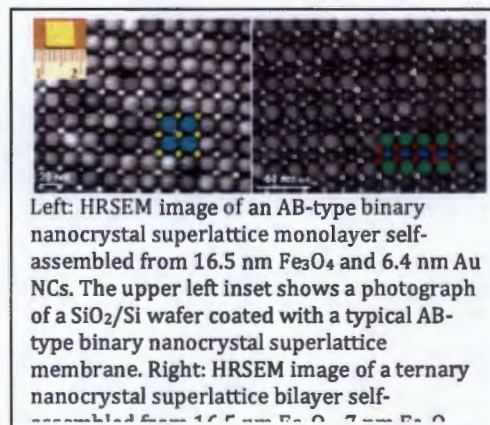
tunable microscale stripe patterns over square centimeter areas while preserving the local superlattice structure. Our approach is based on a drying-driven dynamic assembly process occurring on a liquid surface with the stripe pattern formed by a new type of contact-line instability. Periodic ordering of NCs is realized on microscopic and nanoscopic scales simultaneously without the need of any specialized equipment or the application of external fields. The striped NC superlattice films obtained can be readily transferred to arbitrary substrates for device fabrication. The periodic structure imparts interesting modulation and anisotropy to the properties of such striped NC assemblies. This assembly approach is applicable to NCs with a variety of compositions, sizes, and shapes, offering a robust, inexpensive route for large-scale periodic patterning of NCs.



### Two-Dimensional Binary and Ternary Nanocrystal Superlattices: The Case of Monolayers and Bilayers

Angang Dong, Xingchen Ye, Jun Chen, and Christopher B. Murray

*Nano Lett.* **2011**, 11, 1804-1809





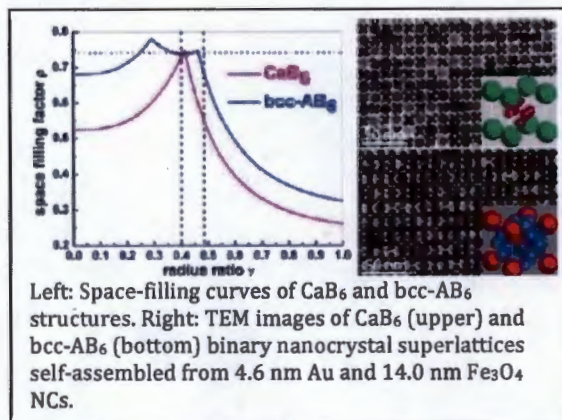
**ABSTRACT:** The modular assembly of multicomponent nanocrystal (NC) superlattices enables new metamaterials with programmable properties. While self-assembly of three-dimensional (3D) binary NC superlattices (BNSLs) has advanced significantly in the past decade, limited progress has been made to grow 2D BNSLs such as monolayers and bilayers over extended areas. Here, we report the growth of large-area ( $\sim 1 \text{ cm}^2$ ), transferable BNSL monolayers using the liquid-air interfacial assembly approach. The BNSL monolayers are formed by an entropy-driven assembly process with structures tunable by varying the NC size ratio. We further demonstrate the liquid-air interfacial assembly of BNSL bilayers which exhibit unique superlattice structures that have not been observed in the 3D BNSLs. As a further extension, bilayered ternary NC superlattices (TNSLs) are obtained by the cocrystallization of three types of NCs at the liquid-air interface.

### Polymorphism in Self-Assembled $\text{AB}_6$ Binary Nanocrystal Superlattices

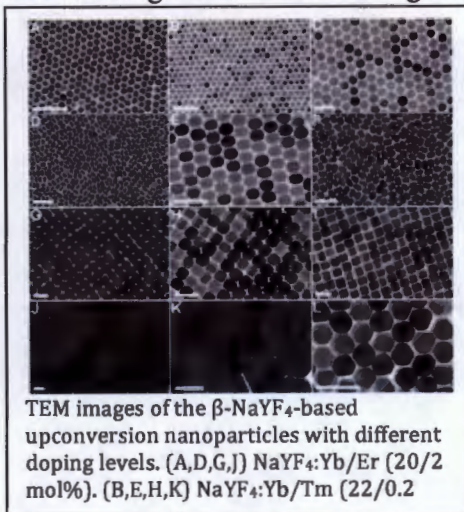
Xingchen Ye, Jun Chen, and Christopher B. Murray

*J. Am. Chem. Soc.* **2011**, 133, 2613-2620

**ABSTRACT:** We report the formation and systematic structural characterization of a new  $\text{AB}_6$  polymorph with the body centered cubic (bcc) symmetry in binary nanocrystal superlattices (BNSLs). The bcc- $\text{AB}_6$  phase, lacking any atomic analogue, is isomorphic to certain alkali-metal intercalation compounds of fullerene  $\text{C}_{60}$  (e.g.,  $\text{K}_6\text{C}_{60}$ ). On the basis of the space-filling principle, we further tailor the relative phase stability of the two  $\text{AB}_6$  polymorphs— $\text{CaB}_6$  and bcc- $\text{AB}_6$ —from coexistence to phase-pure bcc- $\text{AB}_6$ , highlighting the entropic effect as the main driving-force of the self-organization of BNSLs. We also discuss the implication of



Left: Space-filling curves of  $\text{CaB}_6$  and bcc- $\text{AB}_6$  structures. Right: TEM images of  $\text{CaB}_6$  (upper) and bcc- $\text{AB}_6$  (bottom) binary nanocrystal superlattices self-assembled from 4.6 nm Au and 14.0 nm  $\text{Fe}_3\text{O}_4$  NCs.



TEM images of the  $\beta$ - $\text{NaYF}_4$ -based upconversion nanoparticles with different doping levels. (A,D,G,J)  $\text{NaYF}_4\text{:Yb/Er}$  (20/2 mol%). (B,E,H,K)  $\text{NaYF}_4\text{:Yb/Tm}$  (22/0.2 mol%).

surface topology studies and the observation of twinning and preferential orientation in bcc- $\text{AB}_6$  on the growth mechanism of BNSLs. Furthermore, the connection between the bcc- $\text{AB}_6$  phase and the  $(3^2.4.3.4)$  Archimedean tiling shows the promise of further exploration on the structural diversity (both periodic and aperiodic) in this emerging class of metamaterials. The identification and the ability to tune the relative phase stability of polymorphic structures provide a unique opportunity to engineer the interparticle coupling through controlled clustering and/or interconnectivity of sublattice in BNSLs with identical stoichiometry.

### Morphologically controlled synthesis of colloidal upconversion nanophosphors and their shape-directed self-assembly

Xingchen Ye, Joshua E. Collins, Yijin Kang, Jun Chen, Daniel T. N. Chen, Arjun G. Yodh, and Christopher B. Murray

*Proc. Natl. Acad. Sci. U. S. A.* **2010**, 107, 22430-22435

**ABSTRACT:** We report a one-pot chemical approach for the synthesis of highly monodisperse colloidal nanophosphors displaying bright upconversion luminescence under 980 nm excitation. This general method optimizes the synthesis with initial heating rates up to 100 °C/minute generating a rich family of nanoscale building blocks with distinct morphologies (spheres, rods, hexagonal prisms, and plates) and upconversion emission tunable through the choice of rare earth dopants. Furthermore, we employ an interfacial assembly strategy to organize these nanocrystals (NCs) into superlattices over multiple length scales facilitating the NC characterization and enabling systematic studies of shape-directed assembly. The

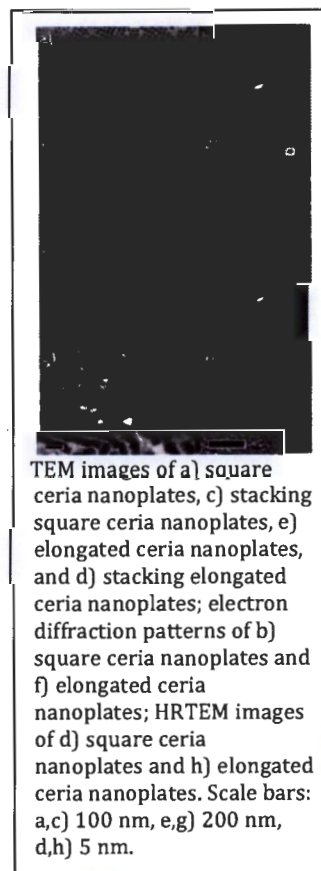
global and local ordering of these superstructures is programmed by the precise engineering of individual NC's size and shape. This dramatically improved nanophosphor synthesis together with insights from shape-directed assembly will advance the investigation of an array of emerging biological and energy-related nanophosphor applications.

### Synthesis and Oxygen Storage Capacity of Two-Dimensional Ceria Nanocrystals

Dianyuan Wang, Yijin Kang, Vicky Doan-Nguyen, Jun Chen, Rainer Küngas, Noah L. Wieder, Kevin Bakmutsky, Raymond J. Gorte, and Christopher B. Murray

*Angew. Chem. Int. Ed.* **2011**, 50, 4378-4381

Ceria has been widely used in catalysis, optics, sensors, and solid oxide fuel cells. Due to its high oxygen storage capacity (OSC), which originates from easy conversion between  $\text{CeO}_2$  and  $\text{CeO}_{2-x}$ , ceria has found its primary utilization in catalysis as an oxygen carrier. Ceria nanomaterials with various morphologies, mainly polyhedra, have been reported. Recently, 1D ceria nanostructures, such as nanowires, have also been reported. However, with the exception of one report on the preparation of nanosheets, well-controlled 2D ceria nanomaterials have not been explored and the comparison of the OSC properties between 3D and 2D structures has not been possible. On the other hand, the different properties of the (100), (110), and (111) ceria facets has been debated. There is no consensus on whether crystallographic orientation or particle size affects reactivities. Therefore, high-quality ceria nanocrystals selectively exposing different low Miller-index surfaces, are crucial to enabling experiments that resolve the controversy. Here we report a simple, robust solution-phase synthesis of





ultrathin ceria nanoplates in the presence of mineralizers. The morphology of nanoplates can be easily controlled by changing reaction parameters, such as precursor ratio, reaction time, etc. In addition, we also prepare ceria nanomaterials in various 3D morphologies by hydrothermal and combustion methods. The OSC of our 2D ceria materials have been tested and compared to the OSC of their 3D counterparts.

## Functionalization and attachment of NP (NP-2). Colin Nuckolls

The Nuckolls group has focused its efforts on designing, synthesizing, and studying molecules that could be used as molecular wires to link particles to each other and to link particles to surfaces such as GaAs and InGaAs. For these studies we have collaborated with the Murray group for the  $\text{Fe}_2\text{O}_3$  particles and for the attachment to GaAs and InGaAs we have collaborated with Christopher Murray.

We have developed a new type of molecular wire that is completely tunable and bears functional groups that allows them to assemble on surfaces. These molecular wires are noteworthy because they are molecularly defined, atomically precise fragments of polyacetylene (PA, Figure 1a). PA is remarkable because it is a simple hydrocarbon polymer that is highly conductive when doped.<sup>1</sup> It also has a low band gap and shows large nonlinear optical susceptibilities.<sup>2</sup> The hypothesis that we followed in the MURI studies was that since the fully conjugated high polymer is electrically conductive, then the well-defined oligomers, hereafter referred to as oligoenes, should be useful molecular conductors in nanoscale situations. These oligoenes are good choices because they are related to naturally occurring molecules, such as carotenoids, that have been made into electrical devices and are known to have useful optical properties. It is difficult to tune these molecules because of the limited number of structures nature provides.<sup>3</sup>

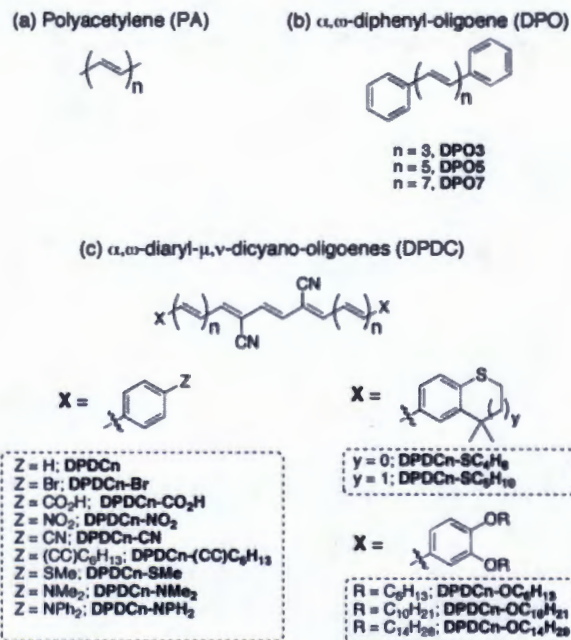


Figure 1. Structure of (a) Polyacetylene (PA). (b) Structure of  $\alpha,\omega$ -diphenyl-oligoenes (DPO), which are regarded as control molecules for comparison with DPDCs. (c) Structure of cyano-functionalized oligoenes, DPDCs. Oligoene molecules



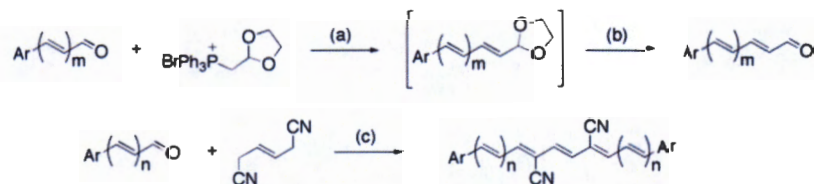
are identified according to their aryl end-group (**X**), and length of their linear conjugated backbone (**n**); **DPDCn-X**. For instance, 1,10-di-(4-bromophenyl)-4,7-dicyano-deca-1,3,5,7,9-pentaene is referred to as **DPDC5-Br**.

Three major challenges have hampered the development of oligoenes as electronic materials: (1) The most thoroughly studied examples of PA oligomers have been prepared by the painstaking isolation of individual oligomers from polymerization reactions that have been carried out only at low monomer conversion.<sup>4</sup> (2) Previous preparative methods have not supported functionalization, and therefore the incorporation of the oligoenes into electronic devices, such as the ones proposed in the MURI program, is limited. (3) Oligomers of PA are chemically impractical because they are nearly insoluble and oxidatively unstable. For the MURI program we developed a new synthetic strategy detailed below for the  $\alpha,\omega$ -diphenyl- $\mu,\nu$ -dicyanooligoenes<sup>5</sup> (DPDC), and are pleased to report that we have overcome these challenges. The key to this synthesis is the incorporation of sterically innocent yet electronically stabilizing nitrile side-groups along the oligoene chain and by terminating the chain with phenyl groups. Phenyl groups protect the reactive terminal olefins<sup>6</sup> and can be easily installed with a large diversity of functional groups.<sup>7</sup> These studies highlight the versatility and adaptability of these new electronic materials by using self-assembled monolayers of appropriately functionalized oligo-enes as electrical conduits that structurally connect magnetic nanoparticles to a semiconductor surface. This will be crucial for the MURI program going forward.

There have been several methods used in the literature to stabilize oligoenes. Some protect the highly reactive terminal olefins with bulky end-groups such as phenyl<sup>6</sup> or *tert*-butyl.<sup>8,9</sup> Other than such hydrocarbon-end-capped oligoenes, however, there are few other examples of non-carotenoid  $\alpha,\omega$ -disubstituted oligoenes longer than pentaenes.<sup>10,11</sup> We felt that for the MURI program these would be highly desirable because as is shown below it is the longer oligomers that have the smallest band gaps. In nature there are methods of oligoene stabilization: carotenoids are the most well-studied oligoenes since they play essential roles in vision (retinol), cell division (retinal) and photosynthesis.<sup>12</sup> In these molecules methyl groups decorate the oligoene backbone and make them both more soluble and more stable. However, the methyl groups collide with the allylic hydrogens on the backbone and distort the backbone from planarity, thus widening the energy difference between the highest occupied molecular orbital (HOMO) and lowest unoccupied molecular orbital (LUMO). Since we want small band gaps for the MURI project, we sought small and synthetically available substituents that could nevertheless confer stability. Cyano groups fulfill these requirements: they are sterically unintrusive,  $\pi$ -electron withdrawing groups (EWG) and not bulky enough to disrupt molecular planarity.<sup>13</sup> Since they are strongly electron withdrawing<sup>14</sup> they should lower the energies of the frontier ( $\pi$ ) orbitals and therefore reduce the likelihood of oligoene oxidation. As an ultimate benefit they enable an economical synthesis that allows for easy end-group functionalization.

**Synthesis.** The nexus of our synthesis of the oligoenes is the Knoevenagel condensation<sup>15</sup> between 1,4-dicyano-2-butene and two equivalents of the

appropriate aryl-enal (Scheme 1). We prepare the aryl-enals starting from the analogous benzaldehyde or trans-cinnamaldehyde via iterative Wittig homologations<sup>16</sup> and concomitant acid hydrolysis of the intermediate acetal. Both the Knoevenagel and Wittig reactions tolerate a wide variety of functionality that can furnish a range of derivatives. We show in Figure 1 those derivatives that we have already prepared.



In order to verify the practical value of the cyano substitution, we have also prepared the corresponding oligoenes that lack the cyano groups. They were synthesized by Horner-Wadsworth-Emmons reaction<sup>17</sup> as described by Spangler and coworkers.<sup>10</sup> The dicyano-oligoenes are sufficiently less reactive than their unsubstituted relatives such that we can conveniently study them under normal aerobic laboratory conditions for extended periods.<sup>18</sup> The thermal stability of these dicyano-oligoenes is similar to that of the tetrakis-*t*-butyl-functionalized oligoenes reported by Jones and coworkers<sup>9</sup> and far higher than that of the methyl and unfunctionalized analogs.<sup>19</sup> Differential scanning calorimetry shows that all members of the parent series **DPDC3-DPDC13** are thermally stable up to 250° C under an inert atmosphere. For a direct comparison we photo-oxidatively decomposed both **DPO5** and **DPDC5** in a side-by-side experiment; the unsubstituted material decomposed four times faster than the dicyano material.<sup>20</sup>

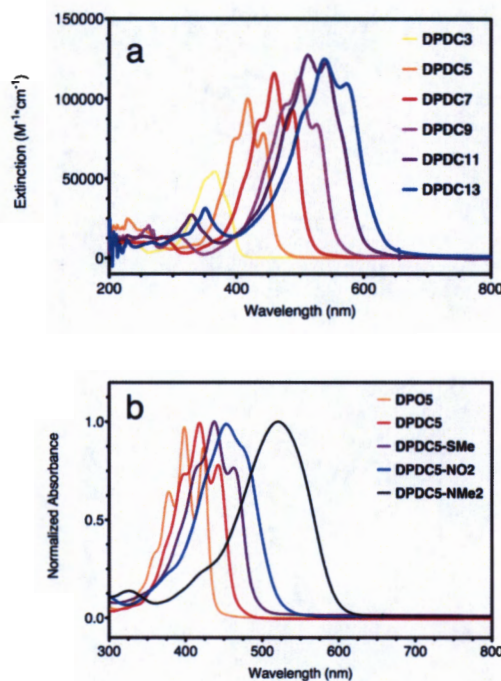


Figure 2. (a) UV-vis absorption spectra of the parent oligoene series (**DPDC3-DPDC13**) in CH<sub>2</sub>Cl<sub>2</sub>. Plot of extinction vs. absorption wavelength.  $\lambda_{\text{max}}$  (from left to right) at 363, 418, 459, 499, 513, and 536 nm; increasing the length of oligomers tunes the optical absorptions over a range of 350 nm. (b) UV-vis absorption spectra of oligoene derivatives in CH<sub>2</sub>Cl<sub>2</sub>; **DPO5** (orange), **DPDC5** (red), **DPDC5-SMe** (purple), **DPDC5-NO<sub>2</sub>** (blue) and **DPDC5-NMe<sub>2</sub>** (black). Absorptions have been normalized.

**Band-gap Engineering.** Despite providing stabilization to the oligoene core, the cyano- and phenyl-substitution does not fundamentally alter the "polyacetylene-type" electronic behavior of the oligoenes. For example, the color of these molecules is strongly correlated with the oligomer length. This has been seen in other vinylogous series<sup>21</sup> and indicates that the HOMO-LUMO gap closes as the conjugation "box" extends. The optical absorptions of the DPDCs span the entire visible spectrum (Figure 2a). The absorptions are also quite intense; molar extinction coefficients ( $\epsilon$ ) exceed 10<sup>5</sup> M<sup>-1</sup>cm<sup>-1</sup>. We estimate the solution-phase optical band gap ( $E_{\text{og}}$ ) for **DPDC11** and **DPDC13** to be 1.81 eV and 1.77 eV, respectively, approaching the values measured for PA itself. Similarly, the quantum mechanical particle-in-a-box model is often used to describe optical absorptions in the simplest size-dependent systems. This model holds that the excitation energies in a simple system vary as the inverse square of the dimensional length. We can fit the excitation energies in the DPDC series with such an inverse-square expression (see Figure 3a), and this leads to an effective mass of 6.22x10<sup>-48</sup> kg. Extrapolation of the strongest wavelength ( $\lambda_{\text{max}}$ ) and longest wavelength ( $E_{\text{og}}$ ) absorptions to an



infinite "box" length estimates values of 577 nm and 1.59 eV, respectively, for trans-PA. This is within the reported range of band gaps (1.4-1.8 eV) for PA.<sup>1,22</sup>

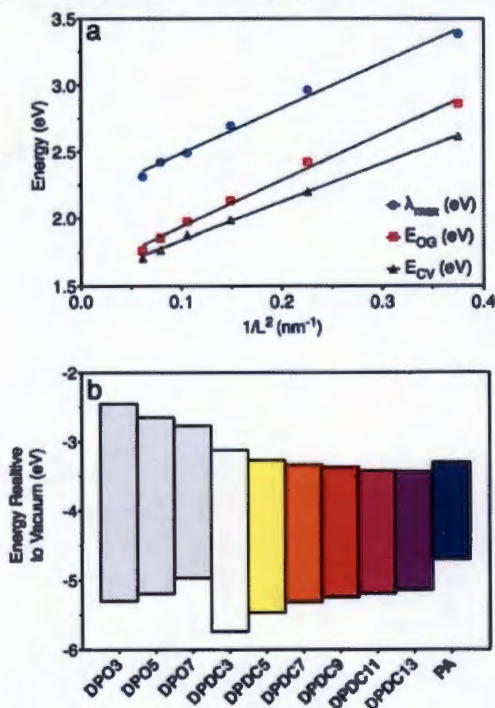




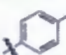



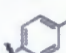


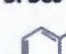
Figure 3. (a) Particle in a box models the characteristic energies determined for the DPDC's and estimates values for an oligomer of infinite length.  $\lambda_{max}$ , optical band gap ( $E_{og}$ ) and the redox band gap ( $E_{cv}$ ) of **DPDC3-DPDC13**, predict values of 577 nm, 1.59 eV and 1.59 eV, respectively, all of which agree well with experimentally determined values for PA. (b) Effect of the cyano groups on the HOMO and LUMO Energies of oligoenes determined by cyclic voltammetry (CV). Redox gap of **DPO3**, **DPO5**, **DPO7** (grey) and the parent series, **DPDC3-DPDC13**. CV's were obtained in DMF solution with 0.1 M (n-Bu)<sub>4</sub>N<sup>+</sup>PF<sub>6</sub><sup>-</sup>. Experimentally determined values for polyacetylene (PA) are included for reference.<sup>22</sup>

While the cyano groups do not change the fundamental electronic behavior of the oligoenes, they do change the particular characteristic values such as redox potentials and absorption maxima. As mentioned above, cyano groups are strongly electron withdrawing, and therefore lower the energies of the frontier orbitals. We used cyclic voltammetry to estimate the energies of the HOMOs and LUMOs in the DPDC series; we found that the nitriles stabilize the HOMO and LUMO by as much as 0.44 and 0.68 eV with respect to the corresponding unsubstituted of DPO molecules (Figure 3b). This is confirmed by UV-vis absorption spectroscopy, in which we observe a bathochromatic shift of up to 35 nm. From the redox values  $E_{cv}$  for an oligomer of infinite length is predicted to be 1.55 eV; both the  $E_{cv}$  and the  $E_{og}$  converge on to similar values as shown in Figure 3a. We also note that the number of electrochemically available states increases with molecular (conjugation) length. For



example **DPDC11** shows four quasi-reversible reductions. As a general trend, reductions become more reversible as the molecular length increases, while oxidations become less so, where apparent deposition of the oxidized material is observed on the electrode surface.

**Table 1. Comparison of Selected DPDC5 Derivatives and Their UV-vis Strongest-wavelength Absorptions.**

entry	R group	$\lambda_{\text{max}}$ (nm/eV) <sup>a</sup>	entry	R group	$\lambda_{\text{max}}$ (nm/eV) <sup>a</sup>
1		418/2.97	6		454/2.73
	<b>DPDC5</b>			<b>DPDC5-OC<sub>6</sub>H<sub>13</sub></b>	
2		426/2.91	7		453/2.74
	<b>DPDC5-Br</b>			<b>DPDC5-OC<sub>10</sub>H<sub>21</sub></b>	
3		426 <sup>b</sup> /2.91	8		455/2.73
	<b>DPDC5-CO<sub>2</sub>H</b>			<b>DPDC5-OC<sub>14</sub>H<sub>29</sub></b>	
4		449/2.76	9		453/2.74
	<b>DPDC5-NO<sub>2</sub></b>			<b>DPDC5-SMe</b>	
5		523/2.37	10		485/2.67
	<b>DPDC5-NMe<sub>2</sub></b>			<b>DPDC5-SC<sub>6</sub>H<sub>10</sub></b>	

<sup>a</sup>Strongest wavelength absorption is taken at the global  $\lambda_{\text{max}}$  and is not indicative of HOMO-LUMO gap energies,  $E_{\text{og}}$ .

Substitution on the terminal phenyl groups offers another opportunity to tailor the electrical and chemical properties of the oligoenes. We synthesized a series of derivatives (see Table 1) whose phenyl-substituents varied from strongly electron withdrawing ( $\text{NO}_2$ ) to electron donating ( $\text{NMe}_2$ ). We found *para*-substitution to be most effective since it is more strongly resonance-coupled to the oligoene backbone and at the same time sterically remote. Spangler and coworkers reported similar results in non-cyano DPOs having the *para*-substituents  $\text{NO}_2$ ,  $\text{Cl}$ ,  $\text{SMe}$ ,  $\text{OMe}$ , and  $\text{NMe}_2$ .<sup>18</sup> An example of the effect of phenyl-functionalization on optical absorption is displayed in Figure 2b. Strong electron donating groups give the greatest bathochromatic shifts. For example, when we substitute a **DPDC5**-scaffold with *p*- $\text{NMe}_2$  groups the longest-wavelength absorption shifts from 490 nm to 640 nm. We can access practically any energy within the visible region by pairing the appropriate oligoene length with the appropriate aryl end-group.

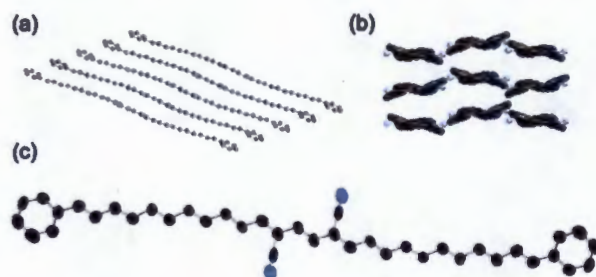


Figure 4. Packing structure of **DPDC13** (a) viewed from the side and (b) down the length of oligoene chain shows deviations from planarity. (c) ORTEP plot of **DPDC13**. Ellipsoids represent 90% probability levels. Hydrogen atoms have been omitted.

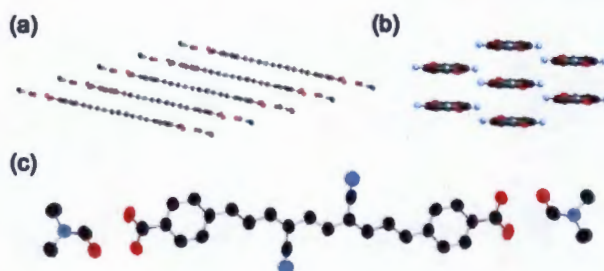


Figure 5. Packing structure of **DPDC5-CO<sub>2</sub>H•2DMF** (a) viewed from the side and (b) down the length of oligoene chain. (c) Ellipsoids represent 90% probability levels. Hydrogen atoms have been omitted.

**Solid-State Structure.** We have been able to grow crystals of each of the **DPDC<sub>n</sub>** consisting of 3 to 13 conjugated C=C. They are composed exclusively of *trans*-olefins as determined from the crystal structures. The crystal structure of **DPDC13** (Figure 4) is the longest oligoene characterized by XRD, even surpassing that of the natural product, rhodopin glucoside,<sup>23</sup> which contains 11 conjugated C=C bonds. Although, some of the shorter vinylogues have been previously prepared in the patent literature for resin dyes,<sup>24</sup> a systematic characterization has been unavailable heretofore. Previously only a few non-carotenoid structures having six conjugated C=C bonds have been reported, and none having more than nine.<sup>25</sup>

Different packing structures are observed within the series of DPDC oligomers. The shortest vinylogues, **DPDC3** and **DPDC5**, stack in a herringbone pattern and are planar, indicating that the nitriles do not significantly interact with allylic hydrogens. The longer oligomers, **DPDC7-DPDC13**, co-crystallize with one solvent molecule per unit cell. Density functional theory (DFT) calculations at the B3LYP/6-31G\*\* level predict fully planar conformations. However, the incorporation of solvent as well as bending is common in crystal structures of oligoenes of significant length (more than 6 C=C bonds).<sup>8,9,14</sup> Despite bending, the central olefin (that having doubly allylic nitriles) remains planar. This suggests that deviations from planarity are induced by the incorporation of solvent into the crystal lattice.



When DPDC's are functionalized with carboxylic acids the solid-state organization changes. The crystals have two molecules of solvent, dimethylformamide (DMF), included per oligoene. Figure 5 shows that the carboxylic acids, through hydrogen bonds, guide the assembly into  $\pi$ -stacked sheets of oligoenes. Unlike members of the parent series, **DPDC5-CO<sub>2</sub>H** is planar and oriented by hydrogen bonding interactions at each of its ends. The lack of solvent between oligoenes allows for the intermolecular distances to decrease to 3.38 Å between  $\pi$ -faces of neighboring molecules. These values approach the interplanar distances found for the classic carbon allotrope, graphite, of 3.33 Å.<sup>26</sup> **DPDC5-CO<sub>2</sub>H** stacks in an oblique alignment with six close neighbors oriented in a hexagonal pattern when viewed down the length of the molecule.<sup>27</sup> All molecules in the crystal lattice are aligned in the same direction and yet overlap the neighboring molecules through  $\pi$ -stacking interactions. This is an ideal geometry for assembly on surfaces into a two dimensional array.

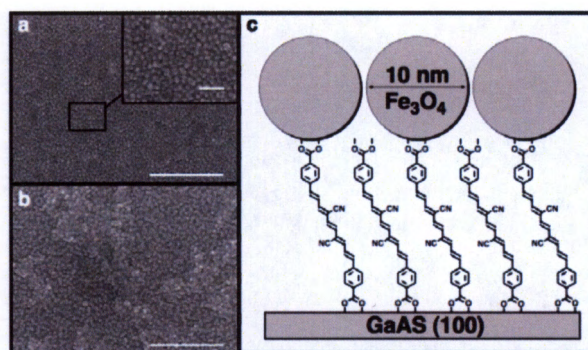


Figure 6. Scanning electron micrographs (SEM) of 10-nm Fe<sub>3</sub>O<sub>4</sub> nanoparticle SAMs made using (a) 1.5 mM solution and (b) 3.0 mM solution of oligoene, **DPDC3-CO<sub>2</sub>H**. Scale bars are set to 500 nm. Insert scale bar set to 50 nm. (c) Schematic of **oligoene-Fe<sub>3</sub>O<sub>4</sub>** composite monolayer.

**Self-Assembly.** For the MURI program one of the most important aspects will be assembly on semiconductor surfaces such as GaAs and InGaAs surfaces. We functionalized them to assemble SAMs of magnetic nanoparticles on GaAs substrates. The magnetic particles were obtained through a collaboration with the Murray group. It has been previously shown that carboxylic acids bind to GaAs and Fe<sub>3</sub>O<sub>4</sub> through known ligand exchange procedures.<sup>28</sup> First, the native oxide layer of the GaAs substrates were removed through submersion in aqueous ammonium hydroxide (NH<sub>4</sub>OH). After rinsing with ethanol they were submerged in a solution of oligoene **DPDC3-CO<sub>2</sub>H** in dimethyl sulfoxide (DMSO). They were then removed from solution, again rinsed with ethanol, and submerged for 1 hour in a solution of 10-nm Fe<sub>2</sub>O<sub>4</sub> nanoparticles in DMF. Scanning electron microscopy (SEM) analysis of these films shows clear formation of nanoparticle monolayers. Shown in Figure 6, we observed that nanoparticle coverage was dependent upon the concentration (1.5 mM, 3.0 mM, or 6.0 mM) of the oligoene solution. As a control, no monolayer



formation was observed when only DMSO was used or upon direct submersion of the GaAs substrate into the nanoparticle solution. Our next steps are to obtain InGaAs substrates from Kiehl to begin to study the dependence of transport on the magnetic field.

In addition to these studies on self-assembly we have also measured the single molecule conductivity of these oligomers. There are some interesting features to these studies that will be the focus of some future studies within the MURI.

## References and Notes:

1. (a) C. K. Chiang, M. A. Druy, S. C. Gau; A. J. Heeger; E. J. Louis, A. G. MacDiarmid; Y. W. Park; H. Shiraka. "Synthesis of highly conducting films of derivatives of polyacetylene, (CH) $x$ " J. Am. Chem. Soc. Vol. 100, pp. 1013-1015, 1978. (b) Park, Y. W.; Heeger, A. J.; Druy, M. A.; MacDiarmid, A. G. "Electrical transport in doped polyacetylene" J. Chem. Phys. Vol. 73, pp. 946-957, 1980.
2. (a) Kajzar, F.; Etemad, S.; Baker, G. L.; Messier, J., "[Frequency dependence of the large, electronic  \$\chi^{\(3\)}\$  in polyacetylene](#)", Solid State Comm. Vol. 63, pp. 1113-1117, 1987. (b) Fann, W. S.; Benson, S.; Madey, J. M. J.; Etemad, S.; Baker, G. L.; Kajzar, F., "Spectrum of  $\chi^{(3)}(-3\omega; \omega, \omega, \omega)$  in polyacetylene: An application of free-electron laser in nonlinear optical spectroscopy", Phys. Rev. Lett., Vol. 62, pp. 1492-1495, 1989.
3. (a) Burch, R. R.; Dong, Y.; Fincher, C.; Goldfinger, M.; Rouviere, P. E. Synth. Metals. "Electrical properties of polyunsaturated natural products: field effect mobility of carotenoid polyenes" Vol. 146, pp. 43-46, 2004. (b) He, J.; Chen, F.; Li, J.; Sankey, O. F.; Terazono, Y.; Herrero, C.; Gust, D.; Moore, T. A.; Moore, A. L.; Lindsay, S. M. "Electronic Decay Constant of Carotenoid Polyenes from Single-Molecule Measurements", J. Am. Chem. Soc., Vol. 127, pp. 1384- 1385, 2005. (c) Visoly-Fisher, I.; Daie, K.; Terazono, Y.; Herrero, C.; Fungo, F.; Otero, L.; Durantini, E.; Silber, J. J.; Sereno, L.; Gust, D.; Moore, T. A.; Moore, A. L.; Lindsay, S. M., "Conductance of a biomolecular wire" PNAS, Vol. 103, 8686-8690, 2006.
4. (a) Knoll, K.; Krouse, K. A.; Schrock, R. R. J. Am. Chem. Soc., "Preparation and isolation of polyenes containing up to 15 double bonds", Vol. 110, pp. 4424-4425, 1988. (b) Knoll, K.; Schrock, R. R. J. Am. Chem. Soc., "Preparation of tert-butyl-capped polyenes containing up to 15 double bonds", Vol. 111, pp. 7989-8004, 1989. (c) Scriban, C.; Amagai, B. S.; Stemmler, E. A.; Christensen, R. L.; Schrock, R. R. J. Am. Chem. Soc. "Synthesis and Optical Spectroscopy of Oligo(1,6-heptadiynes) with a Single Basic Structure Prepared through Adamantylimido-Based Molybdenum Wittig and Metathesis Chemistry", Vol. 131, pp. 3441-13452, 2009.
5. Symbols represent central positions along the oligoene main chain.
6. R. Kuhn, Angew. Chem., "Ueber die Synthese hoeherer Polyene", Vol. 50, pp. 703 - 718, 1937.
7. Meisner, J. S.; Kamanetska, M.; Krikorian, M.; Steigerwald, M.; Venkataraman, L.; Nuckolls, C. Nano Lett. "A Single-Molecule Potentiometer", Vol. 11, pp. 1575, 2011.
8. Kiehl, A.; Eberhardt, A.; Müllen, K., Lieb. Ann. Chem, " $\alpha,\omega$ -Dialkyl-substituted polyenes by palladium-catalyzed coupling reactions of vinyltin compounds with vinyl halides", Vol. 1995, pp. 223-230, 1995.

9. Klein, D., Kiliçkiran, P., Mlynek, C., Hopf, H., Dix, I., Jones, P. G. *Chem. Euro. J.*, "A General Route to Fully Terminally *tert*-Butylated Linear Polyenes"—Vol. 16, pp. 10507-22, 2010.
10. (a) Spangler, C. W.; McCoy, R. K.; Dembek, A. A.; Sapochak, L. S.; Gates, B. D. *J. Chem. Soc., Perkin Trans. 1*, pp.151-154, 1989. (b) Spangler, C. W.; Liu, P. K.; Dembek, A. A.; Havelka, K., *J. Chem. Soc., Perkin Trans. 1*, "Preparation and oxidative doping of  $\alpha,\omega$ -dithienyl polyenes", pp. 799-802, 1991.
11. (a) Duhatuel, L.; Duhamel, P., *Tetrahedron*, "Terminally substituted linear conjugated polyenes: Precursors of molecular wires", Vol. 34, pp. 7399-7400, 1993. (b) Froehlich, W.; Dewey, H. J.; Deger, H.; Dick, B.; Klingensmith, K. A.; Puettmann, W.; Vogel, E.; Hohlneicher, G.; Michl, J. *J. Am. Chem. Soc.*, "Excited singlet states of "hairpin" polyenes", Vol. 105, pp. 6211-6220, 1983.
12. Frank, H. A.; Britton, G.; Young, A. J.; Young, A.; Cogdell, R. J. "The Photochemistry of Carotenoids". Springer-Verlag. New York, ISBN-13: 9780792359425, ISBN: 0792359429, 2000.
13. A-value of cyano groups has been determined to be 0.17 kcal/mol in contrast to that of a methyl group (1.14 Kcal/mol).
14. Cyano groups are known as strong electron-withdrawing groups as evidenced by their high Hammett substituent coefficient. See Hansch, C.; Leo, A.; Taft, R. W. *Chem. Rev.*, "A Survey of Hammett substituent constants and resonance and field parameters", Vol. 91, pp. 165-195, 1991.
15. Knoevenagel, E.; *Chem. Ber.* "Condensation von Malondiure mit Aromatiachen Aldehyden durch Ammoniak und Amine", Vol. 31, pp. 2596-2619, 1898.
16. (a) Wittig, G.; Schoellkopf, U. *Chem. Ber.*, "*Über Triphenyl-phosphin-methylene als olefinbildende Reagenzien (I. Mitteil*", Vol. 87, pp. 1318-1330, 1954. (b) Wittig, G.; Haag, W. *Chem. Ber.*, Vol. 88, pp. 1654-1666, 1955.
17. Wadsworth, W. S. *Org. React.*, "Synthetic Applications of Phosphorlyl-Stabilized Anions", Vol. 25, pp. 73, 1977.
18. Stability of **DPDC3-DPDC11** were observed by <sup>1</sup>H NMR and thin layer chromatography for the duration of 6 months at 0 °C. No degradation was observed while working with oligoenes under normal laboratory conditions for hours or overnight. **DPDC13** was observed to change color when left out on the benchtop for 6 months. <sup>1</sup>H NMR of **DPDC13** showed broadened peaks.
19. (a) Bohlmann, F; Mannhardt, H. J., *Chem. Ber.*, "Darstellung und Lichtabsorption von Dimethylpolyenen", Vol. 89, pp. 1307-1315, 1956. (b) Nayler, P.; Whiting, M. C., *J. Chem. Soc.*, "Researches on polyenes. Part III. The synthesis and light absorption of dimethylpolyenes", pp. 3037-3047, 1955. (c) Sondheimer, F.; Ben-Efraim, D. A.; Wolovsky, R., *J. Am. Chem. Soc.*, "Unsaturated Macrocyclic Compounds. XVII.<sup>1</sup> The Prototropic Rearrangement of Linear 1,5-Enynes to Conjugated Polyenes. The Synthesis of a Series of Vinylogs of Butadiene", Vol. 83, pp. 1675-1681, 1961; (d) Sondheimer, F.; Ben-Efraim, D. A.; Gaoni, Y., *J. Am. Chem. Soc.*, "Unsaturated Macrocyclic Compounds XVIII.<sup>1</sup> The Prototropic Rearrangement of Linear 1,5-Diynes to Conjugated Polyen-ynes" Vol. 83, 1682-1685, 1961.
20. The presence of oligoene starting materials was monitored by UV-vis spectroscopy.

21. Muellen, K.; Wegner, G. "Electronic materials: The Electronic Approach." Wiley-VHC, New York, 1998. ISBN: 3-527-29438-4.
22. The reported values cover a wide range owing to different methods of polymer and film preparation. See: (a) Fujimoto, H.; Kamiya, K; Tanaka, J. Synth. Metals., "Optical constants of polyacetylene", Vol. 10, pp. 367-375, 1985. (b) Starzewski, K. A. O.; Bayer, G. M. Angew. Chem. Int. Ed. "Polyacetylen in polyacrylnytril-matrix: novel soluble matrix polyacetylene by ylide-nickel catalysis", Vol. 30, pp. 961-962, 1991. (c) Krausz, F.; Lásztity, P. Bakos, J. S., Appl. Phys. B., "The influence of photoinduced structural distortions on interband absorption in polyacetylene", Vol. 45, pp. 21-25, 1988.
23. McDermott, G. Prince, S. M. Freer, A. A.; Hawthornthwaite-Lawless, A. M.; Papiz, M. Z.; Cogdell, R. J.; Isaacs, N. W., Nature, "Crystal structure of an integral membrane light-harvesting complex from photosynthetic bacteria", Vol. 374, pp. 517-521, 1994.
24. (A) Langkammerer, C. M. "Reaction products of 3-hexenedinitrile and certain aldehydes", US 2462407, 1949. (b) Kok, Johannes, G. J.; Van Moorselaar, R.; Noordermeer, A. "Dyeing of Synthetic Resins" Ger. Offen., DE 2230783, 1972.
25. Investigations in the Cambridge Structural Database (CSD) provide only two non-carotenoid oligoene structures containing 9 linear conjugated C=C double bonds ( $n = 9$ ). Both structures belong to the molecule [18]-annulene. See Gorter, S.; Rutten-Keulemans, E.; Krever, M.; Romers, C.; Cruickshank, D. W. J., Acta Cryst., "[18]-Annulene,  $C_{18}H_{18}$ , Structure, Disorder and Hückel's  $4n + 2$  Rule", Vol. B51, pp. 1036-1045. Other search results show: 6 structures for  $n = 8$ ; 10 for  $n = 7$ ; and 13 for  $n = 6$ . There is clearly a dearth of solid-state oligoene data.
26. Wyckoff, W. G. "Crystal Structures." John Wiley & Sons, New York, London, 1963. ISBN: 0-470-96860-5.
27. This is similar to the solid-state packing structure in PA.
28. Dong, A., Ye, X., Chen, J., Kang, Y., Gordon, T., Kikkawa, J. M., et al., J. Am. Chem. Soc., "A Generalized Ligand-Exchange Strategy Enabling Sequential Surface Functionalization of Colloidal Nanocrystals", Vol. 133, pp. 998-1006, 2011.



### DNA scaffolding of NP arrays. (DP-1) Nadrian C. Seeman

Before the beginning of the MURI, the Seeman laboratory pioneered the field of Structural DNA Nanotechnology. Following the introduction of the notion of the field (1982), the prominent achievements of that period began with the construction of objects, such as a DNA cube (1991), and a DNA truncated octahedron (1994). These objects were floppy, so the laboratory introduced robust motifs (e.g., DX) in 1995, which ultimately led to both self-assembled 2D motifs (1998) and nanomechanical devices (1999). In conjunction with the Kiehl laboratory, the Seeman laboratory was involved in organizing gold nanoparticles in 2D arrays from 2001 to 2006. The logical next steps involved extending 2D organization to 3D, first using DNA, and then adding nanoparticles. The section below will outline the successes in this area. A second direction of extension is to move from gold to iron oxide particles, which is being pursued with a clear level of success at this time, and which will also be described. We will also discuss briefly some studies with a trigonal protein named ModG, which contains a nanoparticle-binding peptide motif, but which we have not been able to get to bind nanoparticles as one would like.

The attempt to make 3D self-assembled DNA crystals began in 1999, following the initial success of 2D self-assembled DNA crystals. In addition to the obvious intellectual challenge, 3D is likely to prove useful to the MURI's objective, because the crystals that result are macroscopic, with dimensions up to half a millimeter in size. Even if 3D organization of nanoelectronic components is beyond the current ability of the field to exploit, the surfaces of the crystals provide the largest single-domain arrays of DNA yet obtained. Numerous motifs were tried unsuccessfully in the early years of this decade, but all of them led to crystals that diffracted to 10Å resolution or worse. Success has finally been obtained with the tensegrity triangle motif that was first demonstrated by the Mao laboratory. The image below shows both the DNA sequence of a crystal and the crystals themselves.

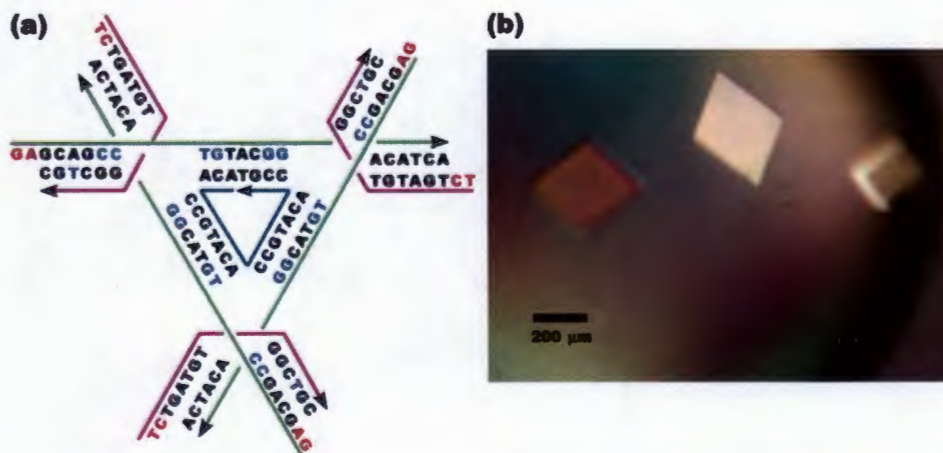
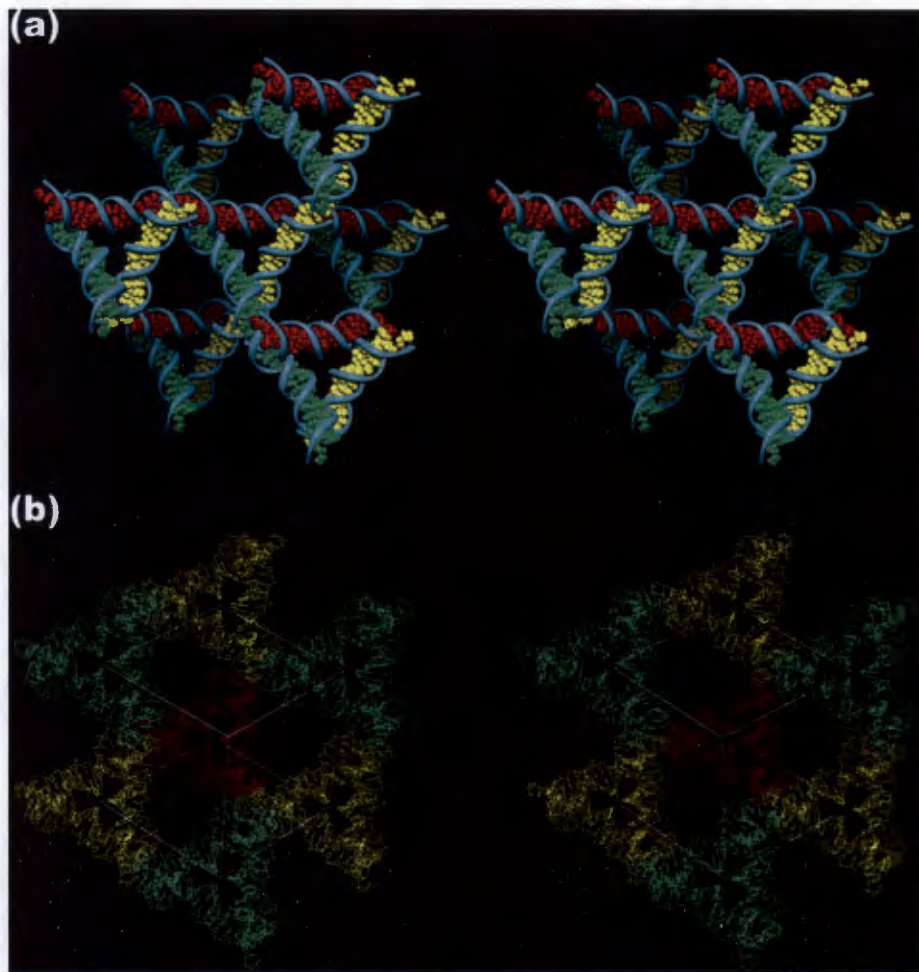


Figure 1. Design of 3D Crystals. (a) The Sequence and Structure. (b) Iodinated derivative crystals.

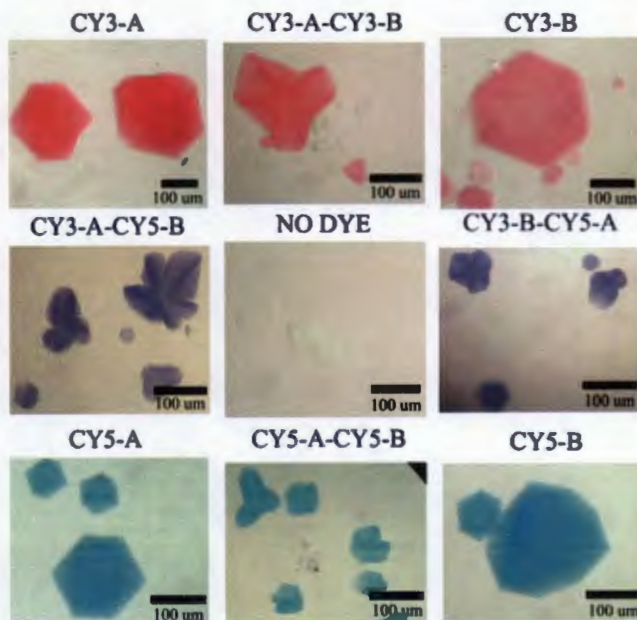
The motif itself spans 3-space, so it is straightforward to get the 3D crystals to self-assemble. When they do, each triangle is surrounded by six other tensegrity triangles. The crystal lattice is rhombohedral, each triangle sits on a vertex of a rhombohedron, creating a cavity with a volume of about  $100 \text{ nm}^3$ . The surroundings of an individual triangle and the rhombohedral cavity are shown in stereo in Figure 2.



**Figure 2. The Self-Assembled Crystal Structure of the Tensegrity Triangle. (a) The environment of an individual triangle. (b) The rhombohedral arrangement of tensegrity triangles. The red triangle flanking the rear vertex joins with the three yellow triangles closer to the viewer, and they each join with the three green triangles closer yet. The front vertex is flanked by another red triangle, which has been removed for clarity.**



We have also been able to use the sticky ends to put two different molecules in the asymmetric unit. By attaching dyes to these molecules selectively, we can color the crystals specifically. Thus, we attach a pink dye, Cy3, to one or the other or both of the individual molecules, and we get pink crystals. Similarly, we attach a blue dye, Cy5, to one molecule or the other or both, and we get blue crystals. When we attach the two dyes, in either order, we get purple crystals, as shown in Figure 3. This approach is clearly a way to prototype the attachment of two different particles to the constituents of the crystals.

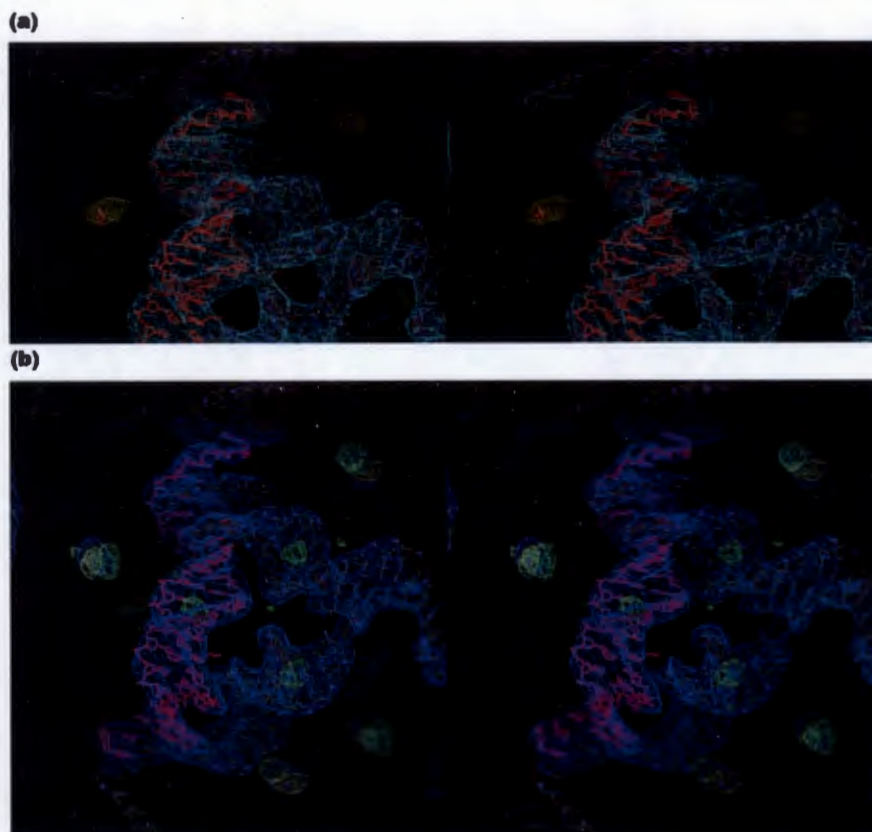


**Figure 3. Controlling the Color of Crystals by Adding Dyes to their Constituent Molecules.** In the top row, the pink dye, Cy3 is attached (left to right) to the A molecule, both, or the B molecule. Likewise in the bottom row, the blue dye, Cy5 has been attached in the same way. The middle row contains crystals where Cy3 is attached to one molecule and Cy5 to the other. The central panel contains control crystals to which dye has not been attached. This experiment is a prototype for the attachment of multiple particles within the crystals.

When it comes to attaching nanoparticles within the three-dimensional context, it seems most logical to begin with the gold particles with which we are most familiar. Of course, we have also begun with the tensegrity triangle crystals that we can self-assemble at will. As with the rest of 3D characterization, the most useful technique is X-ray diffraction analysis. We have worked with both Au-11, and with Au-55. The particles in both cases are attached covalently to the 5' end of the central strand (see Figure 1). The available tethers in both cases are fairly long, and the particles are consequently somewhat disordered. The most reliable way to visualize a metallic particles in the crystalline context is through 'anomalous' scattering. This phenomenon is related to partial absorption of the X-rays by the metal atoms, introducing a change in the imaginary component of the atomic scattering factor. It is observed when one collects data for both the positive hemisphere of reflections and the negative hemisphere, and compares them using an 'anomalous difference' Fourier summation. Figure 4 shows stereographic projections of Au-11 (panel a) and Au-55 (panel b). In the current crystals, we have 3-fold averaged images, because we obtain better crystals if we use the same sticky ends on all three edges of the tensegrity triangle. What is shown is the contoured anomalous scattering density of the gold particles along with the conventional density that is derived from



the DNA components of the crystals. There is a little density directly on the DNA in the anomalous scattering map of Au-55. This is an artifact caused by a certain amount of non-isomorphism between the crystal with the gold particle and the crystal lacking the gold particle. What is clear from both images in Figure 4 is that there is a large anomalously scattering particle that is sitting out in the major cavity of the crystal. Clearly it would be a good idea to eliminate the 3-fold averaging by using distinct sticky ends. These studies are in progress.

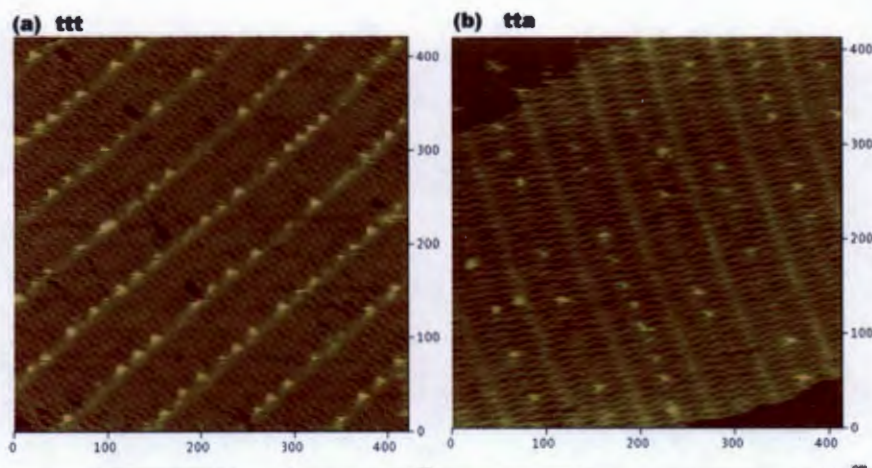


**Figure 4. Anomalous Scattering of Gold Nanoparticles in a Self-Assembled DNA Crystal.** (a) Au-11. The density corresponding to the nanoparticle is drawn in gold. (b) Au-55. The density corresponding to the nanoparticle is drawn in green and blue. In both constructs, the nanoparticles seem to be about as far from the DNA as their tethers will permit them to be.

In addition to gold, we have also worked with Iron oxide ( $\text{Fe}_3\text{O}_4$ ) particles, this time in two dimensions. We find that carboxyls on the DNA do not work. We have obtained the best performance from particles that are commercially available from Nanotech Ocean and that are coated with streptavidin. DNA is attached to them through a biotin-streptavidin linkage, where the biotin is on the DNA 5' end. We have used the original Pinto et al. construct of 4 DX tiles to organize the particles. This construct contains two potential sticky ends. One is on a DX tile containing a long hairpin that terminates in oligo dT. The other sticky end, on another DX tile, is

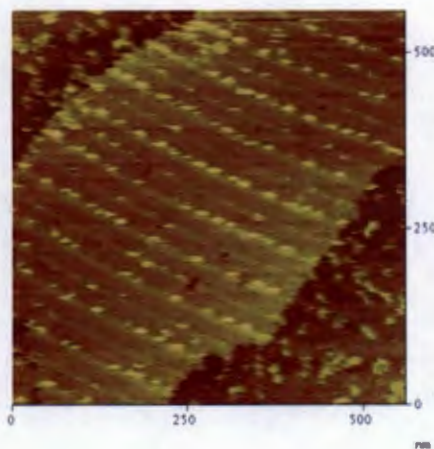


not associated with a hairpin, and the sequence is a repeat of tta. Thus, in AFM images, particles on the hairpin (TTT sticky ends) will appear directly on the stripes of the array, and those associated with the TTA sticky end will appear between the stripes of the array. An example of the best we have done to date is shown in Figures 5 and 6.



**Figure 5. Zoomed Images of 10 nm Iron Oxide Particles on a DX Array.** (a) These particles are bound to the hairpin by the ttt sequence. They sit on the stripes generated by the hairpin. Coverage is almost complete. (b) These particles are bound to the tta sequence. They are half-way between the stripes generated by the hairpin. Coverage is not nearly as good.

Direct comparison of the relative efficiencies between the two different types of attachment, to a sticky end on the hairpin or to a sticky end simply extruding from the array, is seen clearly in the double-binding experiment shown in Figure 6.

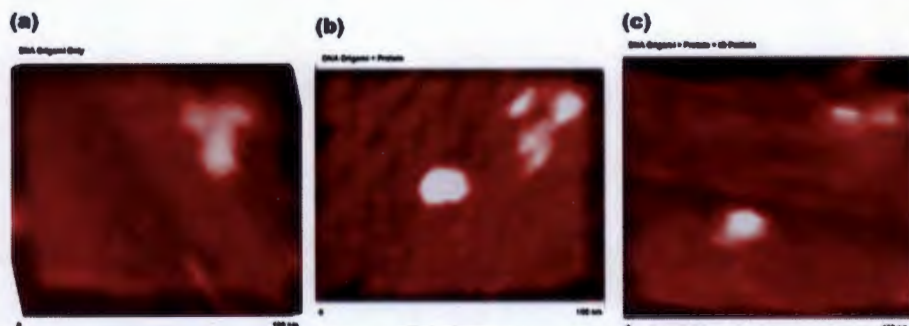


**Figure 6. Comparison of 10 nm Iron Oxide Particle Binding to an Isolated Sticky End in a DX Array and Binding to a Sticky End on a Hairpin.** It is clear that there are two alternating rows of particles bound. One of these rows, the one on the hairpins, is much more efficiently bound than the other row, where the sticky end simply emanates from the array. The control experiment of switching the two sequences, so ttt is between the rows and tta is on the hairpins, has not yet been performed. Four-tile arrays containing two different rows of stripes have been built previously.

We have tried to attach nanoparticles to the ModG protein (from Todd Yeates) that has been attached to a DNA origami construction. The protein contains a particle-binding peptide that should facilitate this binding. The protein is fairly successfully



attached to the DNA origami, but it does not seem possible to attach the nanoparticles to the protein while it is attached to the origami. Efforts continue to find ways

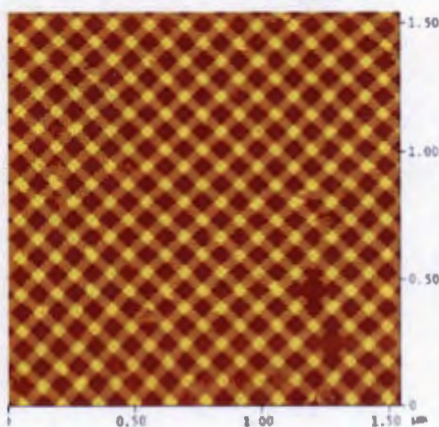


**Figure 7. Attempts to Add Iron Oxide Nanoparticles to ModG Protein.** (a) A DNA Origami Construct containing a marker in the shape of a T for a control reference sub-image. (b) The same origami to which the ModG protein has been added. The protein is readily visible at the enter of the origami construct. (c) Iron oxide nanoparticles have been added to the material in panel (b). Little, if any, change is

attach the particles to the protein.

An additional effort in which we have been engaged is to attempt to make the large arrays that the Mao group has reported. The extent to which the domains in these arrays are aligned has not been reported. To date we have been unsuccessful in generating such arrays, but consultation with Prof. Mao indicates that it is necessary to close the central circle of the domain in a covalent fashion. Efforts are underway to make this modification to the protocol and to continue in this direction.

To summarize some key points, the purpose of the NYU-Chemistry part of the MURI



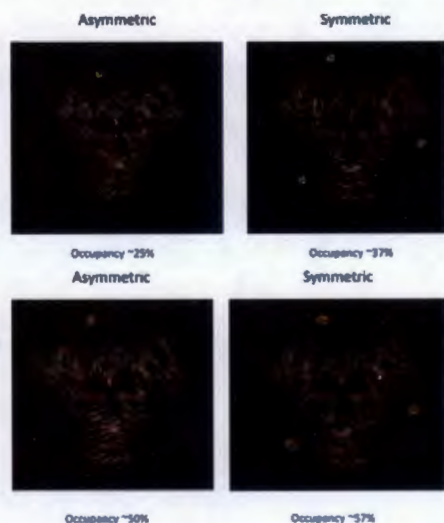
**Figure 2.** Taken from W. Liu, H. Zhong, R. Wang & N.C. Seeman, Crystalline Two-Dimensional DNA Origami Arrays, *Angew. Chemie* 50, 264-267 (2011).

was to work out ways of attaching various species to multidimensional DNA species, either 2D small DNA molecular arrays (e.g., DX) or 2D origami tiles or 2D origami tubes or 3D DNA crystals. Part of the work entailed learning how to organize DNA into origami arrays and DNA tensegrity crystals into 3D crystals that diffract adequately to be characterized. The species to be attached were globular proteins, and gold or iron-oxide nanoparticles.

Part of the control offered by structural DNA nanotechnology is the ability to put more than a single molecule in an asymmetric unit. We learned how to do this in 3D, which is shown in Figure 1. There are two different molecules (the red and the green) which alternate in the



rhombohedral motif. We were able to dye the crystals 3 different colors by attaching dyes to one molecule, the other or both. In a similar fashion, we also solved a major organizational problem by learning how to organize DNA origami



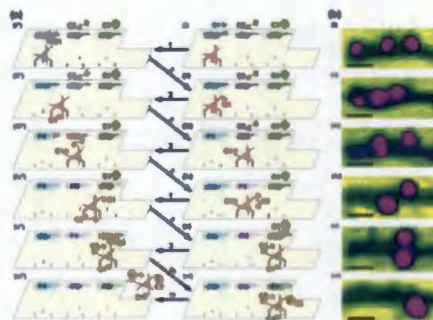
**Figure 3.** Anomalous difference densities for Au-11 (green) and Au-55 (orange).

up with this experimental advance, it is worth noting that the surfaces of the crystals (at least 100 x 100 nm) are the largest 2D arrays of nanoparticles yet to be developed.

We have also demonstrated the capability of manipulating gold nanoparticles individually in a proximity-based nanoscale assembly line. We are able to add different species of gold nanoparticles (a 5 nm particle, a 10 nm particle, and a pair of coupled 5 nm particles) to a somersaulting walker 'chassis' that is deliberately tumbled past each of the addition stations. The 3 different stations lead to  $2^3$  different products, all of which have been made and identified in the differently programmed trajectories. Figure 4

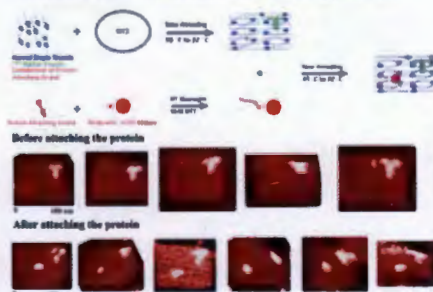
species into 2D crystals, rendering that system useful for larger organizational efforts. This crystal is shown in Figure 2. Note the scale.

Ours is the first group to organize nanoparticles in 3D. 3D organization of nanoparticles is a whole new paradigm in the DNA organization of metallic nanoparticles. We have done this in four systems, both Au-11 nanoparticles and Au-55 nanoparticles organized in the tensegrity triangle lattice, similar to the one in Figure 1, except that only a single species of DNA has been used in this case. Figure 3 illustrates these four different systems. A model of the tensegrity triangle is shown, flanked by anomalous difference densities. Au-11 is shown in the top panels and Au-55 is shown in the bottom panels. Although design has not caught



**Figure 4.** Taken from H. Gu, J. Chao, S.J. Xiao & N.C. Seeman, A Proximity-Based Programmable DNA Nanoscale Assembly Line, *Nature* **465**, 202-205 (2010).

#### Protocol to Put a Protein on a DNA Origami Tile

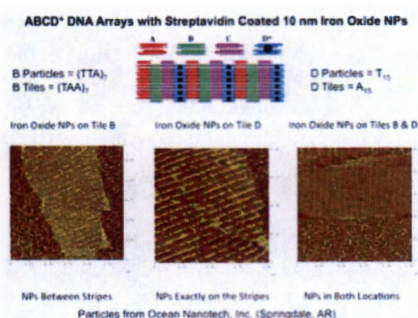


**Figure 5.** The protocol to put the protein on an origami tile is shown at the top. The bottom shows five AFM images before adding the protein to a specific location in the tile. A marker 'T' is in the upper right-hand corner of the tile as a marker. The bottom row shows images of adding the protein to a specific locus. The white dot at the lower left is clearly identifiable as the protein.

shows the system; the middle column shows in schematic what is observed by AFM in the right-most column.

An assigned task in this project was the attachment of a protein to a specific site in an origami tile. The ultimate aim here was to demonstrate that we could render a protein susceptible to the large architectural power of structural DNA nanotechnology. Although the trimeric protein itself was in the end shown by others to be incapable of binding the designated nanoparticles as particles, we were successful in binding the protein to the DNA origami tile. This is shown in Figure 5.

Another assigned task was to get iron-oxide nanoparticles to bind to the standard ABCD\* DX-DNA array. None of the nanoparticles produced within the MURI group



**Figure 6.** The Addition of Iron Oxide Nanoparticles to ABCD\*. The ABCD\* array was prepared with the particles destined for the B tiles bearing a (TTA)<sub>7</sub> and the B tiles bearing a (TAA)<sub>7</sub> complement. Likewise, particles destined for the D\* tiles were derivatized with T<sub>15</sub> and the D\* tiles with the hairpins also had a A<sub>15</sub> sequence. The left AFM panel shows particles only on the B-tiles, between the stripes. The middle panel shows particles attached to the D\*-generated stripes. The right panel shows particles in both locations, as both the B particles and the D\* were bound to particles, so there are particles visible both between the stripes and resting on them.

were capable of binding to this array, but a preparation purchased from Ocean Nanotech, Inc. (Springdale AR) were properly prepared, so that we could accomplish this goal.

Note that each of the slides in this summary narrative indicates a unique breakthrough in the manipulation and organization of nanoparticles.

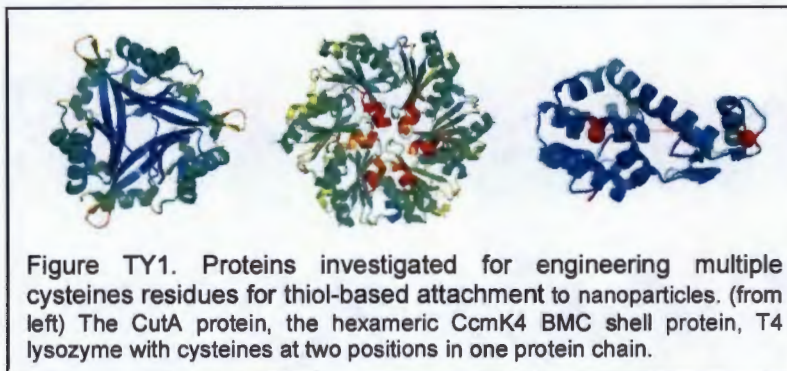


## Protein-organized dimer and trimer NP subcomponents (DP-2).

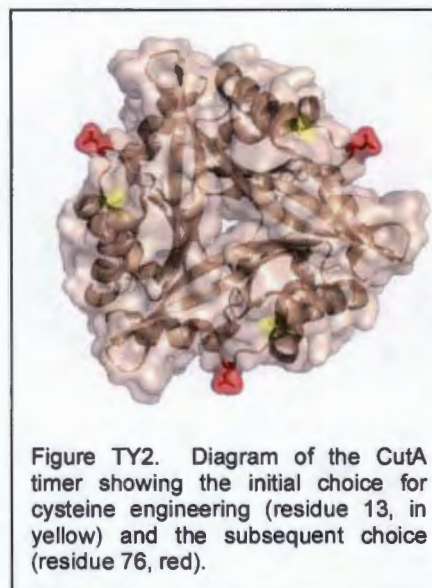
Todd O. Yeates

### Period I

During the period preceding the UCLA review, we performed cysteine engineering studies on several proteins (Fig. TY1). Towards the end of this period, we focused attention on one particular protein deemed most likely to be useful for creating a trimeric cluster of nanoparticles. This protein was CutA, a naturally trimeric protein with 102 amino acids per monomer, a known structure, and established extreme thermostability and tolerance for



organic solvents. The first amino acid position chosen for cysteines insertion was serine 13. This position was chosen based on visual inspection for its perimeter location (intended to provide for individual attachment to three different monofunctionalized nanoparticles, each expected to bear a single maleimide functional group), and its accessibility for chemical reaction. The protein was expressed and purified from *E. coli*. Biophysical experiments, including light scattering and size exclusion chromatography, were performed to confirm that the engineered protein folded correctly and associated into the native trimeric form. At that point, monofunctional nanoparticles were not available to test the ability of the engineered CutA to bind separately to three nanoparticles. Instead, a large organic polymer (PEG maleimide) was used to test whether the engineered cysteines would be chemically accessible for eventual nanoparticle attachment. Those reactivity experiments showed, unexpectedly, that making attachments to the designed site (residue 13) was problematic; only partial saturation could be achieved, as judged by native gel electrophoresis. Plans were made to reassess the site of attachment. A computational analysis of solvent accessibility was performed on the CutA trimer in order to make a more objective choice for cysteine



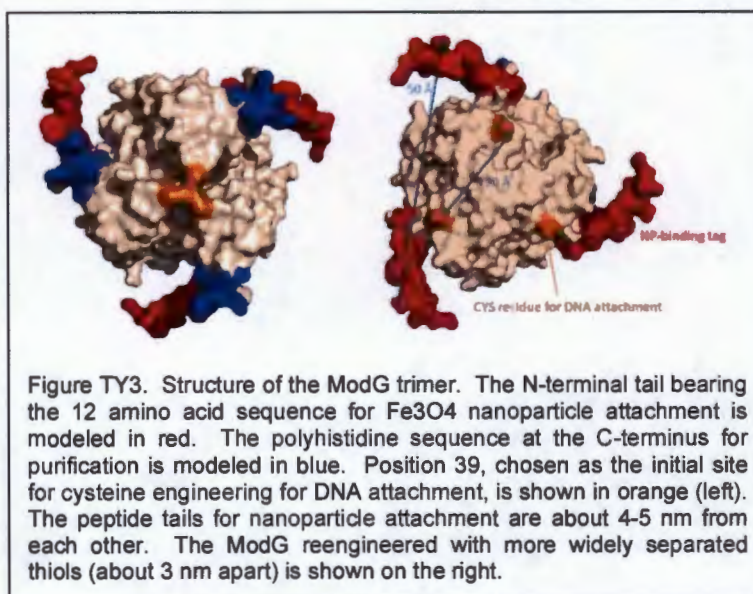


insertion. Position aspartate 76 was chosen for subsequent experiments (Fig. TY2), and molecular cloning was initiated. Development of the thiol-based nanoparticle attachment strategy was put on hold temporarily following progress reported by Prof. Huang at the UCLA review on obtaining peptide sequences for nanoparticle attachment.

## Period 2

At the time of the UCLA review, Prof. Huang presented new data showing the successful selection of short peptide sequences specific for binding to different types of nanoparticles. The possibility of using peptide sequences for nanoparticle binding was viewed as attractive as it might relieve the need for chemically monofunctionalized nanoparticles.

Our protein engineering efforts were therefore redirected towards designing a trimeric protein bearing extra tails based on the amino acid sequences discovered by Prof. Huang. This required a different protein as the framework, since one chain terminus would need to be situated at a desired position in the trimer (e.g. around the periphery). The protein chosen for this



line of experiments was ModG from *Azotobacter vinlandii*, a thermophilic protein with 144 amino acids per monomer (Fig. TY3). The N-terminus of that protein is situated at the periphery of the trimer. The following amino acid sequence for binding Fe<sub>3</sub>O<sub>4</sub> was engineered at the beginning of the ModG protein: mgssALESPHPRLLPssg (with the capital letters representing a 12 amino acid sequence obtained by Hu, and the lower case letters representing a flexible linker and cloning artifacts). This protein was purified and expressed in *E. coli*, and established by biophysical methods to be natively folded and trimeric as expected. The ultimate plan was to attach nanoparticles via peptide tails, and DNA via cysteine engineering and thiol chemistry. An initial idea was to try to engineer a single attachment point for DNA. To that end, a first site for inserting a cysteine was chosen near the three-fold symmetry axis in ModG, with the idea that oxidizing conditions would lead to formation of a single disulfide bond between two of the cysteines, leaving just one cysteine free for DNA attachment. It was subsequently



suggested that it would be advantageous to have three more widely spaced thiol attachment points, so an alternate site (residue 117) was then chosen and the ModG protein was reengineered.

Experiments were then conducted to test whether the ModG bearing peptide tails would bind nanoparticles. The engineered ModG protein was mixed with 10 nm Fe<sub>3</sub>O<sub>4</sub> particles. Electron microscopy studies were problematic. Despite the formulation of nanoparticles for improved solubility in aqueous solutions, irregular aggregates were often observed in EM images, even in the absence of added protein. This complicated analysis. However, under optimal condition, particularly dilute nanoparticle concentrations, it was possible to visualize trimeric clusters of ferrite nanoparticles, presumably organized by attachment to the ModG trimer (Fig. TY4). However, these represented only a minority of the population. Indeed, eletrophoresis studies on the ModG protein plus nanoparticles indicated relatively weak binding. The ModG plus Fe<sub>3</sub>O<sub>4</sub> nanoparticles experiment therefore represented a partial success, but prospects for obtaining fully trimerized ferrite nanoparticles in high yield appeared problematic.

We also engineered an alternate version of ModG in which the tail sequence was one determined by Prof. Huang to bind platinum nanoparticles. The terminal amino acid sequence in that case was FTLSSPY. The binding of this version of ModG to platinum nanoparticles was relatively strong based on native gel electrophoresis experiments. Owing to the lesser interest in platinum particles for the main project objectives, this line of work was not followed up.

One potential approach for achieving trimeric ferrite nanoparticles bound to a DNA template was laid out. When nanoparticles are added at high concentration to the trimerizing protein, the nanoparticles tend to aggregate. When the protein is present at high concentration, multiple proteins can attach to a single nanoparticle, thereby defeating attempts to obtain purely trimeric forms. But if the trimeric protein was attached first to DNA (either at one or many locations), then it might be possible to add nanoparticles at concentrations that would saturate the three binding sites on a protein trimer. Very preliminary experiments – involving just the attachment of protein trimer to DNA – were conducted along this line of investigation.

In view of the challenged faces with the peptide tail approach, and in the hopes that chemically monofunctionalized ferrite nanoparticles might eventually become

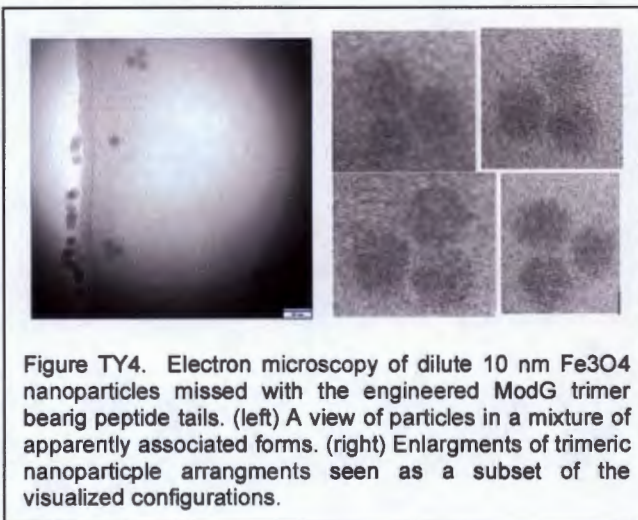
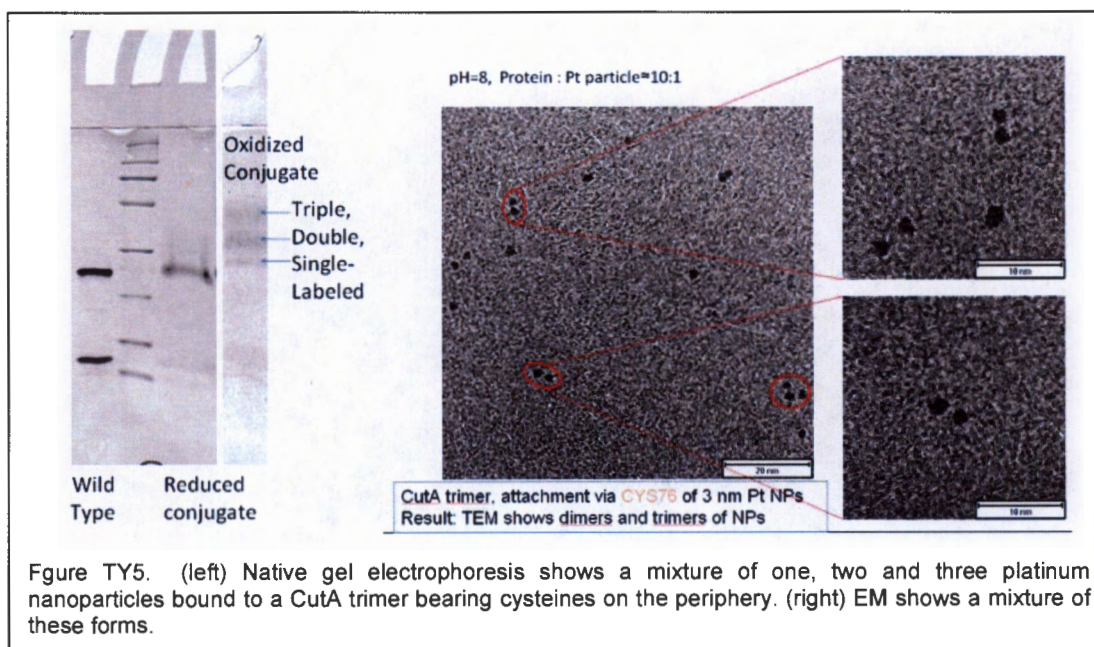


Figure TY4. Electron microscopy of dilute 10 nm Fe<sub>3</sub>O<sub>4</sub> nanoparticles mixed with the engineered ModG trimer bearing peptide tails. (left) A view of particles in a mixture of apparently associated forms. (right) Enlargements of trimeric nanoparticle arrangements seen as a subset of the visualized configurations.

available, we returned to the earlier protein system (CutA) for binding nanoparticles via thiol chemistry at the trimer periphery. In the absence of ferrite particles bearing single maleimide functional groups, we tested the ability of the CutA trimer



bearing peripheral cysteines (at residue 76) to bind directly to 3 nm platinum nanoparticles. Native gel electrophoresis showed the presence of a mixture of protein trimers bearing one, two, or three platinum nanoparticles (Fig. TY5). Electron microscopy likewise revealed a mixture of these forms. As before, the experiments demonstrated some ability to achieve binding between proteins and nanoparticles in solution, but serious difficulty in achieving full binding or high yields.



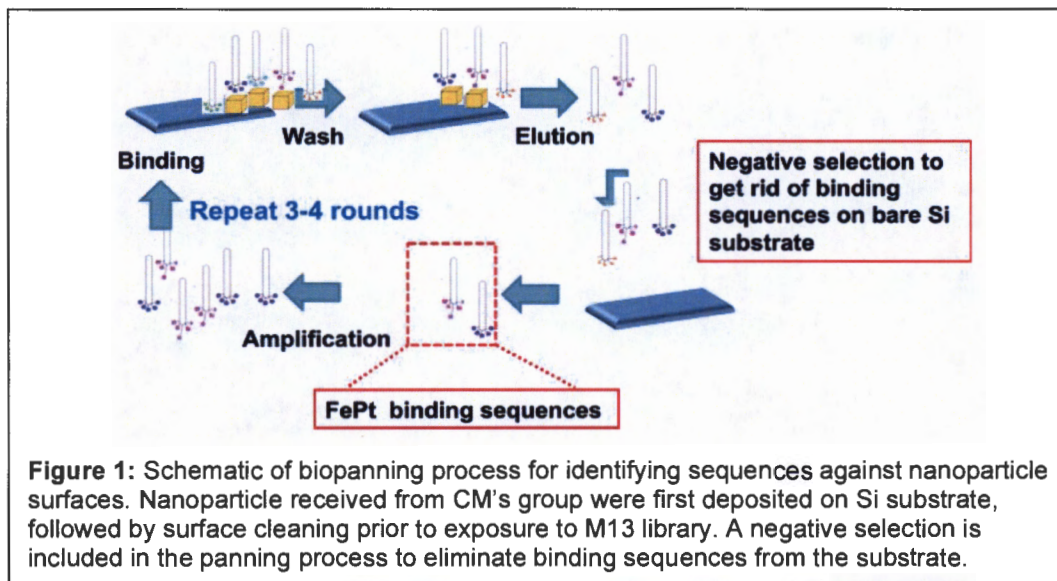
## Specific peptide affinities to core/shell NP (DP-3). Yu Huang

The ultimate objective of the project is to bio-assemble a practical quantum electronic system with built-in complexity and desired architecture. One of the main sub-objectives is to engineer highly active and selective recognition motifs using biomolecules, which will eventually enable the realization of such a self-assembled system.

Within this context, during the first two funding periods, our group has achieved identification of material specific peptide sequences that bind to FePt and Pt nanoparticles, as well as tested the binding specificity of the free peptides (out of its viral protein context) and their application in assisting in-situ synthesis of ultra-small metallic particles which may find their utilizations in quantum electronics. As a team effort, the identified sequences have been passed on to TY's group for incorporation into multimeric protein structures and demonstrated interesting trimer assembly of Pt nanoparticles on protein.

### Approaches

Phage display technique is used to select peptide sequences which have specific binding ability to FePt and Pt crystal surfaces (Figure 1). Fmoc solid phase peptide synthesis (SPPS) technique is used to synthesize the selected peptide sequences. And the effects of selected peptides on the attachment and growth of Pt NCs were explored with "green chemistry" that are comparable with biological systems, at room temperature in aqueous solution.



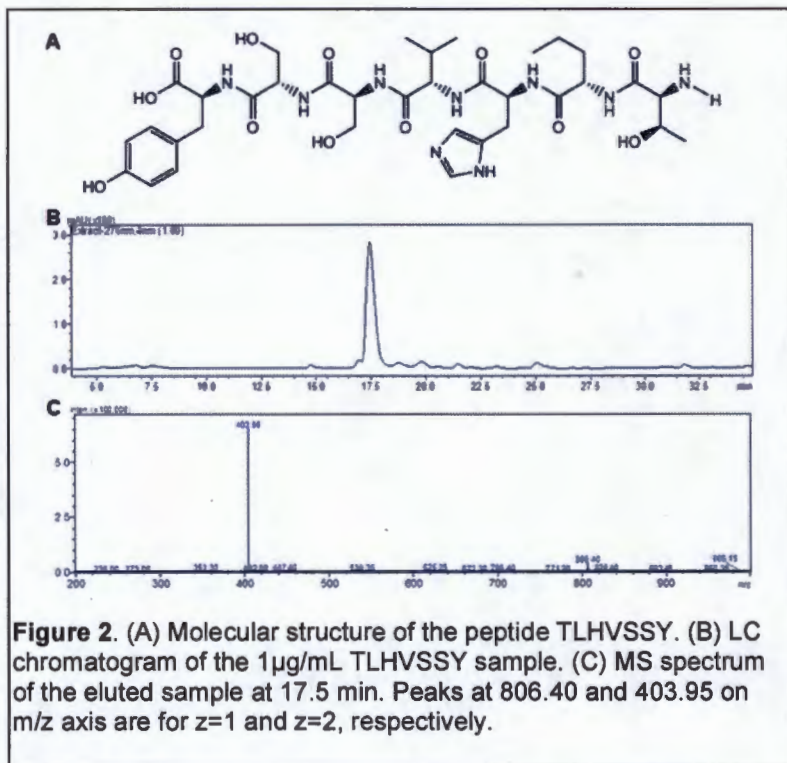
After we identify the peptide sequences that specifically bind to Pt surface, e.g. Thr-Leu-His-Val-Ser-Ser-Tyr (TLHVSSY, MW: 805.9) was selected from the M13 Ph.D.-7 peptide library (New England Biolabs) that bind to Pt surface. Free TLHVSSY moles were then synthesized with F-moc solid phase peptide synthesis (SPPS) technique, and purified with HPLC system to achieve high purity greater than 95% (Figure 2).

## Accomplishments

### 3a. Peptide sequences bound to Fe<sub>3</sub>O<sub>4</sub> and FePt surfaces

The Fe<sub>3</sub>O<sub>4</sub> sequences emerged from Ph.D 12mer library, 7mer library and c7c library (Figure 3), appear to be both rich in hydrophobic, proline and positive charged amino acids and poor in negative charged amino acids when compared to the original library. The selection of positive charged vs negative charged amino acids may be attributed to the

terminal crystal faces of the nanoparticles, e.g. O termination vs. Fe termination. KVMPQH D was identified against FePt nanoparticle sequences. Peptide



#### 12 mer

4 out of 19

8 out of 19

2 out of 19

2 out of 5

3 out of 5

Ala	Leu	Ala	Ser	Pro	Ile	Pro	Ala	Leu	Leu	Pro	Val
Gly	Leu	Asn	Pro	Phe	Ser	Ile	Leu	Pro	Leu	Val	Met
Asn	Pro	Val	Pro	Ser	Pro	Ser	Thr	Ser	Gly	Ser	Met
Leu	Ile	Gln	Pro	Thr	Ser	Ser	Ile	Ile	Met	Ser	Ala
Ala	Ser	Thr	Val	Gly	Ser	Cys	Leu	Ala	Leu	Ser	Ala

#### C7C

3 out of 10

4 out of 10

2 out of 10

E	R	H	S	W	K	S
N	S	N	G	L	S	H
Y	P	T	V	G	R	L

#### 7 mer

4 out of 10

3 out of 10

4 out of 4

K	P	S	V	N	V	H
E	R	P	Y	W	P	Y
N	P	A	N	P	L	I

(+) Charged Groups
(-) Charged Groups
Hydrophobic Groups
Hydrophilic Groups
Methionine
Ring Groups
Proline
Amide Groups

Figure 3. Results of Fe<sub>3</sub>O<sub>4</sub> peptide sequences identification using different M13 phage libraries.



sequences have been passed on to TY's group.

### 3b. Pt binding sequence, Pt Nanocrystal (NC) synthesis and assembly.

*Ultrasmall Pt NCs with tunable morphology and comparable size to the size of macro-biomolecule is important to the assembly of versatile electronic systems. As most small QDs or NCs are synthesized in organic solvents, the compatibility with biological system is rather limited. In this project, our goal is to devise a general approach to the synthesis and assembly of small sized NCs in Aqueous solution, which is compatible with biological entities. We have achieved so far.*

(1) Peptide sequence TLHVSSY has been identified and synthesized as specific binder to Pt surface.

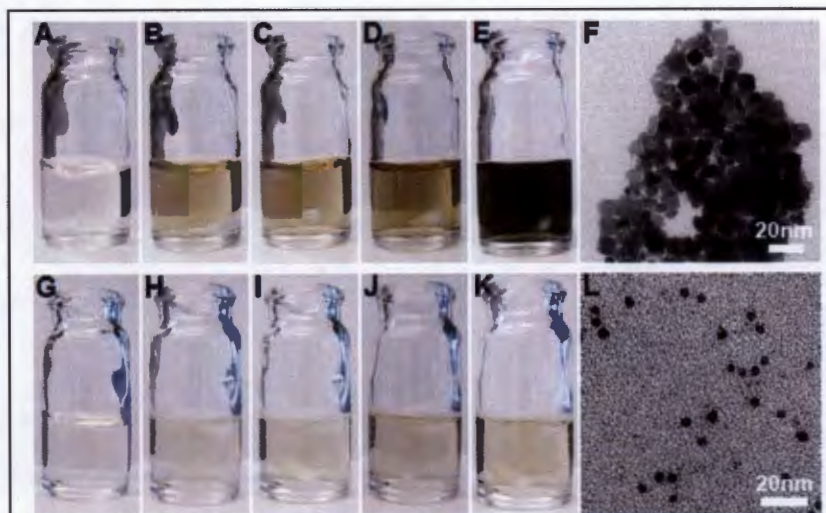
(2) We demonstrated that the synthesized free peptides can (A) retain the binding ability to Pt surface, and function as stabilizers to keep Pt NC stable in water; (B) affect on both the size and morphologies of Pt NC and suppress the growth in [111] direction of the Pt NCs.

(3) Protein-Pt NC trimer assembly has been achieved with the ultrasmall Pt NCs synthesized in aqueous solution, demonstrating the power and feasibility of a bio-assembled nanoparticle approach.

#### (A) Achieving Ultrasmall Pt NCs in Aqueous solution with specific peptides

is briefly described as below. A mixed aqueous solution of potassium tetrachloroplatinate (II) ( $K_2PtCl_4$ ) and TLHVSSY peptide was first prepared, into which a

fresh 40 mM sodium boron hydride ( $NaBH_4$ ) solution was injected in a single shot. The reaction was strongly stirred at room temperature until no color change can be observed. Droplets of reaction solution were pipetted out to prepare transmission electron microscope (TEM) samples on copper grids. Blank reactions without added peptides were also conducted as control experiments.



**Figure 4.** Color evolution of blank reaction (A)-(E) and 50  $\mu\text{g/mL}$  peptide reaction (G)-(K). (A), (G) are before  $NaBH_4$  addition. (B)-(E) and (H)-(K) are photos taken at 10s, 30s, 1min and 3min after reductant injection. TEM images of the obtained NCs from blank reaction at 10s (F) and 50  $\mu\text{g/mL}$  peptide reaction after 36 hours (L).

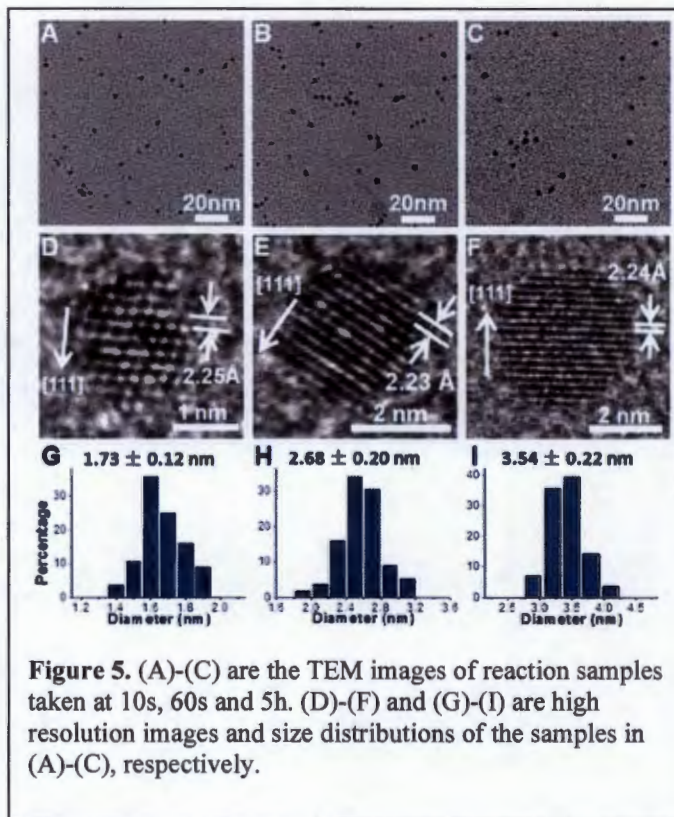


Fig. 4 shows the color evolution of both blank reaction and the reaction with peptides present. The quickly darkening color observed in the blank reaction indicates the reaction evolved very fast (Figs. 4 A-E). After a couple hours, there were obvious particles aggregations precipitating out. TEM studies show NCs from blank reaction typically have large sizes ( $> 10$  nm) with wide size distribution, and are usually aggregated together even at the very early stage (Fig. 4F). In contrast, the reaction with peptide present evolved much more slowly and is highly controllable (Figs. 4 G-K). The resulting solution was stable for up to a few months, indicating NCs were well dispersed in solution. TEM

studies show these NCs typically have nearly spherical shapes, with a narrow size distribution, and remain well separated and well dispersed in solution even after long duration of aging (Fig. 4L). The comparison with blank reaction implies that the peptides suppress the crystal growth at very early stage and change the growth kinetics of Pt NCs. The observation suggests that the free standing peptide TLHVSSY, although selected against platinum surface as a part of M13 phage coat protein, retains the strong binding ability to the crystal surface. The strong binding ability can be attributed to the electrostatic interaction, chemical conjugation, geometrical match, or the combination of these factors between peptide molecules and crystal surface.

We tentatively attribute the effects that peptides exert on Pt NC size and shape to its strong binding ability to Pt. We suggest that peptides bind to reduced Pt atoms or Pt nuclei and form a peptide coating on Pt NC surface. The coverage of peptides prevents NC growth from particle coalescence as well as slows down monomer attachment onto the NC surface. Hence the Pt NC growth rate with peptide present is greatly reduced when compared to the blank reaction, resulting in much smaller NC sizes. At the meanwhile, when peptides bind to Pt NC surface, it changes the Pt NC surface energy landscape and hence its growth kinetics, which may lead to the observed different morphologies compared to blank reactions.

With the greatly reduced growth rate, we were able to achieve ultrasmall NCs of variable sizes with narrow size distribution by stopping the reaction at different times. In this experiment, aliquots of reaction samples of different time, e.g. 10 s, 60 s, and up to 36 h, were taken out of the reaction solution and immediately put into ice bath. Then droplets of different samples were taken to prepare TEM samples. The copper grids were



**Figure 5.** (A)-(C) are the TEM images of reaction samples taken at 10s, 60s and 5h. (D)-(F) and (G)-(I) are high resolution images and size distributions of the samples in (A)-(C), respectively.

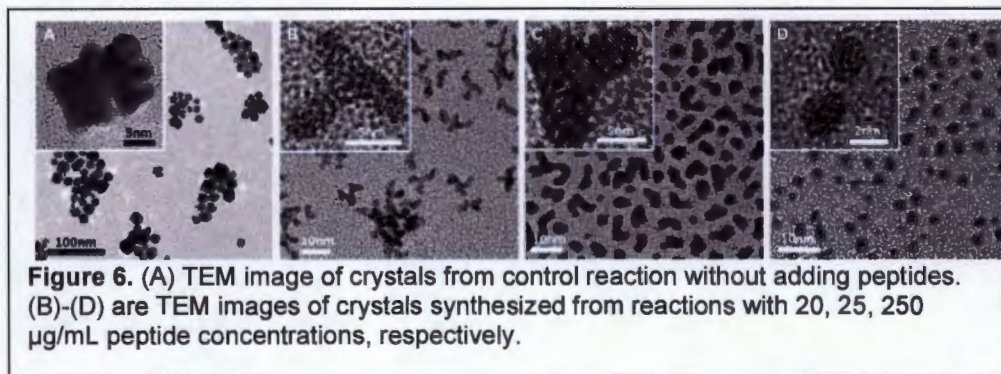


rapidly dried and washed with water to remove unreacted precursors. Figs. 5 A-F show the TEM images of NCs taken out from reaction at 10 s, 60 s and 5 h. In Fig. 5A, the Pt NCs at 10 s after reductant injection have an average size of 1.73 nm, which is much smaller than the NCs formed at the same time in blank reaction (Fig. 4F). Fig. 5B shows the Pt NCs taken out of reaction solution at 60 s, which have an average size of 2.68 nm. The Fig. 3C shows the NCs taken from reaction solution 5 h after the injection with an average size of 3.54 nm. High resolution TEM (HRTEM) images in Figs. 5 D-F show that the atomic layers of Pt NCs in [111] direction, as marked by the arrows, grow from 7 layer to 12 layers, and finally to 16 layers. With this approach, ultrasmall Pt NCs of variable sizes below 5 nm can be synthesized in a highly controllable fashion. Histogram of Pt NC sizes shows highly uniform size distribution, typically with standard deviation less than 10% or less than one atomic layer variation on average (Figs. 5 G-I).

### (B) Morphology control

Using the same peptide sequence, we further demonstrate the synthesis of Pt NCs with multipod morphology by changing the reaction conditions, and that the multipod morphology can be controlled by altering the peptide concentration. Using potassium tetrachloroplatinate ( $K_2PtCl_4$ ) as the precursor and sodium borohydride ( $NaBH_4$ ) as the reducing agent, the reaction is conducted in aqueous solution at room temperature. A  $K_2PtCl_4$ /peptide aqueous solution was prepared, aging for 1 hour. The concentration of  $K_2PtCl_4$  was fixed at 1 mM. Peptide concentration was varied from 0-250  $\mu\text{g/mL}$  to observe the effect of peptide on the crystal morphology.  $NaBH_4$  solution of 40 mM concentration was added into the  $K_2PtCl_4$ /peptide solution with automatic syringe. Typically, a volume of 100  $\mu\text{L}$   $NaBH_4$  solution was added to complete the reaction.

The Figure 4 shows the as-synthesized Pt nanocrystals with different molar ratios between  $K_2PtCl_4$  and peptide (i.e. changing peptide concentrations while keeping the



concentration of  $K_2PtCl_4$ ). The transmission electron microscope (TEM) samples were prepared after 1 h of reaction. The control reaction without adding peptide is shown in Figure 4A. The typical crystals obtained without peptide added show a hyperbranched morphology (as shown in the inset Fig.6A) with the average size around 20 nm (ca. 50 % yield). With the TLHVSSY peptide added, typical crystals seen on TEM grid have a multipod morphology with the average size down to 10 nm, as shown in Figure 4B. The term multipod is used because bi-pod, tri-pod and tetra-pod nanocrystals coexist on the grid. When higher peptide concentration was used, the crystals of multipod morphology



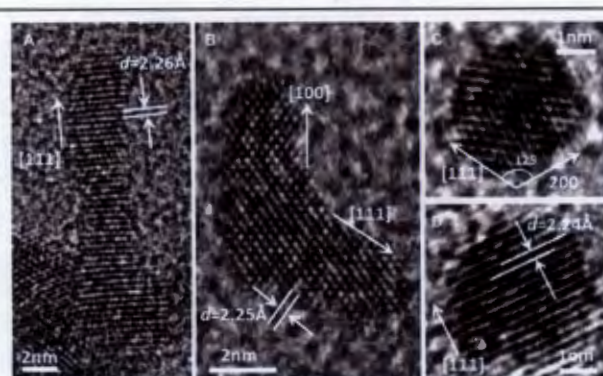
still exist but with shorter pods, as shown in Figure 2 C, i.e. the length of pods can be controlled by varying the concentration of peptides in solutions. In addition, near spherical crystals without pods can also be observed at low yield (ca. 10%). When the peptide concentration was increased up to 250  $\mu\text{g/mL}$ , no multipod nanocrystals were observed. Instead, the typical nanocrystals show monodisperse near spherical shape with the average size around 2.5 nm. Further information can be obtained from the TEM images that the dispersity is becoming better with the increase of peptide concentration.

We further characterize the nanocrystals by HRTEM for the lattice analysis. As shown in Figure 5A, at low peptide concentration, the pods can be as long as 10 nm. According to the lattice spacing measurement, the spacing distance of 2.26 Å is corresponding to the  $\langle 111 \rangle$  lattice spacing, which means that the pods are growing along  $\langle 111 \rangle$  direction with the presence of peptide in solution. When increasing the peptide concentration, one result is that the nanocrystals, shown in Figure 7B, C and D, show shorter lengths along  $\langle 111 \rangle$  direction, the other result is that more and more bi-pod crystals are emerging. From Figure 3B, we can see that the bi-pod crystals have a mix of pods growing along  $\langle 111 \rangle$  and  $\langle 100 \rangle$  directions, looking from  $\langle 110 \rangle$  zone axis. There's also twinning effect observed in the crystals obtained from high peptide concentrations. Figure 3D, also with  $\langle 110 \rangle$  zone axis, shows the twinning formed with the  $\{111\}$  twinning plane. One thing worth noting is that no pods are observed to grow along  $\langle 110 \rangle$  direction. Figure 3e shows the Pt nanocrystals obtained from peptide concentration of 250  $\mu\text{g/mL}$ . The spherical shape implies that the growth along all directions are inhibited, even for  $\langle 111 \rangle$  and  $\langle 110 \rangle$  which are observed growth directions.

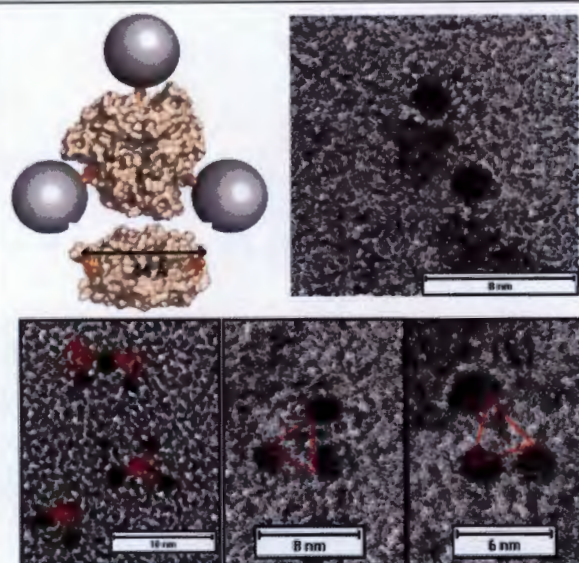
### (C) Pt-Protein Assembly

Together with TY's group we have successfully demonstrated that this ultra small Pt NCs can be readily assembled onto protein surface with specified location. A trimeric structure has been achieved (Figure 8).

**In summary, We have successfully demonstrated that** (1) The selected peptide molecule is able to specifically target and bind to NC surface, and control both the



**Figure 7.** HRTEM images of crystals synthesized from reactions with peptide concentrations of (A) 20, (B) 25, (C, D) 250  $\mu\text{g/mL}$ , respectively.



**Figure 8.** Schematic and TEM images of trimeric CutA protein templated Pt NCs assembly.



morphology and size of the final NCs, in aqueous solution at room temperature, even out of it is viral protein context. *This is a significant preliminary experiment that enables our future experiments*; (2) Using the specific peptides, we have achieved for the first time, the rational synthesis of monodisperse ultrasmall Pt NCs, in aqueous solution at room temperature. Uniform near-spherical Pt NCs with size from 1.73 to 3.54 nm were achieved with very narrow size distribution; (3) Using the specific peptide, we have also demonstrated the control over Pt NC morphologies, i.e. Pt NCs of multipods or near spheres can be achieved by manipulation of peptide concentrations (i.e. ratios of Pt/Peptide). The shape evolution of nanocrystals suggests that the peptide molecules may have preferable binding onto {110} and {100} facets at low peptide concentration, but lose the selective binding at high peptide. Detailed studies on the Pt NCs synthesis with the stabilization of peptide molecules are underway for better size and shape control as well as elucidation of growth mechanism. (3) Working with TY we have demonstrated the feasibility of linking water-solution small Pt NCs to trimeric CutA protein surface and achieved Pt NC assembly with protein.